Fast Spectroscopic Imaging and Field Compensation Using Frequency Modulation at Ultra-High-Field

A THESIS
SUBMITTED TO THE FACULTY OF THE GRADUATE SCHOOL
OF THE UNIVERSITY OF MINNESOTA
BY

Albert Woo Ju Jang

IN PARTIAL FULFILLMENT OF THE REQUIREMENTS
FOR THE DEGREE OF
DOCTOR OF PHILOSOPHY

Advisor: Jianyi Zhang
Co-advisor: Michael Garwood

June, 2016

Acknowledgements

During my first visit to Minnesota for an ISMRM Workshop in 2010, I had the delightful opportunity of taking a tour of the Center for Magnetic Resonance Research (CMRR). Since my official arrival in the summer of 2011, I have had the distinct privilege of working with world class researchers from diverse backgrounds who have been like family to me through their endless support during my 5 years here training as a doctoral student. I believe this is what makes CMRR truly special in addition to being a leading research center for magnetic resonance.

First and foremost, I would like to give my utmost gratitude to my advisor Dr. Jianyi Zhang and co-advisor Dr. Michael Garwood. Both have equally provided invaluable guidance, encouragement, and inspiration, through both good times and bad. Dr. Zhang showed me the significance of magnetic resonance from a biological perspective which I have gained much appreciation for. It was his constant push and support that drove me to be where I am today. Dr. Garwood enlightened me with the joy of not only learning about the art of pulse design, but science in general. I will always admire his passion and willingness to step outside his comfort zone to gain new insight, which has been a big influence to me. I could not have asked for a better co-advisor.

I would like to thank Dr. Anand Gopinath for being my ECE mentor, always offering valuable advice, both academic and non-academic. I would also like to thank Drs. Tommy Vaughan and Rhonda Franklin for taking their time to serve on my Preliminary and Final Oral Exam Committee, and Dr. Kâmil Uğurbil, for creating and sustaining an outstanding research environment.

I am deeply indebted to Qiang Xiong, who was like a big brother. The countless swine studies we've done together will always bring back fond memories. Without his help, I would not have been able to contribute to the Zhang lab.

I am also grateful to Naoharu Kobayashi. It was the endless dumb questions and discussions I had with him that enabled me to learn the nitty gritty technical details of MR. Like Qiang Xiong, I would not have been able to contribute to the Garwood lab without him.

I must also thank the following CMRR family members for whom I have always counted on for help and support: Gregor Adriany, Peter Andersen, Weina Cui, Djaudat Idiyatullin, Małgorzata Marjańska, Steen Moeller, John Strupp, Ivan Tkac, Jinjin Zhang, Pengyuan Zhang, etc.

I must acknowledge the American Heart Institute (AHA) for providing me financial support (14PRE20380625).

Last but not least, I thank my family: my father Henry, my mother Jeong Lim, and sister Jenni; and my girlfriend Jooyoung, for their unconditional love and support.

In memory of my dear friend,
Teddy Kim

Abstract

The high energy phosphates (HEP) in the myocardium, which are critical to understanding the cardiac function in both normal and pathophysiologic states, can be assessed non-invasively *in vivo* using phosphorus-31 (^{31}P) spectroscopy. Compared to proton, for the same volume and magnetic field strength, the available signal-to-noise (SNR) ratio of the HEP metabolites is orders of magnitude lower mainly due to its intrinsically low concentration[1]. Hence, cardiac spectroscopy greatly benefits when performed at ultra-high-fields (UHF, $\geq$ 7 T), both in terms of increased SNR and increased spectroscopic resolution. However, at ultra-high-field strengths, complications arise from the RF transmit wavelength becoming comparable or smaller than the field-of-view (FOV), thus exhibiting wave-like behavior[2]. Furthermore, even with the spectroscopic resolution afforded at UHF, measuring myocardial inorganic phosphate (Pi) is still a challenge and has been a major barrier in extracting the ATP turnover rate. Recently, an indirect way of extracting the ATP hydrolysis rate forgoing direct measurement of Pi was established[3]. In this work, we combine this method with the T_1^{nom} method[4] to monitor the transmural distribution of forward creatine kinase reaction ($k_{\text{f,CK}}$) and ATP hydrolysis rate ($k_{\text{r,ATPase}}$) of the myocardium, effectively reducing data acquisition time by up to an order of magnitude. In addition, a new class of 2D FM pulses and multidimensional adiabatic pulses are presented, which can compensate for B_1 inhomogeneity through its spatiotemporal properties. These pulses should be valuable for spectroscopic applications at ultra-high-fields.

Contents

List of Tables

List of Figures

Chapter 1

Introduction

Nuclear magnetic resonance (NMR) is a physical phenomenon with applications in fields such as chemistry and medicine. Unlike other modalities such as computed tomography (CT) and positron emission tomography (PET), MR does not involve exposure to ionizing radiation. Due to this non-invasive nature, it is best known for its application in the field of medicine, where it is widely used in magnetic resonance imaging (MRI) and magnetic resonance spectroscopy (MRS). By taking advantage of the difference in relaxation rates, magnetic resonance imaging provides stunning contrast between soft tissues, making it a valuable tool for imaging anatomy and physiological processes of the body. MRS is a valuable diagnostic tool for obtaining biochemical information of tissues and is used to study the metabolic changes in various organs such as the brain and heart.

In particular, the high energy phosphates (HEP) in the myocardium, which are critical to understanding the cardiac function in both normal and pathophysiologic states, can be assessed non-invasively *in vivo* using phosphorus-31 (^{31}P) spectroscopy. Studies have observed abnormalities in the myocardial metabolism for hearts with cardiac pathologies such as myocardial infarction[5, 6], left ventricular hypertrophy[7], and hypertension[8]. Specifically, a decrease in the phosphocreatine-to-ATP (PCr/ATP) ratio accompanied by an overall reduction in the high energy phosphate levels have been consistently observed. Noteworthy are a series

of large animal studies carried out by Dr. Jianyi Zhang's group, which used a porcine model of postinfarction left ventricular remodeling (LVR) by acute coronary occlusion[9, 10, 11]. In these studies, remodeling of non-infarcted myocardium with left ventricular (LV) chamber dilation, reduced systolic performance, increased wall stress, and reduced PCr/ATP ratio were observed and correlated well with the size of the initial infarct. In another study, where a concentric LV hypertrophy (LVH) was created by severe aortic banding (AOB), LV remodeling resulted in a reduction of HEP levels as well as a decrease in the PCr/ATP ratio. Furthermore, these abnormalities were found to be in linear correlation to the degree of hypertrophy[12].

Until recently, limitations in measuring the ATP turnover rate has stimulated much speculation on whether a decrease in the myocardial ATP turnover rate contributes to the progression of cardiac dysfunction. Using conventional magnetization saturation transfer (MST) techniques, direct measurement of the ATP turnover rate relies on precise quantification of inorganic phosphate (Pi), which has been a challenge largely due to two reasons: first being the intrinsically low concentration of Pi and second it overlapping peaks with 2,3-DPG. Fortunately, an indirect way of extracting the ATP hydrolysis rate forgoing direct measurement of Pi was recently established[3]. Using magnetic saturation transfer experiment by double saturating both PCr and Pi, it was shown that the ATP hydrolysis rate in the border zone (BZ) of heart with myocardial infarction (MI) decreased significantly, while in hearts that received cell-treatment, this decline was significantly improved. In another study which used an aortic banding induced severe LV hypertrophy model, severe reduction of the LV function during the acute phase of AOB was accompanied by a decrease in ATP utilization[13]. In the same study, a linear relationship between the rate increase of the ATP hydrolysis rate constant and LV rate-pressure product (RPP) increase during catecholamine stimulation was also observed.

Compared to proton, for the same volume and magnetic field strength, the

available signal-to-noise (SNR) ratio of the HEP metabolites is orders of magnitude lower mainly due to its intrinsically low concentration in addition to a lower gyromagnetic ratio[1]. Hence, cardiac spectroscopy greatly benefits when performed at ultra-high-fields (UHF, $\geq$ 7 T), both in terms of increased SNR and increased spectroscopic resolution. This benefit in SNR has been the main driving force towards ultra-high-field strengths, in which the Center for Magnetic Resonance Research (CMRR) at the University of Minnesota has been a pioneer. However, at ultra-high-field strengths, complications arise from the RF transmit wavelength becoming comparable or smaller than the field-of-view (FOV), thus exhibiting wave-like behavior[2]. In addition to non-uniform B_1, main field B_0 inhomogeneity also becomes significant when operating at ultra-high-fields.

^{31}P spectroscopy also profits from the sensitivity enhancement provided by surface coils, making it a preferable coil of choice. However, the B_1 profile produced by surface coils are highly inhomogeneous, varying by an order of magnitude within the sensitive volume. In this type of B_1 environment, high variations in flip angle is observed when conventional amplitude modulated (AM) pulses are used, resulting in quantification errors of metabolites. This high variation in B_1 field can be overcome using frequency modulated (FM) pulses that have adiabatic properties[14, 15]. Adiabatic pulses enable uniform excitation in the presence of extreme B_1 inhomogeneity and have proven to be of great use in spectroscopic sequences such as FLAX-ISIS[16] and RAPP-ISIS[17] developed by Dr. Michael Garwood and colleagues.

The aim of this dissertation is to introduce new methods applicable to magnetic resonance spectroscopic imaging with an emphasis on fast imaging and field inhomogeneity compensation. The outline adheres to the following. Chapter 2 is a brief historical overview and review of the basic principles pertaining to magnetic resonance imaging and cardiac ^{31}P spectroscopy. Chapter 3 presents an ultra-fast method for measuring the transmural distribution of ATP hyrdolysis rates *in vivo*, which has been accepted for publication[18]. Chapter 4 describes

a new design method of two-dimensional (2D) pulses using a spatially dependent frequency sweep based on position-dependent k-space formulation, which can fully compensate for B_1 inhomogeneity while partially compensating for B_0 inhomogeneity. This work has also been accepted for publication[19]. Chapter 5 introduces design method of multidimensional spatially selective adiabatic pulses based on a sub-pulse approach. Using parallel excitation techniques[20, 21, 22], this method should easily be applicable for single-voxel spectroscopy, drastically reducing acquisition time compared to conventional methods[23]. This work has been submitted for publication in Magnetic Resonance in Medicine[]. Chapter 6 covers preliminary simulation studies that have been done on fully compensating for B_0 in one-dimension (1D) and concludes the thesis with a summary and direction for future research.

Chapter 2

Background

2.1 History

The roots of NMR starts with the Stern-Gerlach experiment[24], which revealed the quantum nature of spin by sending silver atoms through an inhomogeneous magnetic field. Rabi and coworkers extended the Stern-Gerlach experiment by sending hydrogen molecules through an additional homogenous magnetic field, observing that energy was absorbed at a specific frequency[25]. Independently, Bloch, Hansen, and Packard[26, 27, 28] applied radiofrequency (RF) energy to macroscopic magnetization and successfully detected magnetic resonance, while Purcell, Torrey, and Pound[29] was able measure absorption of RF energy by the proton magnetic moments of paraffin, simultaneously leading to the discovery of nuclear magnetic resonance in 1946. This contribution lead to Bloch and Purcell sharing the Nobel prize in physics in 1952.

In its infancy, NMR was used as a tool purely for analytical chemistry, in which spectra was acquired through a lengthy process of sweeping the main magnetic field strength while fixing the radiofrequency (RF), known as the continuous wave mode. Then in 1966, Ernst and Anderson[30] introduced pulsed NMR utilizing Fourier transform, which enhanced sensitivity and acquisition speed, enabling study of fast chemical processes and thus transforming the way NMR is practiced.

NMR was then extended to *in vivo* applications in which Damadian[31] reported difference in relaxation constants of tumor tissues and normal tissues. In 1974, Hoult et al[32] showed metabolic changes of a living excised muscle using ^{31}P spectroscopy.

While the field of NMR was burgeoning through *in vivo* applications, a new branch that applied NMR to imaging was launched. By applying magnetic field gradients, Lauterbur[33] exhibited an image of water filled tubes using back-projection of NMR signals, while Mansfield and Grannell[34] showed localization of NMR signal, demonstrating the ability to spatially encode independent of RF wavelength. Thus MRI was born in 1973, in which Lauterbur and Mansfield later shared the Nobel prize in medicine (2003). Ever since, MRS and MRI have constructively influenced each other, both evolving through the development of various advanced techniques. In the following, we lay down the basic fundamentals of MR along with the background relevant to the work presented.

2.2 NMR

2.2.1 Classical View

In the classical interpretation, spin is viewed as an electrical charge that rotates around its own axis (Fig. 2.1a). Based on this picture, it is modeled as a current loop with radius r carrying current I. This induces a magnetic field which has an associated magnetic dipole moment vector, $\vec{\mu}$, given by

$$\vec{\mu} = IA\hat{n} \tag{2.1}$$

where A is the area enclosing the loop ($= \pi r^2$) and $\hat{n}$ is a unit vector obeying the right-hand rule with respect to the direction of current (Fig. 2.1b).

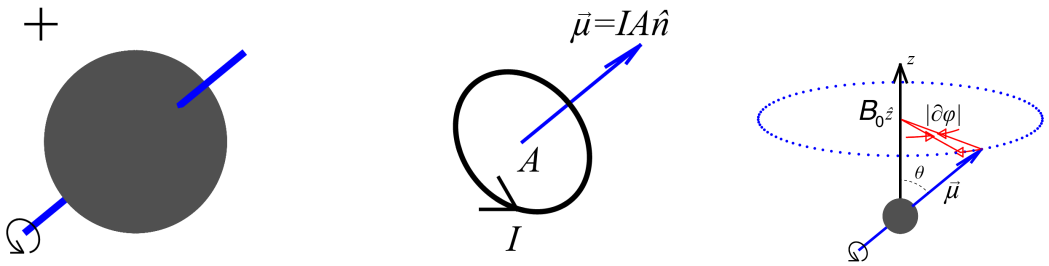

(a) **(b)** **(c)**

Figure 2.1: (**a**) Classical view of spin as an electrical charge that rotates around its own axis. (**b**) This is modeled as an electrical current I in a circular loop enclosing area A that creates a magnetic dipole moment $\vec{\mu} = IA\hat{n}$. (**c**) When an external field $\vec{B}_{\text{ext}} = B_0\hat{z}$ is applied at an angle θ with respect to the magnetic dipole moment, a net torque results, causing the magnetic dipole moment to rotate or precess along a left-handed clockwise direction about $\vec{B}_{\text{ext}}$ by phase increments $|\partial\phi| = \gamma|\vec{B}_{\text{ext}}||\partial t|$.

For a proton with charge q that rotates at a constant speed v along the azimuthal direction, the magnetic dipole moment is

$$\vec{\mu} = \left(\frac{qv}{2\pi r}\right)(\pi r^2)\hat{n} = \frac{qvr}{2}\hat{n} \tag{2.2}$$

Dividing and multiplying by the proton mass m_p, Eq. (2.2) can be rearranged to show a direct proportional relationship between the proton's spin angular momentum $\vec{J}$ and resulting magnetic dipole moment $\vec{\mu}$:

$$\vec{\mu} = \gamma\vec{J} \tag{2.3}$$

The proportionality constant γ, called the gyromagnetic ratio, is particle or nucleus dependent with units $rad\cdot sec^{-1}\cdot T^{-1}$. For nucleus ^{1}H and ^{31}P, the respective gyromagnetic ratios are 267.513 $rad\cdot sec^{-1}\cdot T^{-1}$ and 108.291 $rad\cdot sec^{-1}\cdot T^{-1}$.

In the presence of an external magnetic field $\vec{B}_{\text{ext}}$ that is at an angle θ with respect to the magnetic dipole moment, a force acts on the the differential line charge element $\lambda\partial\vec{l}$, where λ is charge per unit length along the current loop. This

differential force is the Lorentz force given by

$$\partial\vec{F} = \lambda\partial\vec{l}\times\vec{B}_{\text{ext}} \tag{2.4}$$

Consequently, the differential line charge element experiences a differential torque

$$\partial\vec{\tau} = \vec{r}\times\partial\vec{F} \tag{2.5}$$

where $\vec{r}$ is the radial vector that points from center of the loop to the position where differential Lorentz force $\partial\vec{F}$ is applied.

Combining Eq. (2.4) with Eq. (2.5), applying the double cross-product formula and line integrating along the loop, one arrives at the net torque acting on the current loop,

$$\vec{\tau} = \vec{\mu}\times\vec{B}_{\text{ext}} \tag{2.6}$$

Since torque is the rate of change in angular momentum ($\vec{\tau} = \frac{\partial\vec{J}}{\partial t}$), combining this with Eq. (2.3), Eq. (2.6) can be rearranged to give the equation of motion:

$$\frac{\partial\vec{\mu}}{\partial t} = \gamma\vec{\mu}\times\vec{B}_{\text{ext}} \tag{2.7}$$

Solving the differential equation shows that the magnetic dipole moment rotates or precesses along the left-handed clockwise direction about $\vec{B}_{\text{ext}}$ by phase increments $|\partial\phi| = \gamma|\vec{B}_{\text{ext}}||\partial t|$ (Fig. 2.1c). This results in the well-known Larmor precession formula

$$\omega_0 = \left|\frac{\partial\phi}{\partial t}\right| = \gamma|\vec{B}_{\text{ext}}| \tag{2.8}$$

which shows that the precession (Larmor) frequency is proportional to magnetic field strength.

The classical energy associated with the proton magnetic dipole moment is given by:

$$E = -\vec{\mu} \cdot \vec{B}_{\text{ext}} = -|\vec{\mu}||\vec{B}_{\text{ext}}| \cos\theta \tag{2.9}$$

According to the equation, energy is minimum when $\vec{\mu}$ is parallel with $\vec{B}_{\text{ext}}$ and maximum when $\vec{\mu}$ is anti-parallel with $\vec{B}_{\text{ext}}$. Although this classical description illustrates when the energy of a magnetic dipole moment is minimized and maximized in terms of its orientation, it is limited in that it fails to describe the resonance condition that arises from the quantization of spin, which is the core of NMR phenomena. For this, a quantum mechanical treatment is needed.

2.2.2 Quantum Mechanical View

In quantum mechanics, elementary particles have an intrinsic quantized spin, which is somewhat analogous to the motion about the center of mass. This intrinsic spin is specified by the spin quantum number s and the secondary spin quantum number m_s. The spin quantum number s dictates the allowed total spin $\vec{S}$ magnitude through

$$\|\vec{S}\| = \hbar\sqrt{s(s+1)} \tag{2.10}$$

where $\hbar$ is the reduced Planck's constant and s are non-negative integers or half integers (i.e., $s = \frac{1}{2}, 1, \frac{3}{2}, 2, \ldots$).

Analogous to orbital angular momentum, the secondary spin quantum number m_s is associated with the possible states that the spin can have along a specific direction, such as the z-direction, which is given by

$$S_z = \hbar m_s \tag{2.11}$$

where m_s can take on a total of $2s + 1$ values from $-s$ to s in steps of one (i.e., $m_s = -s, -s+1, -s+2, \ldots, s-1, s$).

For fermions such as the proton, $s = \frac{1}{2}$ and the total spin angular momentum is $\frac{\sqrt{3}}{2}\hbar$. Thus, the two possible states for S_z are states with spin $+\frac{1}{2}\hbar$ ($m_s = +\frac{1}{2}$; spin-up) and spin $-\frac{1}{2}\hbar$ ($m_s = -\frac{1}{2}$; spin-down). As a consequence, the spin magnetic dipole moment along the z-axis is also quantized and given by $\mu_z = \gamma m_s \hbar$.

In the presence of an external field, the energy degeneracy of the spin along the z-direction is removed and split into two distinct energy levels that is proportional to field strength, known as the Zeeman effect (Fig. 2.2):

$$E_{m_s=\pm\frac{1}{2}} = -\vec{\mu} \cdot \vec{B}_{\text{ext}} = -\mu_z B_z = \mp\frac{1}{2}\gamma\hbar B_0 \tag{2.12}$$

where B_0 is the z-component of $\vec{B}_{\text{ext}}$. The energy difference between the two states ($E_{m_s=-\frac{1}{2}} - E_{m_s=+\frac{1}{2}}$) is

$$\Delta E = \gamma\hbar B_0 \tag{2.13}$$

Linking the frequency associated with the photon energy for emission or absorption with Eq. (2.13), we arrive at the previously derived Larmor frequency equation $\omega_0 = \gamma B_0$.

2.3 Macroscopic Magnetization

Thus far we have only considered the motion of a single proton spin in the presence of an external magnetic field. In practice, NMR phenomena deals with the measurement of bulk magnetization. Magnetization is defined as the total local magnetic dipole moment per unit volume, given by

$$\vec{M} = \frac{1}{V}\sum_{i=1}^{n}\vec{\mu}_i \tag{2.14}$$

where V is a small volume element assumed to have a constant external field, i is the index for protons within the volume element and n is the total number of proton spins. Neglecting interaction with its environment, the equation of motion

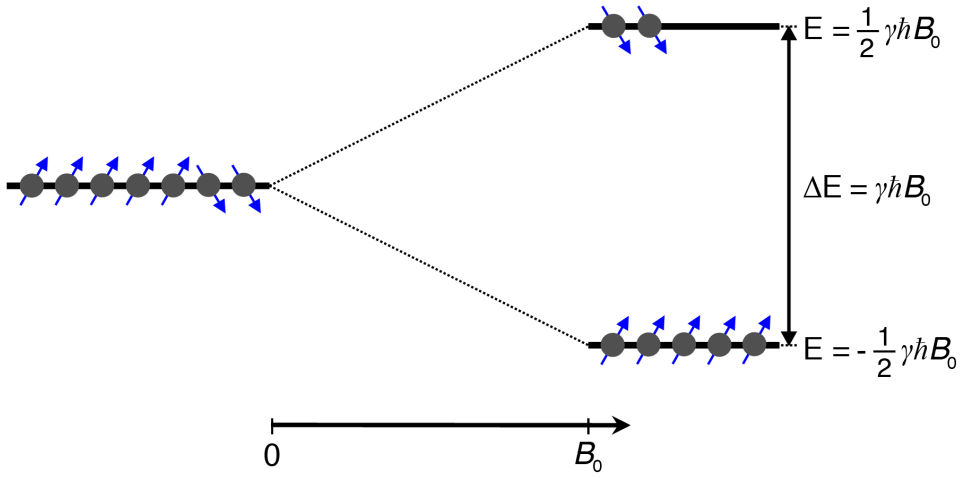

Figure 2.2: In the presence of an external field, the energy degeneracy of the spin along the z-direction is removed, resulting in two distinct energy levels proportional to field strength. The energy difference between the two states is $\Delta E = \gamma\hbar B_0$.

(Eq. (2.7)) for an individual spin can be extended to bulk magnetization by summing over the volume element V:

$$\frac{\partial \vec{M}}{\partial t} = \frac{1}{V}\sum_{i=1}^{n}\frac{\partial \vec{\mu}_i}{\partial t} = \gamma\frac{1}{V}\sum_{i=1}^{n}\vec{\mu}_i \times \vec{B}_{\text{ext}} = \gamma\vec{M} \times \vec{B}_{\text{ext}} \tag{2.15}$$

In the absence of an external magnetic field, the proton spins are randomly oriented and vector sum to zero, thus producing no net magnetization. When a static external field $\vec{B}_{\text{ext}} = B_0\hat{z}$ is applied, the spins have a tendency to align themselves along the direction of the field to attain minimum energy state. However, due to the thermal motion of the lattice, there is thermal energy that excite some spins into a higher energy state by anti-aligning them with the field. This results in a net population difference between spins in the low energy state ($n_{+\frac{1}{2}}$) and high energy state ($n_{-\frac{1}{2}}$), which is governed by the Boltzmann distribution

$$\frac{n_{+\frac{1}{2}}}{n_{-\frac{1}{2}}} = \exp\left(\frac{\Delta E}{k_{\text{B}}T}\right) \approx 1 + \frac{\hbar\omega_0}{k_{\text{B}}T} \tag{2.16}$$

where k_{B} is Boltzmann's constant, T is temperature (K), and the approximation is a truncated Taylor series expansion using $\Delta E = \hbar\omega_0$.

At thermal equilibrium, in the plane perpendicular to $\vec{B}_{\mathrm{ext}}$ (x-y plane), spins are randomly distributed and have no phase coherence, vector summing to zero. However, along the external field direction (z-axis), the individual magnetic dipole moments align either parallel or anti-parallel with respect to this direction. As a result, only the z-components of the dipole moments contribute to the total net magnetization M_0, which is the summation of the parallel ($\mu_z = +\frac{1}{2}\gamma\hbar$) and anti-parallel ($\mu_z = -\frac{1}{2}\gamma\hbar$) magnetic dipole moments in volume element V given by,

$$M_0 = (\gamma\hbar)^2 \frac{nB_0}{4k_{\mathrm{B}}T} \tag{2.17}$$

where n is the total population. The net magnetization is linear with respect to field strength, which stems from the population difference increase between the two spin states at higher fields (Eq. (2.16)).

2.3.1 Chemical Shift

Nuclei in different molecules are surrounded by different chemical environments. In the presence of an external field, neighboring electrons have an associated magnetic dipole moment similar to protons, but aligned opposite the external field. As a result, the field that the nucleus encounters reduces or "chemically shifts" according to

$$B = B_0(1 - \sigma) \tag{2.18}$$

where σ is a dimensionless environment dependent shielding constant, usually expressed in parts per million (ppm). Thus, the actual precession frequency of the nucleus is $\omega = \gamma B_0(1-\sigma)$. This sensitivity to chemical shift enables detection of important compounds and is what makes NMR a powerful tool in chemistry and medicine. Moreover, due to chemical shift being dependent on the external

field strength, NMR at higher fields afford higher spectral resolution and greater signal intensity.

To remove its field dependence, it is often more convenient to express chemical shift with respect to some reference compound. By convention, chemical shift δ is defined as

$$\delta = \frac{\omega - \omega_{\text{ref}}}{\omega_{\text{ref}}} \cdot 10^6 \tag{2.19}$$

where ω_{ref} is the resonance frequency of a reference compound and δ has units of ppm. A widely accepted reference compound for ^{1}H and ^{13}C NMR is tetramethylsilane (TMS) due to it being inert and insensitive to external environments such as temperature and ionic strength. For *in vivo* cardiac ^{31}P MRS, phosphocreatine (PCr) is often used as the reference of choice, resulting in γ-ATP and inorganic phosphate (Pi) having chemical shifts of -2.6 ppm and $\sim$5 ppm respectively.

2.4 Excitation

As previously stated, spins have no coherence along the transverse plane at thermal equilibrium and the net magnetization vector is static in the z-direction. To detect the precessional motion, spins are radiated by a secondary magnetic field oriented along the transverse plane, $\vec{B}_1(t)e^{-i\omega t}$, which oscillates at a frequency in the MHz range with amplitude modulated by $|\vec{B}_1(t)|$, called an RF pulse. Application of the RF pulse effectively rotates the longitudinal magnetization onto the transverse plane by evenly populating spins in both energy states and generating phase coherence amongst individual spins.

To better visualize this, the classical treatment of viewing magnetization as a vector is employed. As will be evident, it is more convenient to work in a coordinate system that rotates at the frequency of the applied RF field ω, called the rotating frame of reference (contrary to the laboratory frame of reference). In this frame of reference, denoted by $\hat{x}'$, $\hat{y}'$, and $\hat{y}'$, the x and y axis rotate with respect to the static laboratory frame of reference according to:

$$\begin{aligned} \hat{x}^{'} &= \cos(\omega t)\hat{x} - \sin(\omega t)\hat{y} \\ \hat{y}^{'} &= \sin(\omega t)\hat{x} + \cos(\omega t)\hat{y} \\ \hat{z}^{'} &= \hat{z} \end{aligned} \tag{2.20}$$

In the rotating frame, both the RF pulse and relative motion of the precessing spins appear stationary. In this frame, the equilibrium magnetization M_0 sees and therefore precesses about an "effective" field, which is the vector sum of the transverse component $\vec{B}_1(t)$ and longitudinal component $(B_0 - \frac{\omega}{\gamma})$. When the RF is applied at the Larmor frequency on resonance ($\omega = \omega_0$), $\vec{B}_{\text{eff}}(t) = \vec{B}_1(t)$, and M_0 rotates towards the transverse plane. The total rotation or flip angle is given by $\theta = \gamma \int_0^{T_\text{p}} |\vec{B}_1(t)|dt$, where T_p is the duration of $\vec{B}_1(t)$ called RF pulse length. In contrast, in the laboratory frame of reference, instead of appearing static, $\vec{B}_1(t)$ oscillates at frequency ω_0, while M_0 rotates towards the transverse plane and simultaneously precesses about B_0. Figure 2.3 compares the evolution of a 90° rotation seen from both frames of reference. Working in the rotating frame clearly simplifies the dynamics of magnetization. Therefore, going forward, unless stated otherwise, we will assume working in rotating frame coordinates and denote it by $\hat{x}$, $\hat{y}$, and $\hat{z}$.

It is possible to superimpose an additional spatially (linearly) varying field to the existing static field utilizing an extra set of coils called gradient coils. The z-component of the magnetic field becomes

$$B_z = B_0 + \vec{G}_r(t) \cdot \vec{r} \tag{2.21}$$

where $\vec{G}_r$ is a spatially constant gradient in the $\vec{r}$-direction $\left(\vec{G}_r = \frac{\partial B_z}{\partial \vec{r}}\right)$. Generally, there are three sets of gradient coils $\vec{G}_x(t)$, $\vec{G}_y(t)$, and $\vec{G}_z(t)$, which spatially vary along the x, y, and z-direction respectively. As a consequence, the spin precession rates vary linearly along the gradient direction. Gradients are often used to manipulate the precession frequency of excited spins and encode spatial information by frequency encoding along that direction. When applied in concert with an

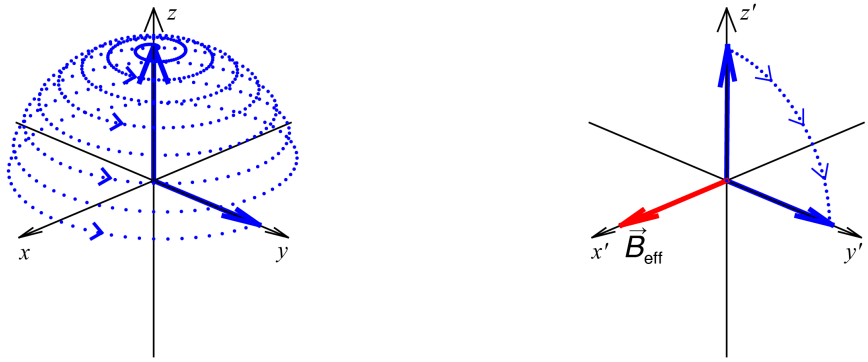

Figure 2.3: Spin evolution of a 90° rotation in the (**a**) laboratory frame and (**b**) rotating frame of reference.

RF pulse, spins orthogonal to the gradient direction that precess at frequencies within the RF bandwidth are selectively rotated, resulting in a one-dimensional slice excitation. Furthermore, as will be discussed shortly, through careful design of the gradient being applied as a function of time, selective excitation in two- and three-dimensions can be accomplished.

2.4.1 The Bloch Equations

Up to now, magnetization has been treated as an ensemble of isolated individual spins. However, in real NMR phenomena, spins interact with both its environment and each other, leading to relaxation. Relaxation is the process of magnetization returning to its thermal equilibrium state by releasing the energy absorbed from perturbation. It is observed as an average statistical measurement of the time it takes for 1) the magnetization component parallel to the field ($\vec{M}_z = M_z\hat{z}$), called the longitudinal magnetization, to return to 63% of its thermal equilibrium value , and 2) the magnetization component perpendicular to the field ($\vec{M}_{xy} = M_x\hat{x} + M_y\hat{y}$), called the transverse magnetization, to decay to 37% of its initial value after excitation. These two magnetization components relax different rates

according to

$$\begin{aligned} \frac{\partial \vec{M}_z(t)}{\partial t} &= -\frac{\vec{M}_z(t) - M_0}{T_1} \\ \frac{\partial \vec{M}_{xy}(t)}{\partial t} &= -\frac{\vec{M}_{xy}(t)}{T_2^*} \end{aligned} \tag{2.22}$$

Relaxation parameter T_1 is the longitudinal or spin-lattice relaxation time, and characterizes the energy of the excited spins being transferred to the lattice while going back to thermal equilibrium. The total transverse relaxation time T_2^* is a damping term that characterizes the loss of phase coherence between spins on the transverse plane. The main sources that contribute to T_2^* are 1) the exchange of energy between spins (no net energy transfer) characterized by spin-spin relaxation time T_2, and 2) main field inhomogeneity characterized by relaxation parameter T_2'

$$\frac{1}{T_2^*} = \frac{1}{T_2} + \frac{1}{T_2'} \tag{2.23}$$

Adding the relaxation terms (Eq. (2.23)) to the equation of motion (Eq. (2.15)), we arrive at the Bloch equations[27]. The equations are a set of non-linear macroscopic equations that mathematically describe the motion of magnetization as a function of time with relaxation present. In the rotating frame of reference, it is given by

$$\frac{\partial \vec{M}(\vec{r},t)}{\partial t} = \gamma \vec{M}(\vec{r},t) \times \vec{B}(t) - \frac{M_z(\vec{r},t) - M_0(\vec{r})}{T_1} - \frac{\vec{M}_{xy}(\vec{r},t)}{T_2^*} \tag{2.24}$$

where magnetization is generalized to include spatial-dependency ($\vec{r} = x\hat{x} + y\hat{y} + z\hat{z}$). They are the governing equations for spin manipulation and serve as the main workhorse for understanding NMR phenomena.

2.4.2 Small-Tip-Angle Approximation

Neglecting relaxation effects, the Bloch equation in the rotating frame for excitation is

$$\frac{\partial \vec{M}(\vec{r},t)}{\partial t} = \gamma \vec{M}(\vec{r},t) \times \left[B_{1,x}(t)\hat{x} + B_{1,y}(t)\hat{y} + (\vec{G}_r(t)\cdot\vec{r})\hat{z} \right] \tag{2.25}$$

For an initial magnetization at thermal equilibrium ($\vec{M}(\vec{r},0) = M_0(\vec{r})\hat{z}$), the small-tip-angle approximation[35] assumes that the change in longitudinal magnetization from equilibrium during excitation is negligible $\left(\frac{\partial M_z(t)}{\partial t} = 0\right)$. This decouples the transverse magnetization components from the longitudinal components of Eq. (2.25), enabling a solution to the differential equation in the following closed form:

$$\vec{M}_{xy}(\vec{r},T_{\mathrm{p}}) = i\gamma M_0(\vec{r}) \int_0^{T_{\mathrm{p}}} \vec{B}_1(t) e^{i\vec{k}_r(t)\cdot\vec{r}} dt \tag{2.26}$$

where T_{p} is pulse length, $\vec{B}_1(t) = B_{1,x}(t)\hat{x} + B_{1,y}(t)\hat{y}$, and $\vec{k}_r = -\gamma \int_t^{T_{\mathrm{p}}} \vec{G}_r(t')dt'$. At small-tip-angles, the excitation profile and RF pulse form a Fourier transform pair. Namely, the resulting transverse magnetization is given by the Fourier transform of *excitation k-space*, $\vec{k}_r(t)$, weighted by $\vec{B}_1(t)$, where excitation k-space weighting occurs along a trajectory dictated by the gradient $\vec{G}_r(t')$. Thus, a linear relation between the applied RF and the resulting excitation is established. By sampling and weighting excitation k-space in two, three-dimensions, this Fourier relation can be used to design pulses that selectively excite in two, three-dimensions. Figure 2.4 shows an example of a two-dimensional spiral trajectory RF pulse weighted with a Gaussian windowed jinc function (Figs. 2.4a and 2.4b) and its corresponding excitation profile (Fig. 2.4c).

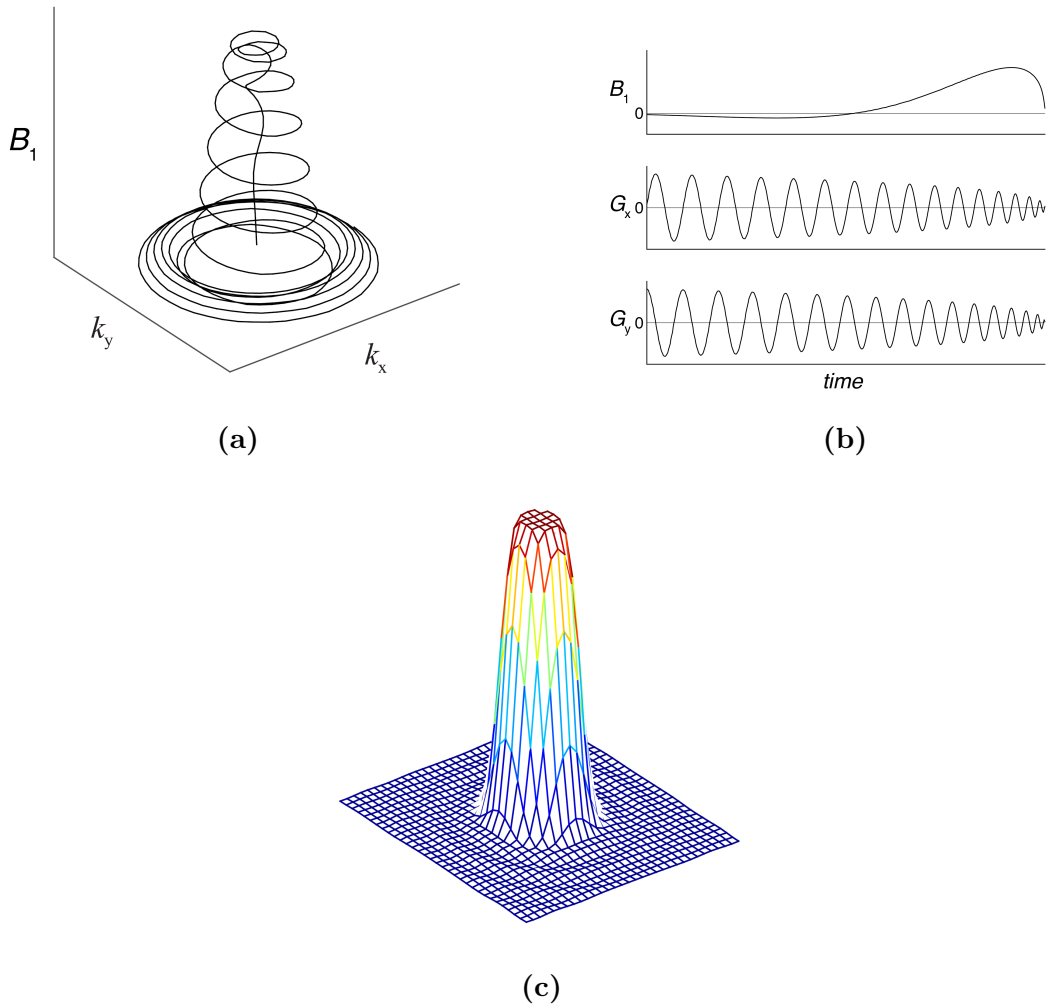

(a) **(b)** **(c)**

Figure 2.4: 16 ms Gaussian windowed 2D Jinc pulse using 16 turn spiral trajectory: (**a**) excitation k-space, (**b**) corresponding pulse, (**c**) and resulting excitation profile.

2.4.3 Frequency Modulated Pulses

Frequency modulated (FM) RF pulses are a class of pulses in which the RF frequency is modulated in addition to amplitude modulation. Compared to amplitude modulated (AM) pulses, FM pulses have unique features and certain advantages. Probably the most well known use of FM pulses is its use in achieving adiabatic rapid passage by sweeping the pulse frequency $\omega_{\mathrm{RF}}(t)$. Known as adiabatic pulses[14, 15], a uniform flip angle can be generated even in the presence of a highly inhomogeneous B_1 profile such as those produced by surface coils, provided that the B_1 amplitude meets a certain threshold requirement. This enables benefiting from the high sensitivity offered by surface coils, which is advantageous to certain applications such as *in vivo* ^{31}P cardiac spectroscopy, where the inherent concentration of the metabolites in the myocardium is low.

The dimensionless amplitude and frequency modulation functions for an FM pulse is denoted by $F_1(t)$ and $F_2(t)$, respectively. To best describe the motion of the magnetization in the presence of adiabatic pulses, we employ a frequency modulated frame of reference that rotates about the z-axis at the instantaneous RF frequency $AF_2(t)$, where A is the amplitude of frequency modulation relative to the pulse carrier frequency ω_{c} with units rad. Called the FM frame (indicated by $x^{'}$, $y^{'}$, and $z^{'}$), where the RF amplitude is along a constant orientation (arbitrarily chosen as the $x^{'}$-axis), spins precessing at the Larmor frequency ω_0 will encounter an additional field component $\frac{\Delta\omega(t)}{\gamma}$ along the $z^{'}$ axis, where $\Delta\omega(t) = AF_2(t) - \omega_0$. This results in a time-dependent effective field, given by

$$\vec{B}_{\mathrm{eff}}(t) = B_1^{\max} F_1(t)\hat{x}^{'} + \frac{\Delta\omega(t)}{\gamma}\hat{z}^{'} \tag{2.27}$$

where $B_1^{\max}$ is the maximum magnitude of the amplitude modulation in units of Hz.

In an adiabatic passage, the pulse frequency starts far above resonance ($\Delta\omega \gg \omega_0$), $\vec{B}_{\mathrm{eff}}$ being initially oriented along the $z^{'}$ direction with amplitude $\approx \frac{\Delta\omega(t)}{\gamma}$. As the frequency is swept from A to $-A$, the effective field rotates towards the $x^{'}$-$y^{'}$

plane at an instant angular velocity $\frac{\partial\alpha(t)}{\partial t}$, where $\alpha(t)$ is the angle formed by $\vec{B}_{\text{eff}}(t)$ and $\frac{\Delta\omega(t)}{\gamma}\hat{z}^{'}\big(= \arctan\left(\frac{\Delta\omega(t)}{\gamma B_1^{\max}F_1(t)}\right)\big)$. The effective field terminates at either the $x^{'}$ axis for an adiabatic half passage or the $-z^{'}$ axis for an adiabatic full passage. Throughout the frequency sweep, if the condition

$$\left|\frac{\partial\alpha(t)}{\partial t}\right| \ll |\vec{B}_{\text{eff}}(t)| \tag{2.28}$$

known as the adiabatic condition, is satisfied, magnetization initially parallel to $\vec{B}_{\text{eff}}$ will follow and magnetization initially perpendicular will remain perpendicular. Figure 2.5 illustrates the $\vec{B}_{\text{eff}}$ trajectory of a constant amplitude linear frequency chirp pulse during an adiabatic full passage and the resulting evolution that an on resonance isochromat experiences.

2.4.4 Offset Independent Adiabaticity

The principle of offset independent adiabaticity (OIA) requires the adiabatic condition to be equally satisfied for isochromats with a resonance offset $\Omega = \omega_0 - \omega_c$ lying within the pulse frequency sweep range $-A < \Omega < A$. Accordingly, the adiabatic condition is given by the ratio

$$\begin{aligned} K(B_1^{\max},\Omega,t) &= \left|\frac{\gamma B_{\text{eff}}(B_1^{\max},\Omega,t)}{\frac{\partial\alpha(t)}{\partial t}}\right| \\ &= \frac{A}{\gamma B_1^{\max}}\frac{[(\gamma B_1^{\max}F_1(t)/A)^2+[F_2(t)-\Omega/A]^2]^{\frac{3}{2}}}{\left|(F_2(t)-\Omega/A)\frac{\partial F_1(t)}{\partial t}-F_1(t)\frac{\partial F_2(t)}{\partial t}\right|} \gg 1 \end{aligned} \tag{2.29}$$

For an isochromat with offset Ω, when the resonance condition ($F_2(t_\Omega) = \Omega/A$) is met, $\left|\frac{\partial\alpha(t)}{\partial t}\right|_{t=t_\Omega}$ is greatest and $\vec{B}_{\text{eff}}(t_\Omega) = B_1^{\max}F_1(t_\Omega)\hat{x}^{'}$. Consequently, K is smallest at time of resonance t_Ω, given by

$$K(t_\omega) = \frac{(\gamma B_1^{\max}F_1(t_\Omega))^2}{A\frac{\partial F_2(t)}{\partial t}\big|_{t=t_\Omega}} \tag{2.30}$$

Equation (2.30) states that for all isochromats with $-A < \Omega < A$, at $t = t_\Omega$, the square of the RF amplitude must be greater than the rate of RF frequency

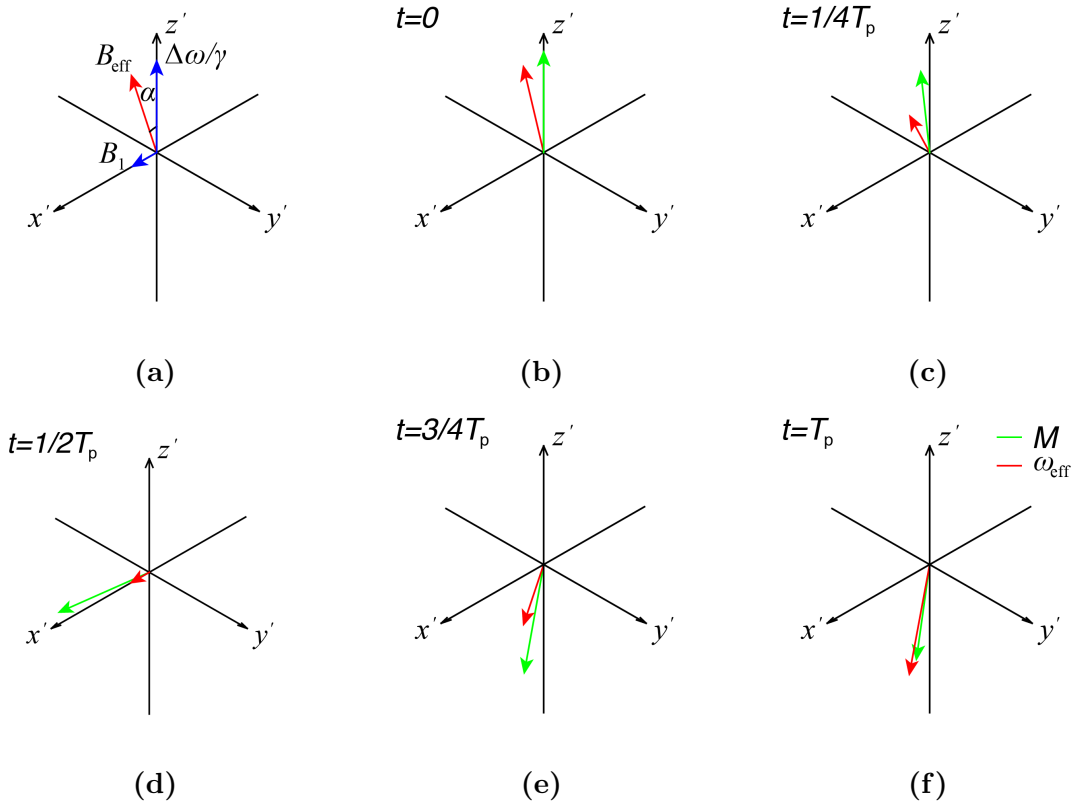

Figure 2.5: (**a**) $\vec{B}_{\text{eff}}$ composed of $\frac{\Delta\omega}{\gamma}\hat{z}'$ and $B_1\hat{x}'$ in the FM frame of reference. $\vec{B}_{\text{eff}}$ (red) and $\vec{M}$ (green) during an adiabatic full passage at (**b**) $t = 0$ (**c**) $t = \frac{1}{4}T_{\text{p}}$ (**d**) $t = \frac{1}{2}T_{\text{p}}$ (**e**) $t = \frac{3}{4}T_{\text{p}}$ and (**f**) $t = T_{\text{p}}$, where T_{p} is length of pulse.

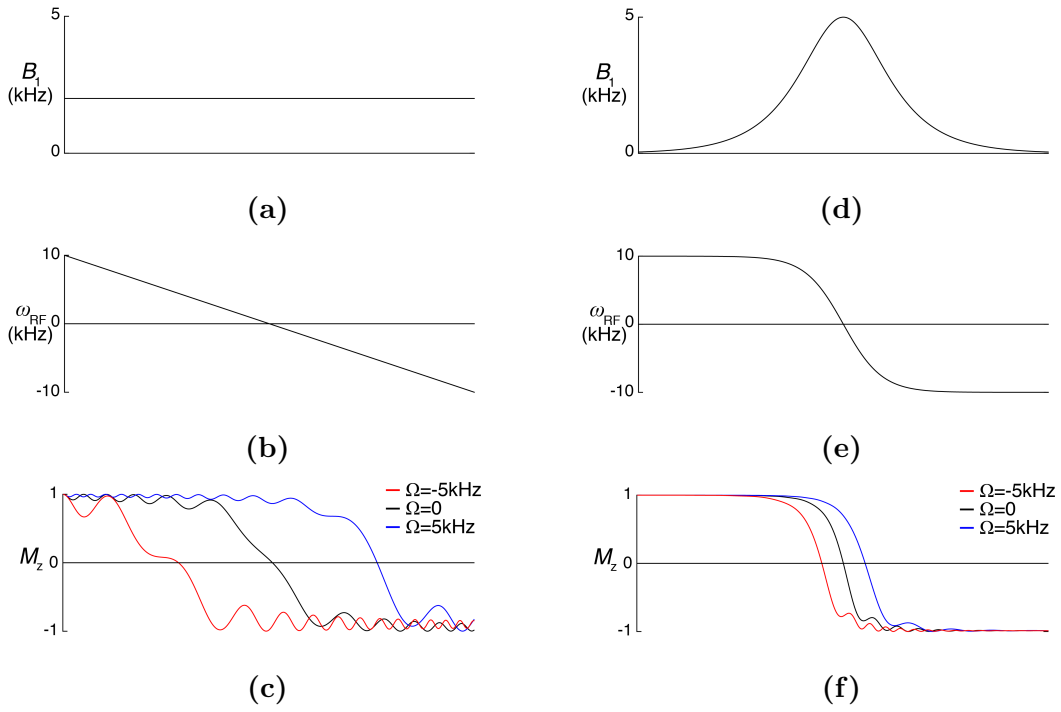

Figure 2.6: Chirp (**a**) amplitude, (**b**) frequency, and (**c**) resulting motion of longitudinal magnetization for isochromats with resonance offset $\Omega = -5, 0, 5\ kHz$. HS1 (**d**) amplitude, (**e**) frequency, and (**f**) resulting motion of longitudinal magnetization for isochromats with resonance offset $\Omega = -5, 0, 5\ kHz$.

change by the same factor $K(t_\Omega)$. If this condition is satisfied, all isochromats with an offset Ω in the frequency sweep range will achieve uniform adiabaticity. Well known pulses that satisfy the OIA condition are the chirp pulse and hyperbolic secant (HS1)[36] pulse, which are shown in Fig. 2.6 along with its resulting inversion profiles.

2.4.5 k-space Formulation of Frequency Modulated Pulses

Starting from Eq. (2.26), which was derived assuming a low tip angle excitation for a pulse with amplitude-modulated function $B_1(t)$, one can include frequency modulation by writing the applied RF pulse in phasor form, $B_1 e^{i\varphi(t)}$, giving

$$
\begin{aligned}
M_{\mathrm{xy}}(\vec{r}) &= i\gamma M_0 \int_0^{T_\mathrm{p}} B_1(t) e^{i\varphi(t)} e^{-i\gamma \int_t^{T_\mathrm{p}} \vec{G}(t')\cdot\vec{r}dt'} dt \\
&= i\gamma M_0 e^{i\varphi(T_\mathrm{p})} \int_0^{T_\mathrm{p}} B_1(t) e^{-i[\varphi(T_\mathrm{p})-\varphi(t)]} e^{-i\gamma \int_t^{T_\mathrm{p}} \vec{G}(t')\cdot\vec{r}dt'} dt \\
&= i\gamma M_0 e^{i\varphi(T_\mathrm{p})} \int_0^{T_\mathrm{p}} B_1(t) e^{-i\gamma \int_t^{T_\mathrm{p}} \frac{(\omega_{\mathrm{RF}}(t')-\omega_\mathrm{c})}{\gamma}\left(\frac{\hat{r}}{|\vec{r}|}\cdot|\vec{r}|\hat{r}\right)dt'} e^{-i\gamma \int_t^{T_\mathrm{p}} \vec{G}(t')\cdot\vec{r}dt'} dt \\
&= i\gamma M_0 e^{i\varphi(T_\mathrm{p})} \int_0^{T_\mathrm{p}} B_1(t) e^{-i\vec{r}\cdot\gamma \int_t^{T_\mathrm{p}} \left[\frac{(\omega_{\mathrm{RF}}(t')-\omega_\mathrm{c})}{\gamma}\frac{\hat{r}}{|\vec{r}|}+\vec{G}(t')\right]dt'} dt \\
&= i\gamma M_0 e^{i\varphi(T_\mathrm{p})} \int_0^{T_\mathrm{p}} B_1(t) e^{i\vec{r}\cdot\vec{k}_\mathrm{r}(t)} dt
\end{aligned} \tag{2.31}
$$

$$
\vec{k}_\mathrm{r}(t) = -\gamma \int_t^{T_\mathrm{p}} \left[\frac{(\omega_{\mathrm{RF}}(t')-\omega_\mathrm{c})}{\gamma}\frac{\hat{r}}{|\vec{r}|}+\vec{G}(t')\right]dt' \tag{2.32}
$$

where $\hat{r} = \frac{\vec{r}}{|\vec{r}|}$ and $\omega_{\mathrm{RF}}(t') - \omega_\mathrm{c}$ is in the frequency-modulated frame of reference. This formulation of k-space that is position dependent has been validated through Gradient Rotating Outer Volume Excitation (GROOVE)[37], a two-dimensional outer volume suppression pulse that uses rotating gradients to accomplish frequency-swept excitation and produce a circular suppression band. Applying the position dependent k-space formulation and invoking a Jacobi-Anger expansion, one can derive the following analytical solution for the excitation profile

$$
\begin{aligned}
M_{\mathrm{xy}}(x,y) = \frac{\gamma M_0 B_1}{\omega_\mathrm{G}} \sum_{m=-\infty}^{\infty}\sum_{l=-\infty}^{\infty} (-1)^m (i)^l J_m\left(\frac{\gamma G}{\omega_\mathrm{G}}x\right) \\
J_l\left(\frac{\gamma G}{\omega_\mathrm{G}}y\right)\frac{e^{i2\pi\left(m+l-\frac{\omega_\mathrm{off}}{\omega_\mathrm{G}}\right)}-1}{m+l-\frac{\omega_\mathrm{off}}{\omega_\mathrm{G}}} e^{i\gamma G\left(T_\mathrm{p}\frac{\omega_\mathrm{off}}{\gamma G}-\frac{y}{\omega_\mathrm{G}}\right)}
\end{aligned} \tag{2.33}
$$

where $\omega_\mathrm{G} = \omega_{\mathrm{RF}}(t) - \omega_\mathrm{c}$ is a constant offset frequency, G is the maximum value of the time-varying gradient along the x and y axis, and J_n and J_l are Bessel functions of the first kind. Comparison between the Bloch simulations and analytical solution (Fig. 2.7) show excellent agreement.

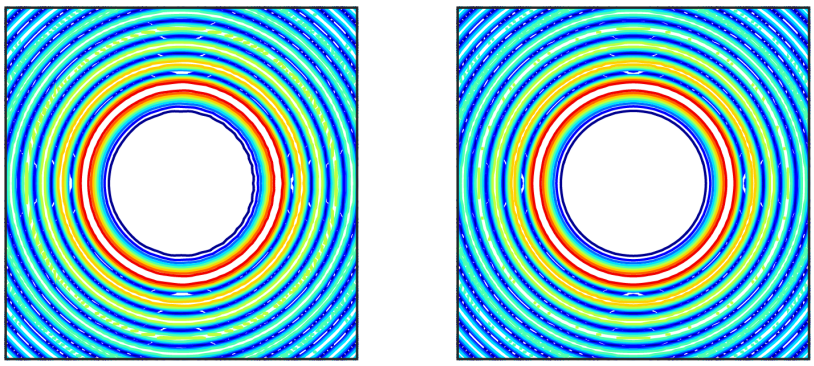

(a) **(b)**

Figure 2.7: Comparing (a) Bloch simulation of GROOVE excitation pulse in the uniform field of isochromats with (b) low flip angle analytical solution derived using position dependent k-space formulation with the same pulse parameters show excellent agreement.

2.5 Acquisition

2.5.1 Free Induction Decay

After excitation, there is a magnetization component in the transverse plane which experiences an effective torque solely due to the leftover main static field B_0. The time dependent motion of transverse magnetization precessing at the Larmor frequency ω_0 induces an electromotive force ε in a nearby pickup coil given by Faraday induction. However, due to relaxation effects, the precessing transverse magnetization and consequently ε exponentially decays proportional to T_2^* with respect to time, while the longitudinal magnetization recovers to its equilibrium value (Eq. (2.22)). Accordingly, following a θ° excitation, the signal acquired reflects the contributions from all the precessing transverse magnetization within a macroscopic sample. Called the free induction decay (FID), it is the volume integral of the transverse magnetization

$$s(t) = e^{-\frac{t}{T_2^*}} \int M_0(\vec{r}) \sin(\theta) e^{-i\omega_0 t} d\vec{r} \tag{2.34}$$

where the integral is taken over the macroscopic sample. Figure 2.8a depicts

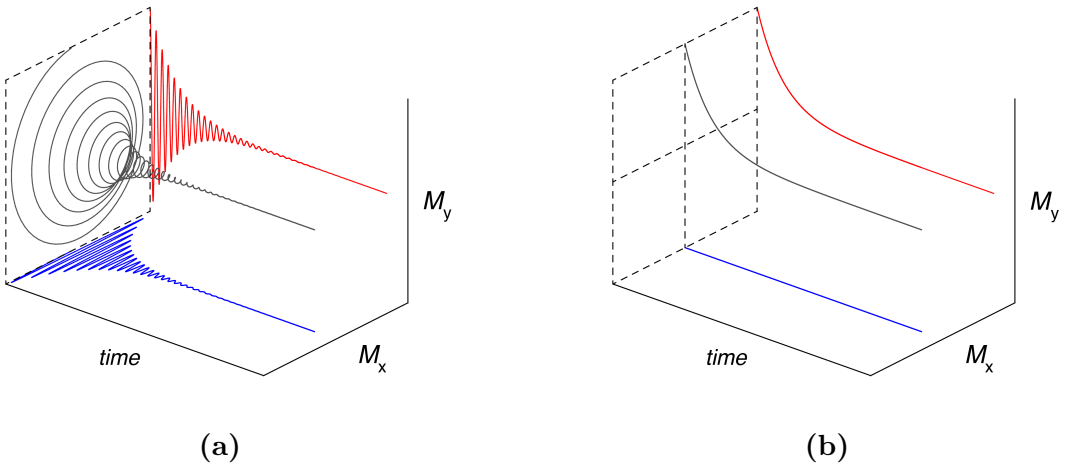

(a) **(b)**

Figure 2.8: Free induction decay of a single isochromat following 90° excitation in the (**a**) laboratory frame and (**b**) rotating frame of reference. The transverse components M_x and M_y are color coded blue and red, respectively. In the laboratory frame, transverse magnetization samples a helix that precesses about B_0 at the Larmor frequency and exponentially decays with a characteristic time T_2^*. In the rotating frame, the helix transforms into a simple exponential decay with no rotation.

the FID of a single isochromat uniform sample subsequent to 90° excitation. In three-dimensions, it samples a helix that traverses along the time dimension with an exponentially decaying radius characterized by T_2^*. An equivalent FID in the rotating frame can be obtained using demodulation. It is achieved by simply multiplying the acquired laboratory frame signal (Eq. (2.34)) by $e^{i\omega_0 t}$. The corresponding demodulated FID is shown in Fig. 2.8b.

2.5.2 Magnetic Resonance Spectroscopy

The acquired FID signal can be used to determine the abundance of various chemical shifts within a sample. This is accomplished by applying a Fourier transform to the time domain signal, resulting in a frequency domain representation:

$$S(\omega) = \int M_0(\sigma) e^{-i\omega_0(1-\sigma)t} e^{-\frac{t}{T_2^*(\sigma)}} dt \tag{2.35}$$

where $\omega = \omega_0(1 - \sigma)$ and T_2^* is now chemical shift dependent. For the FID discussed above involving a single isochromat precessing at a single frequency, the Fourier transform of the exponentially decaying signal is a Lorentzian function centered at precession frequency ω_0. When the sample contains molecules containing multiple chemical shifts, the signal will now contain contributions from transverse magnetization precessing at different frequencies. The Fourier transform will result in several Lorentzian peaks centered around frequencies pertaining to each chemical shift component, with the integral under each peak corresponding to its relative abundance within the sample. Figure 2.9 shows simulation generated spectra for a sample with single (Fig. 2.9a) and multiple (Fig. 2.9b) chemical shifts. Fig. 2.9c is ^{31}P spectra obtained from an *in vivo* heart study.

2.5.3 Magnetic Resonance Imaging

The spatial distribution of the composition, concentration, and relaxation of biological compounds can vary significantly between normal and pathological tissues. Magnetic resonance imaging provides the necessary techniques in obtaining this spatial information along with other properties about the subject of interest. When acquiring a two-dimensional image, after slice select excitation, the in-phase magnetization along the transverse plane is spatially encoded by linearly distributing the precession frequency over space using gradients.

One of the remarkable results of using gradients to spatially encode is being able to resolve voxel sizes that are orders of magnitude smaller than the RF wavelength. By spatially distributing the spin precession frequency, its phase varies linearly along the direction of the applied gradient, effectively imposing a plane wave modulation with spatial frequency given by the time integral of the applied gradient. Therefore, applying a higher gradient amplitude of same length or a longer duration of same amplitude will impart a higher spatial frequency plane wave. Neglecting T_2^*, the resulting FID from a slice selection along the

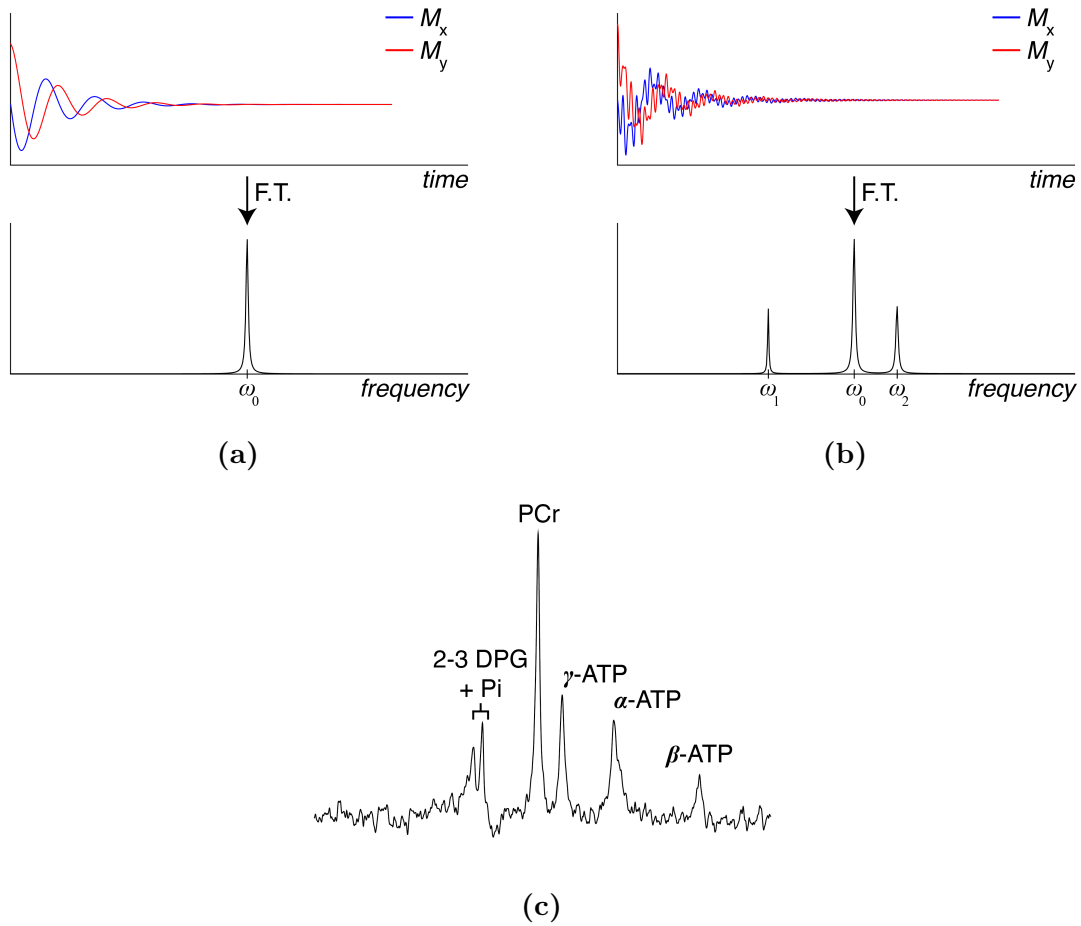

Figure 2.9: (**a**) FID and frequency spectra from single isochromat precessing at ω_0 obtained using T_2^*= 0.2 ms. (**b**) FID and frequency spectra from 3 chemical shift components precessing at ω_0, ω_1, and ω_2 obtained using T_2^* = 0.2 ms, 0.4 ms, and 0.2 ms, respectively. (**c**) Global ^{31}P spectra from an *in vivo* study of the heart shows peaks from right to left corresponding to β-ATP, α-ATP, γ-ATP, PCr, and Pi overlapping with 2-3 DPG.

z-direction followed by gradient application along the x-y plane is given by

$$s(t) = \int M_0(x,y) e^{-i(k_x(t)x + k_y(t)y)} dxdy \tag{2.36}$$

where $k_{x(y)}(t) = \gamma \int_0^t G_{x(y)}(t')dt'$ is a time varying spatial frequency variable (k-space)[38, 39] with units rad/cm. Analogous to the small-tip-angle approximation for excitation, the acquired signal $s(t)$ and magnetization $M_0(x,y)$ form a Fourier transform pair. The sampled signal at time t corresponds to the Fourier transform of $M_0(x,y)$ at k-space coordinate $(k_x(t), k_y(t))$ or equivalently the amount of spatial frequency $k_x(t)\hat{x} + k_y(t)\hat{y}$ contained in $M_0(x,y)$. Thus, sampling the signal $s(k_x(t), k_y(t))$ along a trajectory determined by the time integral of the applied gradients that sufficiently covers k-space and taking its inverse 2D Fourier transform, one can recover $M_0(x,y)$.

Spatial encoding using FIDs have some limitations such as high loss of signal in the presence of field inhomogeneity and sampling artifacts due to finite rise time of encoding gradients. This can be overcome using an "echo", in which the signal is sampled after preparation of spatial encoding by realigning the spatially dependent linear phase[40]. Two methods commonly used are the gradient-echo technique and spin-echo technique. In the gradient induced echo, the spins are synthetically dephased and rephased using gradients, coming into focus when the area of the rephasing gradient equals the total area of the dephasing gradient and forming an echo. A spin-echo[41] is formed by applying a 180° inversion pulse at time τ after excitation, which effectively time reverses the phase accrued between excitation and inversion, thus refocusing the spins at $t = 2\tau$.

In order to faithfully reconstruct an image, k-space must be sufficiently sampled. For Cartesian coordinates, this is often done by acquiring a series of parallel k-space lines along the frequency-encode direction. Specifically, after selective slab excitation, starting from the origin, the k-coordinate shifts along a trajectory determined by the time integral of the gradients applied during the preparation phase, which de-phase the spins and sets up the starting point for acquisition. A

line of k-space is then acquired while the spins re-phase and form an echo via read-out gradients. The next line of k-space is sampled by choosing a different starting point, usually an increment of Δk along the phase-encode direction, followed by acquisition of another line of k-space. This is repeated until k-space is completely covered. Following the reciprocity relation of the discrete Fourier transform, for a fixed resolution determined by the number of sampled points N, the field-of-view (FOV), which is the maximum distance in image space, is given by FOV $= \frac{1}{\Delta k}$, and the pixel size $\left(= \frac{\text{FOV}}{N} \right)$ is given by $\Delta x = \frac{1}{k_{\max}}$, where Δk is the spacing between samples in k-space and $k_{\max} = 2N\Delta k$ is the maximum k-space sample. To better illustrate, Fig. 2.10 shows the sequence diagram and corresponding k-space sampling for a gradient echo, along with snapshots of the imposed spatial frequency on the spins at different time points during the sequence. Actual *in-vivo* data of acquired k-space and resulting brain image is shown as well.

2.5.4 Spectroscopic Imaging

Spectroscopic imaging aims to detect the local chemical shift content within an imaging voxel across multiple voxels, providing a spatial map of the spectroscopic information across a region of interest. This is achieved by treating the additional phase accrued due to chemical shift as a separate dimension independent of spatial encoding. In *chemical shift imaging* (CSI)[42], phase encoding is applied prior to signal acquisition. For one-dimensional spatial encoding (1D-CSI), applying a constant amplitude phase-encode gradient of duration τ_{PE} along the direction of spatial encode, say the x-axis, different compounds at different spatial locations will acquire different phases $(= \gamma G_x \tau_{\text{PE}} x = k_x x)$, resulting in the signal

$$s(k_x, t) = \int M_0(x, \sigma) e^{-i(k_x x - \sigma\omega_0 t)} dx d\sigma \tag{2.37}$$

Taking the Fourier transform with respect to time for each phase encode step results in a set of spectra that has spatially varying phase for each chemical shift. An extra Fourier transform along the phase-encode direction will unwrap

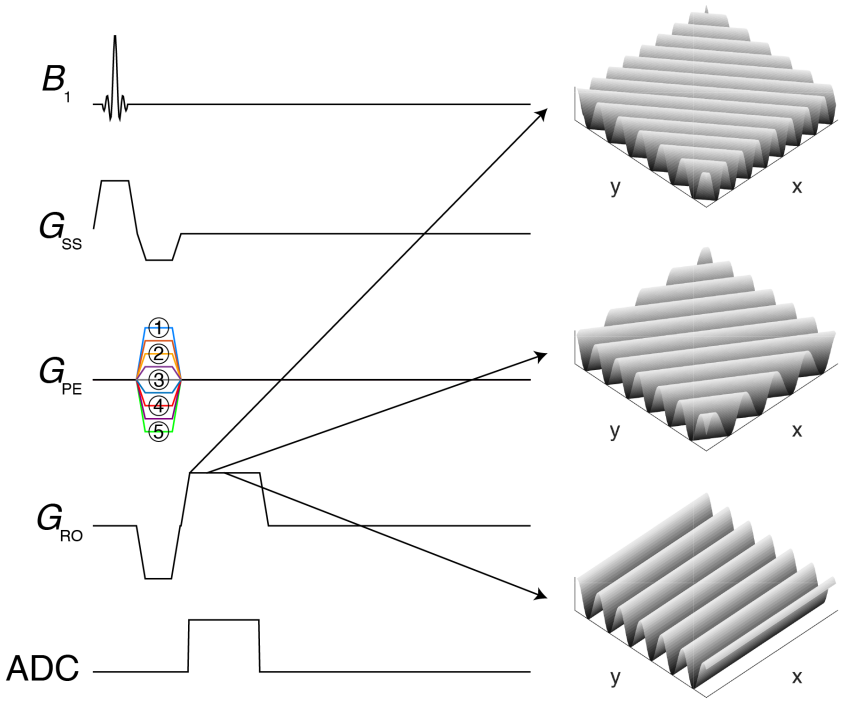

(a)

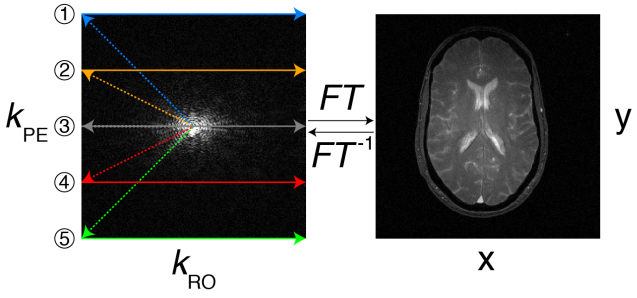

(b)

Figure 2.10: (**a**) Sequence diagram of a gradient echo (GRE) sequence and snapshots of spatial frequency imposed at different times during readout for $k_{\mathrm{PE}} = -\frac{3}{4}k_{\mathrm{max}}$ (G_{PE} color-coded in purple). Prior to acquisition, spatial encode is prepared by de-phasing spins using phase-encode and readout gradients, which determine the starting point for each line of k-space acquired. (**b**) *in-vivo* k-space data and reconstructed image. The numbers denote the corresponding line of k-space acquired for different G_{PE}.

the spatial distribution for all chemical shifts $M_0(x, \sigma)$. Extension to two- and three-dimensions is be done by adding extra phase-encode gradients along the orthogonal direction(s).

2.6 ^{31}P Cardiac Spectroscopy

In the heart, there is a constant coupling and balancing of energy production, transportation and utilization. As the organ that consumes the most amount of energy, being able to detect these energy metabolites is important in elucidating these mechanisms. Fortunately, phosphorus ^{31}P NMR spectroscopy provides a mean to non-invasively measure adenosine triphosphate (ATP), the currency of energy, phosphocreatine (PCr), and inorganic phosphate (Pi).

The ATP produced in the mitochondria through oxidative phosphorylation is transferred to the site of energy utilization in the form of PCr[43]. Creatine kinase (CK) facilitates the phosphorylation of creatine (Cr) through ATP in the mitochondria to create PCr. PCr is transported through intracellular space to the myofibrils in the cystol. Upon arrival, PCr combines with adenosine diphosphate (ADP) in the myofibril and generates ATP. The unphosphorylated Cr subsequently returns to the mitochondria site, where it phosphorylates again (Fig. 2.11).

$$\mathrm{Cr} + \mathrm{ATP} \overset{\mathrm{CK}}{\rightleftarrows} \mathrm{PCr} + \mathrm{ADP} + \mathrm{H}^{+} \tag{2.38}$$

In addition to serving as an intracellular spatial energy shuttle, due to the CK reaction rate far exceeding that of ATPase[44, 45, 46, 47], it also functions as a temporal buffer by maintaining constant ATP levels available for consumption, even during periods of heavy demand. Energy utilization occurs when the transferred ATP pool undergoes hydrolysis via cytosolic ATPase, where it produces a by-product Pi while releasing energy:

$$\mathrm{ATP} \overset{\mathrm{ATPase}}{\longrightarrow} \mathrm{ADP} + \mathrm{Pi} + \mathrm{Energy} \tag{2.39}$$

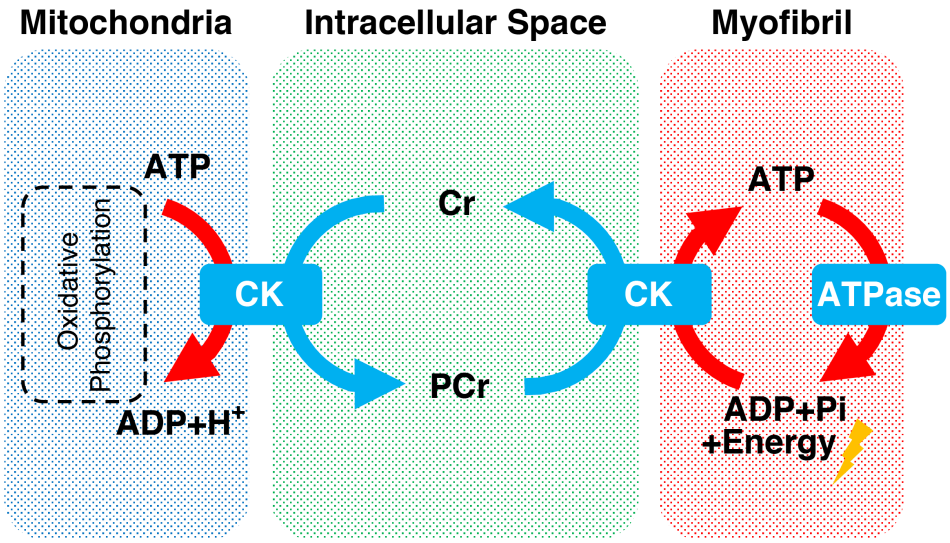

Figure 2.11: Flow diagram depicting CK shuttling. CK catalyzes the mitochondria ATP phosphorylation of Cr and produces PCr. PCr travels through intracellular space where upon arrival at the myofibril, it combines with myofibril ADP via CK to produce ATP. The resulting ATP is used to support muscular contraction utilizing the energy released from undergoing hydrolysis via ATPase.

This energy is in turn utilized to generate force needed to support muscle contraction of cardiomyocytes.

The ratio between PCr and ATP is an important indicator for predicting mortality in patients with heart failure[7]. Compared to the normal heart, the PCr-to-ATP ratio decreases in diseased hearts and is accompanied by an overall reduction of high energy phosphate (HEP) levels. For example, using a porcine model of postinfarction left ventricle remodeling (LVR) by acute coronary occlusion, it was shown that the PCr/ATP ratio decreases significantly in patients that developed into congestive heart failure (CHF)[9, 10]. Furthermore, in studies aimed at therapeutically combating heart disease, normalization of the myocardial energetics was observed, where the PCr/ATP ratio increased significantly in response to stem cell transplant[48, 49], supporting feasibility for further use as a criterion for determining therapy effectiveness.

2.6.1 Magnetization Saturation Transfer

The reaction rates and fluxes serve as an important measure for characterizing the dynamics of metabolic process. For example, previous work[50] have shown that inhibiting CK decreased the contractile reserve, which is consistent with other previous studies showing that failing hearts have a decreased energy reserve[11, 51]. For high energy phosphates, the reaction rate constant going from PCr to ATP can be measured utilizing magnetization saturation transfer (MST) techniques[45, 52, 53]. Consider the chemical exchange between PCr and ATP at equilibrium:

$$\mathrm{PCr} \underset{k_{\mathrm{r,CK}}}{\overset{k_{\mathrm{f,CK}}}{\rightleftarrows}} \mathrm{ATP} \tag{2.40}$$

where $k_{\mathrm{f,CK}}$ and $k_{\mathrm{r,CK}}$ are the pseudo-first-order forward and reverse rate constants for CK reaction with units s^{-1}. Since the product of the forward rate constant with PCr concentration, [PCr], is the forward flux rate ($k_{\mathrm{f,CK}}$[PCr]) for generating ATP from ADP, $k_{\mathrm{f,CK}}$ is the fractional turn over rate at which PCr is converted to ATP. Accordingly, the evolution of the PCr spin magnetization, with chemical exchange, is given by the modified Bloch-McConnell equations[54]:

$$\frac{\partial M_{\mathrm{PCr}}(t)}{\partial t} = \frac{M_{0,\mathrm{PCr}} - M_{\mathrm{PCr}}(t)}{T^{\mathrm{int}}_{1,\mathrm{PCr}}} - k_{\mathrm{f,CK}} M_{\mathrm{PCr}}(t) + k_{\mathrm{r,CK}} M_{\mathrm{ATP}}(t) \tag{2.41}$$

where $M_{0,\mathrm{PCr}}$ is the equilibrium magnetization and $T^{\mathrm{int}}_{1,\mathrm{PCr}}$ is the longitudinal relaxation constant in the absence of chemical exchange. By selectively saturating ATP, having yet to fully recover due to T_1 relaxation, the chemical exchange from ATP is removed, thereby decreasing the longitudinal magnetization of PCr. Erasing the reverse reaction (PCr←ATP), the last term in Eq. (2.41) is eliminated. Solving this differential equation, the longitudinal magnetization in the absence of reverse chemical exchange is given by

$$M_{\mathrm{PCr}}(t) = M_{0,\mathrm{PCr}} \left[\frac{T^{\mathrm{app}}_{1,\mathrm{PCr}}}{T^{\mathrm{int}}_{1,\mathrm{PCr}}} + \left(1 - \frac{T^{\mathrm{app}}_{1,\mathrm{PCr}}}{T^{\mathrm{int}}_{1,\mathrm{PCr}}} \right) e^{-\frac{t}{T^{\mathrm{app}}_{1,\mathrm{PCr}}}} \right] \tag{2.42}$$

where $T_{1,\mathrm{PCr}}^{\mathrm{app}}$ is the apparent longitudinal relaxation time when ATP is continuously saturated, given by $\frac{1}{T_{1,\mathrm{PCr}}^{\mathrm{app}}} = \frac{1}{T_{1,\mathrm{PCr}}^{\mathrm{int}}} + k_{\mathrm{f,CK}}$. $T_{1,\mathrm{PCr}}^{\mathrm{app}}$ is measured over multiple progressive MST acquisitions in which saturation time is varied and curve fitted to Eq. (2.42). In the steady-state MST experiment $\left(\frac{\partial M_{\mathrm{PCr}}(t)}{\partial t} = 0\right)$, which is achieved by saturating ATP for an "infinitely long" time (usually 3−5 times of $T_{1,\mathrm{PCr}}^{\mathrm{app}}$), the forward CK rate constant can be calculated from:

$$k_{\mathrm{f,CK}} = \left(\frac{M_{0,\mathrm{PCr}} - M_{\mathrm{ss,PCr}}}{M_{0,\mathrm{PCr}}}\right) / T_{1,\mathrm{PCr}}^{\mathrm{app}} \tag{2.43}$$

where $M_{\mathrm{ss,PCr}}$ is the equilibrium magnetization with ATP saturated. Knowing $k_{\mathrm{f,CK}}$ and $T_{1,\mathrm{PCr}}^{\mathrm{app}}$, $T_{1,\mathrm{PCr}}^{\mathrm{int}}$ can thus be easily extracted. Progressive MST is the gold standard for measuring intrinsic T_1 values when chemical exchange is involved.

Fortunately, previous studies have shown that $T_{1,\mathrm{PCr}}^{\mathrm{int}}$ is constant among subjects with different physiological and pathological conditions[45, 11, 55, 56]. Based on this, knowing $T_{1,\mathrm{PCr}}^{\mathrm{int}}$, a single steady-state MST experiment is sufficient in measuring the forward rate constant using the following equation, forgoing the need to conduct progressive MST, which can be extremely time consuming.

$$k_{\mathrm{f,CK}} = \left(\frac{M_{0,\mathrm{PCr}} - M_{\mathrm{ss,PCr}}}{M_{\mathrm{ss,PCr}}}\right) / T_{1,\mathrm{PCr}}^{\mathrm{int}} \tag{2.44}$$

2.6.2 T_1^{nom} Method for Rapid k_{f} Measurement and Quantification

The inefficient signal-to-noise (SNR) ratio per unit time of the traditional magnetization saturation transfer experiment is largely due to both the longitudinal magnetization with (M_{ss}) and without saturation (M_0) defined as being in a fully relaxed state. For ^{31}P metabolites such as PCr and ATP, the long intrinsic T_1 (T_1^{int}) can make certain measurements physiologically impractical, such as when trying to obtain spatial localization. To recompense for this lengthy acquisition, Bottomley et al introduced the Four-Angle Saturation Transfer (FAST) method where the kinetic reaction rate constants were extracted using 4 partially relaxed

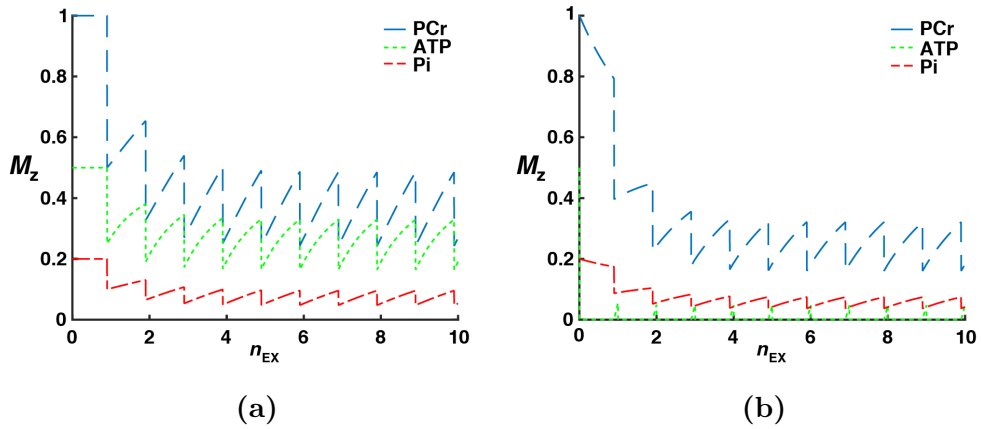

Figure 2.12: Numerical simulation of longitudinal magnetization achieving steady-state under partial relaxation. (**a**) Without ATP saturation and (**b**) with ATP saturation. Spin parameters used: PCr:ATP:Pi = 1:0.5:0.2, T_1^{int} used for PCr, ATP, and Pi are 3.2 s, 1.1 s, and 3 s respectively. Sequence parameters FA = 60°, TR = 1 s, d_1 = 0.1 s.

measurements with high SNR, drastically shortening acquisition time[57]. Xiong et al demonstrated an approach that optimizes the presaturation delay to minimize saturation time, thus significantly reducing repetition time and total acquisition time[58].

The T_1^{nom} method[4] enables rapid acquisition of enzyme kinetics utilizing MST experiment in a partially relaxed state with arbitrary flip angle (FA) and repetition time (TR). Under this partially relaxed condition, the longitudinal magnetization will attain a new steady-state under both without (M_{c}) and with saturation (M_{s}) applied, as shown in Fig. 2.12. Due to this new partially relaxed steady-state, the linear relation between the M_0/M_{ss} and the forward rate constant k_{f} under full relaxation given by

$$\frac{M_0}{M_{\text{ss}}} = 1 + T_1^{\text{int}} k_{\text{f}} \tag{2.45}$$

is no longer valid.

Figure 2.13 are the numeric simulation results obtained using various acquisition parameters (FA and TR) and k_{f} for a fixed spin system and delay after

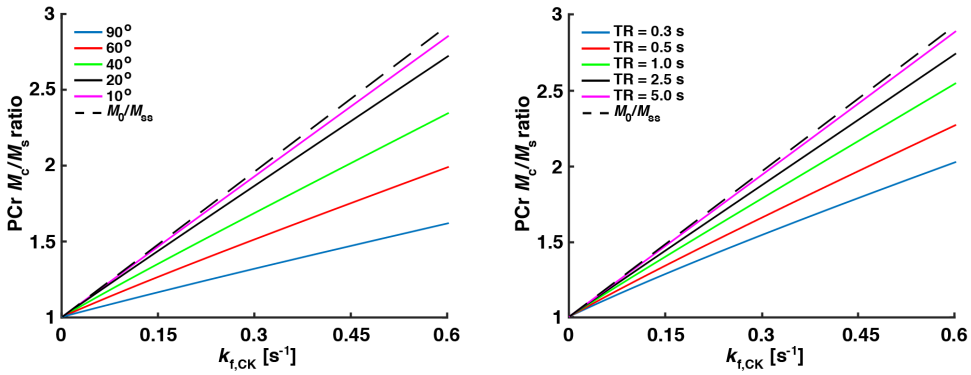

(a) **(b)**

Figure 2.13: Numerical simulation of M_c/M_s vs. $k_{f,CK}$ for ATP saturation. (a) FA and (b) TR dependence. $k_{f,CK}$ was swept from 0∼0.6 s^{-1} to show that the intercept occurs at 1. Fully relaxed state is indicated by dashed line (M_0/M_{ss}) in which the slope is equal to T_1^{int}. Same spin system and sequence parameters that were used in Fig. 2.12. Linear relationship between M_c/M_s and $k_{f,CK}$ is observed.

excitation (d_1). As can be seen, a new approximate linear relationship under partial relaxation is established given by

$$\frac{M_c}{M_s} \approx \beta + T_1^{nom} k_f \tag{2.46}$$

where the intercept β is usually within 5% of 1 and T_1^{nom} is the slope. Comparing Eqs. (2.45) and (2.46), it is seen that the empirical parameter T_1^{nom} accounts for the effects due to partial relaxation. Although there is no analytical expression for calculating T_1^{nom}, it is in general a function of spin system parameters (relative pool size and its respective T_1^{int}) and sequence parameters (FA, TR and d_1).

Chapter 3

Transmurally Differentiated Measurement of ATP Hydrolysis Rates in the *in vivo* Porcine Hearts

This is a manuscript accepted for publication in Magnetic Resonance in Medicine.

3.1 Introduction

Adverse changes in cellular ATP metabolism are known to contribute to the progression of myocardial dysfunction in patients with left ventricular (LV) hypertrophy and heart failure [59, 60, 61, 62, 63, 64, 7, 65]. Until recently, attempts to test this hypothesis have been largely unsuccessful due to techniques for monitoring ATP hydrolysis (ATP $\rightarrow$ ADP + Pi) in the hearts of living animals being unavailable. In principle, the rate of ATP hydrolysis can be measured utilizing phosphorous-31 MR spectroscopy (^{31}P MRS) magnetization saturation transfer (^{31}P MRS-MST) experiments. However, the conventional approach requires

quantification of inorganic phosphate (Pi) levels, which is difficult to achieve, because Pi levels in the myocardium are low, and the resonance peaks of Pi and 2,3-diphosphoglycerate (2,3-DPG) from the erythrocytes overlap in the ^{31}P MR spectrum [66]. We have very recently developed a novel ^{31}P MRS-MST method that bypasses this need to quantify Pi levels when measuring the ATP hydrolysis rate, and have used this approach to show that the rate of myocardial ATP hydrolysis at the peri-scar border zone (BZ) is significantly decreased in the hearts of swine with experimentally induced ischemia reperfusion injury [3]. Our results also indicated that the functional improvements associated with the administration of cell therapy to injured swine hearts were accompanied by reduction of LV wall stress and improvement in BZ ATP hydrolysis rate [3].

In hearts, although the inner (ENDO, subendocardial) and outer (EPI, subepicardial) layers are known to differ substantially in perfusion, metabolism, and contractile activity [67, 68], few cardiovascular investigations have been able to evaluate how the properties of myocardial metabolism and the response to myocardial injury may vary across the thickness of the ventricular wall. Some evidence suggests that these variations may be accompanied by differences in cellular energetics. For example, flow-limiting coronary stenosis appears to reduce cellular energy levels more substantially in the ENDO than in the EPI [67], which may suggest that the inner layer is more vulnerable to ischemia, while the induction of a high cardiac work state through catecholamine infusion led to more prominent increases in blood flow and energy consumption in the subepicardium with a uniform distribution across the LV wall of the myocardial phosphorylation potential [69, 70, 71]. Observations can also vary depending on the method used to elevate the heart rate: stenosis with dobutamine-induced elevations reduced energy levels in both layers, with the greatest decline observed in the EPI layers, whereas combining stenosis with pacing-induced tachycardia reduced energy levels more pronouncedly in the ENDO layers [72].

It remains a significant clinical question why the inner layers of the myocardium across the left ventricle are more susceptible to an ischemia insult [73].

Although these series of bioenergetic evaluations convincingly shows that the myocardial ischemic and oxidative stress responses are not uniform across the thickness of the left ventricular wall, the observations were generally limited to measurements of the steady state levels of myocardial high-energy-phosphate (HEP), rather than the kinetics of the ATP turnover rate. The transmurally differentiated evaluations of the myocardial ATP turnover rate is important for examining the mechanisms of myocardial ischemia or metabolic diseases. Difficulty in measuring myocardial inorganic phosphate has been a major barrier in examining the transmural gradient of the reserve of myocardial ATP hydrolysis rate, and whether this gradient contributes to the progression of cardiac failure in hearts with compensated hypertrophy (add 18)[74, 75], a subject still of much debate. Thus, for the experiments presented in this report, we used ^{31}P MRS-MST to compare the EPI and ENDO ATP hydrolysis rates under both baseline and catecholamine induced high cardiac workload states.

We also introduce a modified version of our 31P MRS protocol that enables us to perform our rate calculations from partially relaxed spectra: the T_1^{nom} method, which was recently established [4]. The implementation of T_1^{nom} effectively reduced the time required for data acquisition by up to an order of magnitude.

3.2 Theory

^{31}P MRS-MST Assessments of Myocardial ATP Turnover Rates from Partially Relaxed Spectra

Cellular ATP levels are maintained by the activity of creatine kinase (CK), which catalyzes the interconversion of PCr and ATP, and by cellular ATP synthases (ATPase), which catalyzes the metabolic pathways responsible for ATP production (ADP + Pi $\rightarrow$ ATP) and consumption (ATP $\rightarrow$ ADP + Pi). Thus, the kinetics of ATP metabolism can be summarized with the following model:

$$[\text{PCr}] \underset{k_{\text{r,CK}}}{\overset{k_{\text{f,CK}}}{\rightleftharpoons}} [\text{ATP}] \underset{k_{\text{f,ATPase}}}{\overset{k_{\text{r,ATPase}}}{\rightleftharpoons}} [\text{Pi}]$$

where k_{f} and k_{r} are pseudo first-order rate constants for the indicated forward

and reverse reactions, respectively. Because the PCr $\leftrightarrow$ ATP reaction is at equilibrium under steady-state condition, the ATP hydrolysis rate (ATP $\rightarrow$ ADP + Pi) can be calculated by subtracting the flux of the PCr $\rightarrow$ ATP reaction from the flux of the combined ATP $\rightarrow$ Pi and ATP $\rightarrow$ PCr reactions $\mathit{flux}_{\mathrm{ATP,total}}$ (i.e., $\mathit{flux}_{\mathrm{r,ATPase}} = \mathit{flux}_{\mathrm{ATP,total}} - \mathit{flux}_{\mathrm{f,CK}}$) [3]. The fluxes, in turn, can be calculated from the concentrations of the reactants and from MRS measurements of the corresponding rate constants, which are determined utilizing the following equations:

$$k_{\mathrm{ATP,total}} = \left(\frac{M_{0,\mathrm{ATP}}}{M_{\mathrm{ss,ATP}}} - 1\right) / T_{1,\mathrm{ATP}}^{\mathrm{int}} \tag{3.1}$$

$$k_{\mathrm{f,CK}} = \left(\frac{M_{0,\mathrm{PCr}}}{M_{\mathrm{ss,PCr}}} - 1\right) / T_{1,\mathrm{PCr}}^{\mathrm{int}} \tag{3.2}$$

$$k_{\mathrm{r,ATPase}} = \left(\frac{M_{0,\mathrm{ATP}}}{M_{\mathrm{ss,ATP}}} - 1\right) / T_{1,\mathrm{ATP}}^{\mathrm{int}} - \frac{M_{0,\mathrm{PCr}}}{M_{0,\mathrm{ATP}}} k_{\mathrm{f,CK}} \tag{3.3}$$

where M_{ss} and M_0 are the fully relaxed magnetizations with (M_{ss}) and without (M_0) saturation, and T_1^{int} is the intrinsic longitudinal relaxation time. T_1^{int} is exceptionally long for PCr and ATP and, consequently, the acquisition time required for accurate assessments of $k_{\mathrm{f,CK}}$ and $k_{\mathrm{r,ATPase}}$ can be prohibitive, particularly when attempting to differentiate between measurements obtained in the epicardial and endocardial layers of the ventricular wall. To decrease this unrealistic acquisition time, the T_1^{nom} method can be employed. By determining a correction factor, T_1^{nom} enables calculating the rate constants from partially relaxed spectra, thereby dramatically reducing the acquisition time. The validity of using this method is presented in the following.

In the case of double saturating PCr and Pi, mathematically, the Bloch McConnell equations for ATP become equivalent to the case of single saturation of

ATP for PCr(Pi),

$$\begin{aligned}\frac{dM_{\mathrm{PCr(Pi)}}(t)}{dt} &= \left(\frac{M_{0,\mathrm{PCr(Pi)}} - M_{\mathrm{PCr(Pi)}}(t)}{T^{\mathrm{int}}_{1,\mathrm{PCr(Pi)}}}\right) - k_{\mathrm{f,CK(ATPase)}} M_{\mathrm{PCr(Pi)}}(t) \\ \frac{dM_{\mathrm{ATP}}(t)}{dt} &= \left(\frac{M_{0,\mathrm{ATP}} - M_{\mathrm{ATP}}(t)}{T^{\mathrm{int}}_{1,\mathrm{ATP}}}\right) - k_{\mathrm{ATP,total}} M_{\mathrm{ATP}}(t)\end{aligned} \tag{3.4}$$

where $k_{\mathrm{ATP,total}} = k_{\mathrm{r,CK}} + k_{\mathrm{r,ATPase}}$. Hence, the same linear relation between the partially relaxed magnetization without and with saturation ratio ($M_{\mathrm{c}}/M_{\mathrm{s}}$), and rate constant $k_{\mathrm{ATP,total}}$ is observed, and is therefore plausible to apply the T_1^{nom} method to ATP in a partially relaxed state for double saturation. This was verified for the B_1-*I*nsentitive *TR*ain to *O*bliterate signal (BISTRO) pulse sequence (add 22), a train of pulses interleaved with crusher gradients used to selectively saturate a target frequency before excitation, which is then followed by a delay (d_1) as shown in Figure 3.1. Spin parameters PCr:ATP:Pi = 1:0.48:0.20, $T^{\mathrm{int}}_{1,\mathrm{PCr}} = 3.2$ s, $T^{\mathrm{int}}_{1,\mathrm{ATP}} = 1.1$ s, $T^{\mathrm{int}}_{1,\mathrm{Pi}} = 3$ s were numerically simulated for flip angle (FA) of 90°, repetition time (TR) of 2.5 s, and delay of 0.052 s (Fig. 3.2). Under partially relaxed state, the longitudinal magnetization of PCr, ATP, and Pi reach a steady state in both without (Fig. 3.2a) and with (Fig. 3.2b) PCr-Pi double saturation. Parallel to ATP single saturation [4], the empirical T_1^{nom} parameter is a function of spin system parameters (T_1^{int} and pool size ratios of metabolites) and pulse sequence acquisition parameters, and intercepts the $M_{\mathrm{c}}/M_{\mathrm{s}}$-axis at 1. Based on this, in steady-state, the equations used to calculate T_1^{nom} for ATP and PCr(Pi) from partially relaxed MR spectra are:

$$T^{\mathrm{nom}}_{1,\mathrm{PCr(Pi)}} = \left(\frac{M_{\mathrm{c,PCr(Pi)}}}{M_{\mathrm{s,PCr(Pi)}}} - 1\right) / k_{\mathrm{f,CK(ATPase)}} \tag{3.5}$$

$$T^{\mathrm{nom}}_{1,\mathrm{ATP}} = \left(\frac{M_{\mathrm{c,ATP}}}{M_{\mathrm{s,ATP)}}} - 1\right) / k_{\mathrm{ATP,total}} \tag{3.6}$$

and when this correction factor is incorporated into Eqs. (3.1)(3.2)(3.3), the modified equations for calculating $k_{\mathrm{f,CK}}$ and $k_{\mathrm{r,ATPase}}$ from partially relaxed spectra

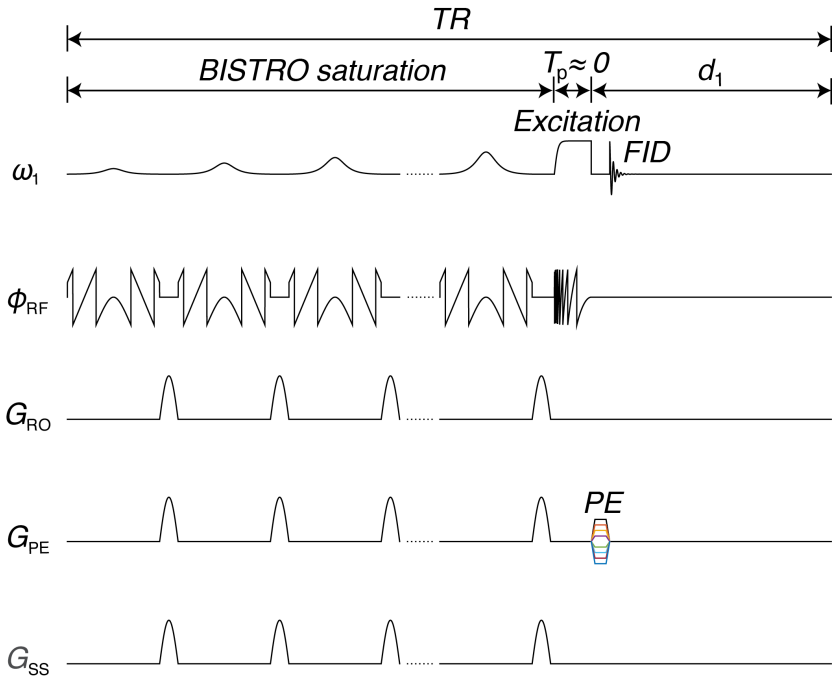

Figure 3.1: BISTRO pulse sequence used in partially relaxed MST experiment. A train of adiabatic full-passage (AFP) pulses interleaved with crusher gradients achieves selective saturation of target frequency. This is sequentially followed by excitation, phase encode, and readout. Length of excitation pulse is assumed to be negligible ($T_\mathrm{p} \approx 0$). For the control spectrum, the power of the pulse train is turned off.

become:

$$k_{\mathrm{f,CK}} = \left(\frac{M_{\mathrm{c,PCr}}}{M_{\mathrm{s,PCr}}} - 1 \right) / T_{1,\mathrm{PCr}}^{\mathrm{nom}} \tag{3.7}$$

$$k_{\mathrm{r,ATPase}} = \left(\frac{M_{\mathrm{c,ATP}}}{M_{\mathrm{s,ATP}}} - 1 \right) / T_{1,\mathrm{ATP}}^{\mathrm{nom}} - \frac{M_{0,\mathrm{PCr}}}{M_{0,\mathrm{ATP}}} k_{\mathrm{f,CK}} \tag{3.8}$$

where M_s and M_c are the partially relaxed magnetizations with (M_s) and without (M_c) saturation, respectively.

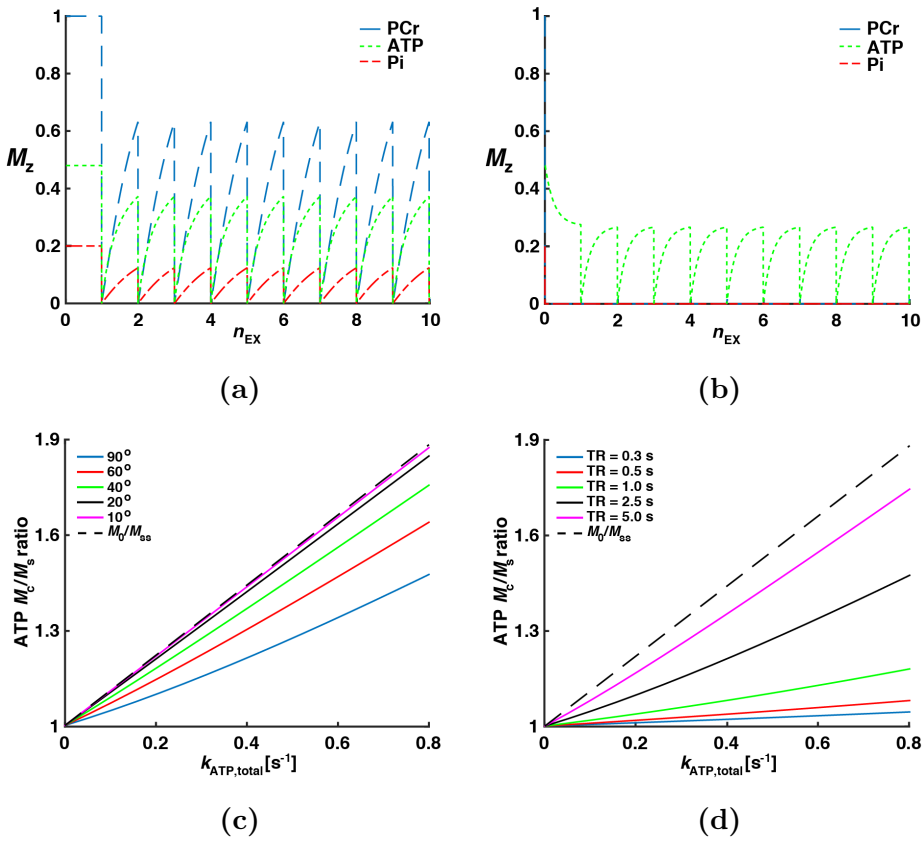

Figure 3.2: Numerical simulation of the T_1^{nom} method for PCr-Pi double saturation. Longitudinal magnetizations without saturation (M_c) (**a**) and with PCr-Pi double saturation (M_s) (**b**) as a function of number of excitations (n_{EX}) achieve steady-state. Spin system parameters used: PCr:ATP:Pi = 1:0.48:0.2; $T_{1,\text{PCr}}^{\text{int}} = 3.2$ s, $T_{1,\text{ATP}}^{\text{int}} = 1.1$ s and $T_{1,\text{Pi}}^{\text{int}} = 3.0$ s. Chemical exchange parameters: $k_{\text{f,CK}} = 0.3$ s^{-1}; $k_{\text{f,ATPase}} = 0.18$ s^{-1}. Acquisition parameters: TR = 2.5 s, FA = 90° , $d_1 = 0.052$ s. Simulated M_c/M_s ratio vs. $k_{\text{ATP,total}} = k_{\text{r,CK}} + k_{\text{r,ATPase}}$ dependence on FA (**c**) and TR (**d**). $k_{\text{f,CK}}$ was swept from 0∼0.6 s^{-1}, with $k_{\text{f,ATPase}} = 0$ to show that the intercept occurs at 1. Fully relaxed state is indicated by dashed line (M_0/M_{ss}) in which the slope is equal to $T_{1,\text{ATP}}^{\text{int}}$. Sweeping $k_{\text{f,CK}}$ with $k_{\text{r,ATPase}} \neq 0$ produces identical result. Same spin system parameters and delay were used. Linear relationship between M_c/M_s and $k_{\text{ATP,total}}$ as observed in the single ATP saturation case confirms that the T_1^{nom} method can be applied for double saturation.

3.3 Methods

All experimental protocols were approved by the University of Minnesota Research Animal Resources Committee. Experimental and animal maintenance procedures were in agreement with the Animal Use Guidelines of the University of Minnesota and consistent with the National Institutes of Health *Guide for the Care and Use of Laboratory Animals* (NIH publication No. 85-23).

Animal Preparation

Female Yorkshire swine (∼21 kg) were anesthetized with inhaled 2% isoflurane, intubated, and ventilated with a respirator and supplemental oxygen; the animals arterial blood pressure, left ventricle pressure, and blood oxygen levels were monitored throughout all surgical and MRS procedures. A left thoracotomy was performed to expose the heart, and polyvinyl chloride catheters (3 mm outer diameter) were inserted into the ascending aorta (through the left external carotid artery) and LV (through the apical dimple) for hemodynamic monitoring and drug administration. A double-tuned (^{1}H and ^{31}P), 28-mm diameter surface coil was sutured on to the epicardium over the anterior wall of the left ventricle; then, the coil was tuned and matched, and the animal was placed on a cradle and inserted into the magnet bore. MR experiments were performed under both baseline cardiac workload and high cardiac workload which was induced through intravenous infusion of dopamine and dobutamine (10 μg/kg per min each) from a syringe pump (PHD 2000; Harvard Apparatus, Holliston, MA); high-workload assessments were performed ∼10 min after infusion was initiated.

MR Spectroscopic Imaging

MR spectra were obtained with a 9.4 Tesla (T), 65-cm bore magnet (Magnex Scientific, Oxford, UK) interfaced with a VnmrJ console (Agilent Technologies, Santa Clara, CA). Gradient echo (GRE) images were obtained and used both for positioning the probe to the isocenter of the magnet and for planning acquisition

of the chemical shift imaging (CSI) sequence; B_0 shimming was performed via proton signal detection, and the center frequency offset between PCr and ATP was determined from global ^{31}P spectra acquired with a 1 ms adiabatic pulse to ensure uniform spin rotations within the sensitive volume of the surface coil. After acquisition of fully relaxed global control spectra (TR = 12 s, number of averages [nt] = 16, spectral width [SW] = 10 kHz), magnetization-saturation-transfer experiments were performed in the absence of saturation, with ATP saturation, and with both PCr and Pi simultaneous saturation (TR = 6.8 s, nt = 16, d_1 = 1.51 s, and SW = 10 kHz). Saturation was achieved by using the BISTRO pulse sequence (22). ATP was excited with a frequency selective hyperbolic secant pulse, and PCr and Pi were simultaneously saturated with a composite pulse consisting of two distinct hyperbolic secant pulses with different excitation frequencies; the composite pulse was validated using Bloch simulations to ensure that adjacent peaks were not significantly excited. The carrier frequency for saturation and excitation was positioned between the chemical-shift frequencies of PCr and ATP. Having these measurements at hand, calculation of the rate constants $k_{\mathrm{f,CK}}$ and $k_{\mathrm{ATP,total}}$ using Eqs. (3.1)(3.2)(3.3) assuming $T^{\mathrm{int}}_{1,\mathrm{PCr}} = 3.2$ s and $T^{\mathrm{int}}_{1,\mathrm{ATP}} = 1.1$ s [3] was carried out.

Each epicardial and endocardial measurement was calculated from three sets of 1D-CSI spectra: (i) spectrum obtained in the absence of saturation ($M_{\mathrm{c,PCr}}$ and $M_{\mathrm{c,ATP}}$), (ii) "single-saturation" spectrum ($M_{\mathrm{s,PCr}}$) obtained with saturation applied at the ATP resonance frequency, and (iii) "double-saturation" spectrum ($M_{\mathrm{s,ATP}}$) obtained with saturation applied at both the PCr and Pi resonance frequencies (field of view [FOV] 4 cm, $d_1 = 0.05174$ s, $n_{\mathrm{PE}} = 17$, SW = 10 kHz, nt = 12). T_1^{nom} was experimentally obtained as follows: three additional global spectra, control, single-, and double-saturation, were acquired using identical sequence parameters that were used in CSI, yielding global $M_{\mathrm{c,PCr}}/M_{\mathrm{c,ATP}}$, $M_{\mathrm{s,PCr}}$, and $M_{\mathrm{s,ATP}}$ in partially relaxed states, respectively. To accommodate for the recovery of longitudinal relaxation that occurs during the CSI phase encode period, a delay equivalent to the phase encode time ($\tau_{\mathrm{PE}} = 536\ \mu$s) was inserted between excitation

and acquisition to compensate.

Combining these measurements with the global rate constants obtained from above, T_1^{nom} for both PCr and ATP were calculated using Eqs. (3.5) and (3.6). These T_1^{nom} values were then incorporated to the measurements obtained from the three CSI MST experiments to calculate $k_{\text{f,CK}}$ and $k_{\text{r,ATPase}}$ using Eqs. (3.7) and (3.8) for each transmural layer. PCr/ATP ratio obtained from the control spectra under these conditions were used to calculate the normalization factor between fully relaxed and partially relaxed states by dividing it by the fully relaxed ratio initially obtained. A flow chart depicting this process is given in Figure 3.3. Motion artifacts were minimized by gating NMR acquisition to coincide with both the diastolic state of the cardiac cycle and the expiration state of the respiratory cycle. Because excitation flip angle was 90°, no dummy scans were needed to achieve steady-state. To ensure that the delay between the last BISTRO pulse and the excitation pulse was minimized (thereby maximizing saturation), an optimal TR was determined from assessments of the animals heart and respiratory rates, and the number of BISTRO pulses was adjusted accordingly. In our studies, the optimal TR ranged from 2.369 - 3.525 s, $T_{1,\text{ATP}}^{\text{nom}}$ and $T_{1,\text{PCr}}^{\text{nom}}$ ranged from 0.18 - 0.53 s and 1.11 - 2.15 s, respectively, at baseline condition, resulting in a typical study lasting on average 45 - 60 min.

MR Data Analysis

CSI data were reconstructed using in-house software programmed in MATLAB (MathWorks, Inc., Natick, MA). The transmural series of spectra (N = 17) was averaged with 6 Fourier-series windows [76] to generate representative epicardial and endocardial spectra with no voxel in between, resulting in a voxel width of 0.67 cm. It was confirmed through numerical simulations of the slice profile constructed from Fourier-series windows that the adjacent voxel signal contamination was less than 3%. Resonance peaks were integrated and quantified using the data analysis toolkit provided by the VnmrJ software. The ATP hydrolysis rate ($\mathit{flux}_{\text{r,ATPase}} = [\text{ATP}]k_{\text{r,ATPase}}$) was calculated based on an ATP concentration of 5.3 μmol/g (as

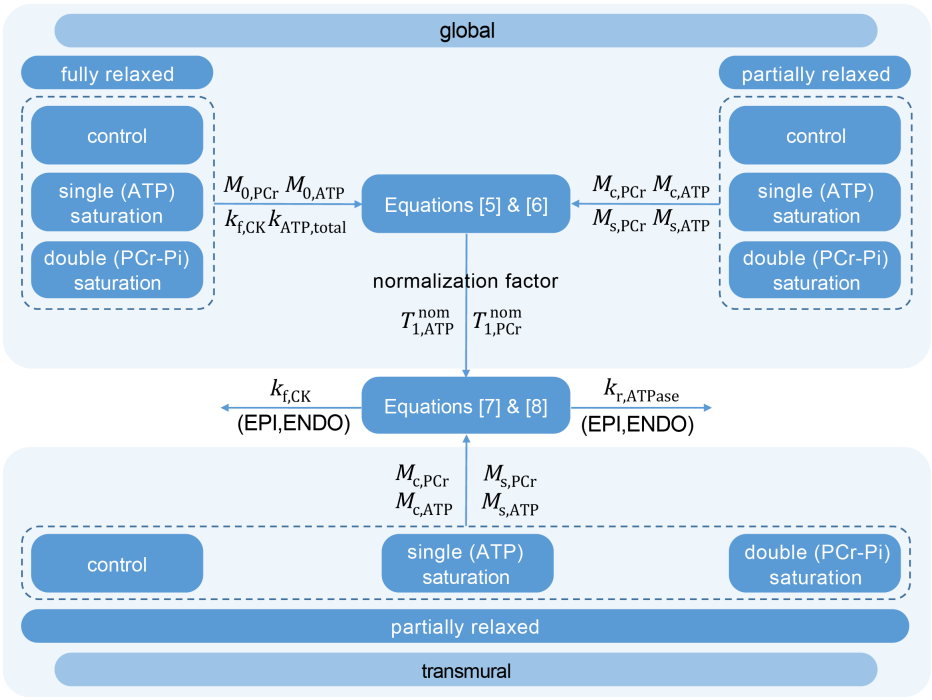

Figure 3.3: Flow chart of applying T_1^{nom} method to extract transmural rate constants. Fully relaxed global magnetization-saturation-transfer experiments (top left) are performed in the absence of saturation, with ATP saturation, and with both PCr and Pi simultaneous saturation, yielding global rate constants $k_{\mathrm{f,CK}}$ and $k_{\mathrm{ATP,total}}$. Partially relaxed global spectra (top right), control, single-, and double-saturation, yield global $M_{\mathrm{c,PCr}}/M_{\mathrm{c,ATP}}$, $M_{\mathrm{s,PCr}}$, and $M_{\mathrm{s,ATP}}$ in partially relaxed states, respectively. These global measurements are combined to calculate T_1^{nom} for both PCr and ATP using Eqs. (3.5) and (3.6). The obtained T_1^{nom} values and the normalization factor are then incorporated with the measurements obtained from the 3 partially relaxed transmural spectra (bottom) to calculate $k_{\mathrm{f,CK}}$ and $k_{\mathrm{r,ATPase}}$ using Eqs. (3.7) and (3.8) for each transmural layer.

determined in a previous report) [12, 77], and the PCr concentration required to calculate the CK flux rate ($flux_{\mathrm{f,CK}} = [\mathrm{PCr}]k_{\mathrm{f,CK}}$) was extracted based on the ratio between the magnitudes of the PCr and ATP resonances from the control spectrum of each transmural layer.

Data are presented as mean ± standard deviation (SD) and were evaluated for significance using student t-test (unpaired, 2 tailed); the Bonferroni correction was used when more than two groups were being compared. A P-value less than 0.05 was considered significant.

3.4 Results

Hemodynamic Data

Hemodynamic data during each experimental condition are summarized in Table 3.1. During high cardiac workload condition, the heart rate (HR), LV systolic pressure (LVSP), and rate pressure product (RPP) were significantly increased in response to catecholamine stimulation. Application of dopamine and dobutamine stimulation increased rate pressure product (mmHg/min) by 260% compared with baseline conditions ($P < 0.05$; Table 3.1).

Validity of Applying T_1^{nom} Method to PCr-Pi Double Saturation

Numerical simulations were carried out to confirm partially relaxed steady-state magnetization without and with PCr-Pi double saturation (Figs. 3.2a, 3.2b). For the given parameters, all three spins (PCr, ATP, and Pi) attained partially relaxed steady-state after 1 repetition cycle for both no saturation (Fig. 3.2a) and double saturation (Fig. 3.2b). Based on this, the $k_{\mathrm{ATP,total}}$ vs. ATP $M_{\mathrm{c}}/M_{\mathrm{s}}$ ratio was simulated for various flip angles (Fig. 3.2c) and repetition times (Fig. 3.2d). Depending on FA and TR, the slope, T_1^{nom}, varies while the linear relationship between $M_{\mathrm{c}}/M_{\mathrm{s}}$ and $k_{\mathrm{ATP,total}}$ is maintained. This corroborates that in addition to T_1^{nom} being a function of spin system parameters (T_1^{int} and relative ratio of metabolites), it is also a function of acquisition parameters (TR and

Hemodynamic Data during Each Experimental Condition[1]

	HR	LVSP	RRP (mmHg/	AV diff	MVO_2 (ml·O_2/min/100 gram)	
	(beats/min)	(mmHg)	min×1000)	(ml/dl)	EPI	ENDO
Baseline	96.1 ± 4.93	90.6 ± 2.27	8.71 ± 0.48	11.1 ± 0.89	10.21 ± 0.82	10.55 ± 0.85
High Cardiac Workload	194 ± 7.50[2]	116 ± 4.55[2]	22.40 ± 0.77[2]	11.7 ± 0.87	27.57 ± 1.93[2]	28.47 ± 2.00[2]

Table 3.1: RPP (mmHg/min×1000) is calculated as the product of heart rate and LVSP. MVO_2 (ml·O_2/min/100 gram of myocardium) is calculated as the product of arteriovenous oxygen difference (AV diff) and myocardial blood flow (MBF). AV diff (ml/dl) was assumed to be same in both EPI and ENDO layers. Basal MBF of 0.92 ml/min/g in the EPI layers and 0.95 ml/min/g in the ENDO layers were taken from a previous report using the same *in vivo* model[9]. In high cardiac workload state, MBF was increased proportional to increase in RPP. n = 9 for measurements (HR/LVSP/RPP) at both baseline and high cardiac workload; n = 9 and n = 6 for AV diff/MVO_2 at baseline and high cardiac work state, respectively.

FA). Increasing TR and/or decreasing FA results in partially relaxed steady-state magnetization approaching fully relaxed steady-state, with T_1^{nom} approaching T_1^{int}.

^{31}P MR Spectroscopy

At basal conditions, there was no significant difference between subepicardium and subendocardium (Table 3.2) for both $flux_{\text{f,CK}}$ (4.4 ± 0.53 vs. 4.57 ± 0.84, μmol/g/s, EPI and ENDO, respectively) and $flux_{\text{r,ATPase}}$ (1.11 ± 0.12 vs. 1.12 ± 0.13, μmol/g/s, EPI and ENDO, respectively). Under high workload where rate pressure product increased 2.6-fold, $flux_{\text{f,CK}}$ showed no significant change in both subepi- and subendo-layers (EPI: 4.52 ± 0.47; ENDO: 3.68 ± 0.16, P = NS vs. baseline), while $flux_{\text{r,ATPase}}$ increased significantly (EPI: 2.35 ± 0.27; ENDO: 2.21 ± 0.08, each $P < 0.01$ vs. baseline).

[1] Data are presented as mean±SEM

[2] $P < 0.01$ vs. baseline

[3] Data calculated based on [ATP] = 5.3μmol/g and are presented as mean±SEM

Data Calulated[3]

	Baseline		High Cardiac Workload	
	EPI	ENDO	EPI	ENDO
PCr/ATP	2.02 ± 0.05	2.2 ± 0.05	2.21 ± 0.09	2.44 ± 0.11
$k_{\mathrm{f,CK}}$ (s^{-1})	0.40 ± 0.04	0.38 ± 0.06	0.37 ± 0.06	0.29 ± 0.01
$flux_{\mathrm{f,CK}}$ (μmol/g/s)	4.4 ± 0.53	4.57 ± 0.84	4.52 ± 0.47	3.68 ± 0.16
$k_{\mathrm{r,ATPase}}$ (s^{-1})	0.21 ± 0.02	0.21 ± 0.02	0.44 ± 0.05^2	0.42 ± 0.02^2
$flux_{\mathrm{r,ATPase}}$ (μmol/g/s)	1.11 ± 0.12	1.12 ± 0.13	2.35 ± 0.27^2	2.21 ± 0.08^2

Table 3.2: PCr/ATP ratios (n = 8 for baseline and n = 7 for HWL) were obtained using partially relaxed spectra that were normalized back to its fully relaxed equivalent state as described in the methods section. n = 6 for baseline flux rates and n = 5 for high cardiac workstate flux rates. EPI, subepicardial; ENDO, subendocardial.

3.5 Discussion

MVO_2 Calculation

In the present study, myocardial oxygen consumption (MVO_2) was calculated by taking the arteriovenous oxygen difference and multiplying it by the rate of myocardial blood flow (MBF) taken from our previous report using the identical porcine open chest model and radioactive microspheres [9]. Blood samples were drawn from the aortic and coronary vein catheters into heparin-filled syringes during both surgical preparation and MR imaging. PO_2 and pH were measured using a calibrated blood gas analyzer (RAPIDLab 248, Siemens Healthcare, Erlangen Germany). Because RPP (heart rate $\times$ LVSP) is linear with respect to MVO_2 [78], under high workload conditions, the MBF was scaled based on RPP increase going from baseline to high workload state. Table 3.1 summarizes the calculated myocardial oxygen consumption. Myocardial blood flow of 0.92 ml/min/g was used for the EPI layers and 0.95 ml/min/g was used for the ENDO layers. In high cardiac workload state, MBF was scaled based on increase in RPP. Based on this, going from basal to high workload condition, both RPP and MVO_2 rate are

more than doubled in both the EPI and ENDO layers.

In dogs, using FLAX-ISIS and RAPP-ISIS, we have previously reported a significant transmural gradient in the myocardial PCr to ATP ratio across LV wall of the normal heart, with slightly but significantly lower PCr/ATP in the inner layer of the LV wall [72, 9, 79]. The concept that the inner layer myocardium of LV is more susceptible to an ischemia insult metabolically is based on the fact that the inner layer works twice as much as the outer layer [80] and myocardial blood flow ceases during systole as a result of the back pressure during the systole [81]. This concept was later demonstrated experimentally in a study where myocardial ischemia was induced by a partial coronary artery stenosis produced by a hydraulic occluder, with the coronary perfusion pressure monitored using an intracoronary pressure transducer and regional myocardial blood flow measured using microspheres [68]. In this experimental setting, the myocardial PCr/ATP ratio was measured continuously while the severity of coronary stenosis was progressively increased by tightening the hydraulic occluder.

The present study uses 1D-CSI, which uses a spatially linear gradient field to spatially encode. Compared with FLAX-ISIS and RAPP-ISIS, which uses the B_1 gradient of a surface coil to spatially encode, 1D-CSI results in a uniform spatial resolution (identical voxel size) whereas FLAX-ISIS and RAPP-ISIS results in a nonuniform spatial resolution due to the B_1 gradient being spatially nonlinear. The present data indicates that in the normal porcine heart at baseline, there is no significant transmural gradient across the LV wall in terms of PCr/ATP, CK forward flux rate, and ATP hydrolysis rate (Table 3.2). The reason for the discrepancy between the present study and previous reports that used canine models [68, 12, 78] remain unclear. It could simply be due to the small size of the study group, or the difference in species between the porcine and canine hearts.

ATP Turnover Rates in the Subepicardial and Subendocardial Layers of the LV Wall

Spectra were generated for the epicardial and endocardial layers of the LV wall

in the absence of saturation, with ATP saturated, and with both PCr and Pi saturated (Fig. 3.4); notably, the resonance for 2,3-DPG was considerably more prominent in endocardial spectra than in epicardial spectra, which can be explained by the presence of blood in the LV chamber. Please note that all spectra shown were obtained from short TR and represent partially relaxed states. In both LV layers, the PCr peak was lower in the ATP-saturated spectrum than in the unsaturated spectrum, while the ATP peak declined in response to simultaneous PCr and Pi saturation. The ATP hydrolysis rate ($flux_{\mathrm{r,ATPase}} = [\mathrm{ATP}]k_{\mathrm{r,ATPase}}$) and CK flux rate ($flux_{\mathrm{f,CK}} = [\mathrm{PCr}]k_{\mathrm{f,CK}}$) was extracted as described in the methods section. Significant differences were not observed between the epicardial and endocardial layers for either flux rate, and $flux_{\mathrm{f,CK}}$ did not change significantly when the cardiac workload was increased (Table 3.2). However, $flux_{\mathrm{r,ATPase}}$ in both regions was significantly greater during periods of high cardiac workload in comparison with baseline condition, which is consistent with the concept that ATP consumption increases when RPP increases.

3.6 Conclusions

A novel method in measuring myocardial ATP hydrolysis rates with transmural differentiation in the *in vivo* heart has been demonstrated. The findings in the present study indicate that there are no significant differences between EPI vs. ENDO concerning the ATP hydrolysis rate or CK flux rate, in both baseline and high cardiac works states of normal porcine model. The change of the basal to high cardiac work states is accompanied by a linear increase of ATP hydrolysis rate with no changes in CK flux rate.

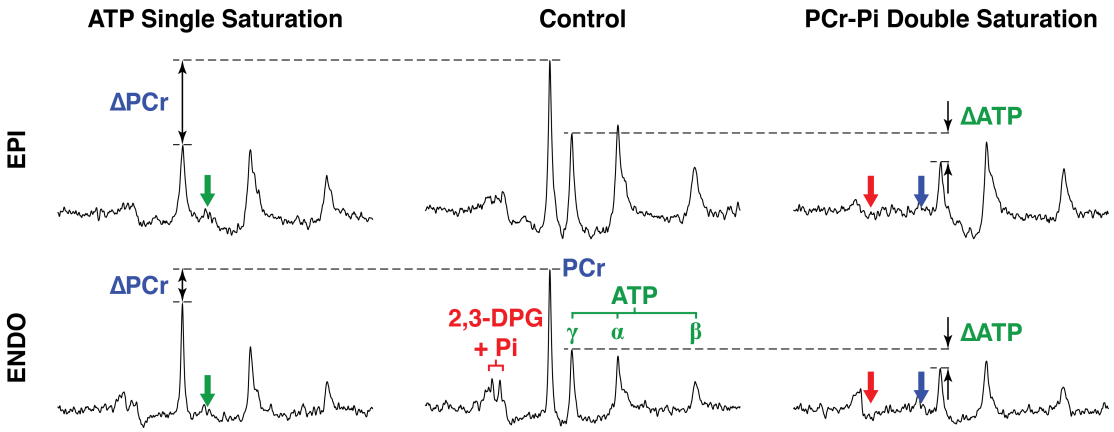

Figure 3.4: ^{31}P MRS-MST assessments of myocardial ATP turnover rates from partially relaxed spectra. Spectra were generated for the epicardial (EPI) and endocardial (ENDO) layers of the LV wall with ATP saturated (green arrows), in the absence of saturation, and with both PCr (blue arrows) and Pi (red arrows) saturated. The Fourier-series window profile produced minimal (<3%) overlap between neighboring voxels. Changes in the intensities (black double arrows) of the resonances for PCr in the ATP-saturated spectra and for ATP in the PCr/Pi double-saturated spectra were used to calculate the fluxes of the PCr→ATP and ATP→Pi reactions. Note, it is the difference in relative amount (spectra integral), not spectra height, which is used to extract ΔPCr and calculate rates.

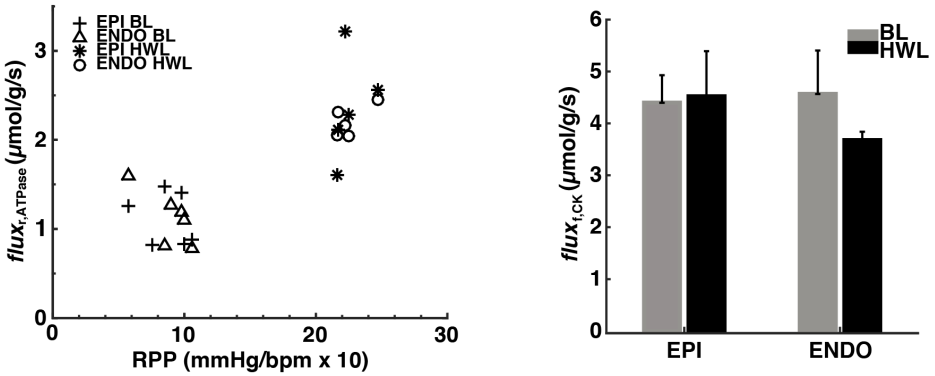

(a) **(b)**

Figure 3.5: Correlation of flux rates with baseline and high work states of normal porcine hearts. **a**: Hydrolysis flux rate ($flux_{\mathrm{r,ATPase}}$) vs. rate pressure product (RPP) under baseline and high cardiac work states show that an increase in cardiac workload is accompanied by an increase in ATP hydrolysis rate for both EPI and ENDO layers. There was no significant difference between EPI versus ENDO for $flux_{\mathrm{r,ATPase}}$ and CK flux rate ($flux_{\mathrm{f,CK}}$) (**b**) in both baseline and high cardiac work states.

Chapter 4

2D Pulses Using Spatially Dependent Frequency Sweeping

This is a manuscript accepted for publication in Magnetic Resonance in Medicine.

4.1 Introduction

By evenly distributing radiofrequency (RF) power in time, frequency-modulated (FM) pulses can provide certain advantages in MRI, such as high tolerance to B_1 inhomogeneity, sharp slice profiles, and broadband excitation with low peak RF power[14, 15]. When an FM pulse is used to excite (or invert) spins in a slice, the isochromats experience unique excitation (or inversion) times and the phase of the resultant transverse magnetization varies nonlinearly in the direction of the gradient. With chirp and hyperbolic secant (HS1) pulses, a spatially quadratic phase is produced, and inverting the gradient polarity after applying these FM pulses causes the magnetization to rephase at different times[82, 83].

In recent years, the ability to sequentially excite the different isochromats with one-dimensional (1D) FM pulses has been exploited to encode spatial information along one or two dimensions of an image. Pipe introduced quadratic encoding, which stems from the sequential chirp excitation previously mentioned, to encode

along the slice-selective direction[82]. Shrot et al showed how frequency encoding in conventional two-dimensional (2D) MRI can be replaced with the spatiotemporal encoding provided by a chirp pulse[84]. Chamberlain et al substituted phase encoding with spatiotemporal encoding to create a series of echoes with constant echo time to avoid blurring caused by T_2^* relaxation[85].

Recently, 2D FM pulses have gained attention due to their ability to temporally encode in two dimensions. Through simulations, Dumez and Frydman demonstrated RF pulses that sequentially "sculpt" along 2D raster and spiral spatial trajectories[86]. Snyder et al introduced the concept of MRI by steering localized resonance through an object using 2D FM pulses to spatiotemporally encode along single-turn spiral trajectories[87]. By using a B_1^+ profile map and adjusting the pulse pattern in a temporal manner based on the resonance trajectory, the feasibility of B_1 inhomogeneity compensation was shown through simulations. MR imaging with tolerance to inhomogeneous fields is a unique attribute of multidimensional FM pulses.

Here, we present a new class of 2D FM pulses that produces maximum phase coherence in a spatiotemporal manner along a spiral trajectory in space. By rewinding the gradients after applying the pulse, this phase coherence trajectory can be reversed. In this manner, the spatiotemporal dependence for image acquisition is preserved. Furthermore, these 2D FM pulses offer a means to compensate for inhomogeneity within the selectively excited volume. This extends the work of Snyder et al by replacing the need for multiple spiral trajectories to completely cover the object with a single shot. Based on a k-space description, we provide the theoretical basis for designing such pulses and describe how coherence can be steered along a trajectory in a sequential manner. Bloch simulations and experimental images of phantoms and human brain are used for validation.

4.2 Theory

4.2.1 Spatiotemporal Coherence Pulse Design

In the presence of a constant gradient, a 1D FM pulse, such as a chirp and hyperbolic secant (HS1) pulse[36], rotates isochromats having resonant frequencies within the excitation bandwidth onto the transverse plane in a sequential manner. Accordingly, the transverse magnetization $M_{\mathrm{xy}}(\vec{r})$ is encoded with a spatially varying quadratic phase (in addition to a linear phase) in the direction of the gradient[82, 83]. From a k-space analysis, while traversing a uniformly sampled k-space in one dimension, the chirp and HS1 pulse distributes a quadratic phase equivalent to the pulse phase, in addition to modulating the k amplitude through the B_1 amplitude. Thus, the phase distribution in physical space and k-space are both quadratic. This can be extended to a higher order dimension by exploiting symmetry and carefully allocating phase while sampling k-space in such a way that it replicates the k-space of the 1D FM pulses along the symmetric direction.

The phase of a chirp pulse is proportional to τ^2, where $\tau(=\frac{t}{T_{\mathrm{p}}})$ is normalized time with respect to the pulse length T_{p}. In the case of a constant gradient of magnitude G applied in concert with the pulse to achieve slice selection, the RF phase ends up being proportional to $k^2(\tau)$ because the 1D k-space of the pulse is directly proportional to $k(\tau) = \gamma G T_{\mathrm{p}} \tau$. This can be expanded to two dimensions by sampling a spiral k-trajectory of constant gradient magnitude in two dimensions. By taking advantage of the trajectorys radial symmetry, one can allocate phase that is proportional to the square of the radial magnitude of k, thereby making it equivalent to the 1D chirp when projecting along the radial direction. Figure 4.1 depicts the radially sampled k-space amplitude and phase of a 2D chirp pulse that selectively excites a cylindrical volume. With a constant RF amplitude ($\omega_1^{\mathrm{chirp}}$) with respect to time, the resulting FM function ($\omega_{\mathrm{RF}}^{\mathrm{chirp}}(t)$) of a parabolic phase profile in 2D k-space and the gradient function $\vec{G}_{\mathrm{s}}(t)$ in polar

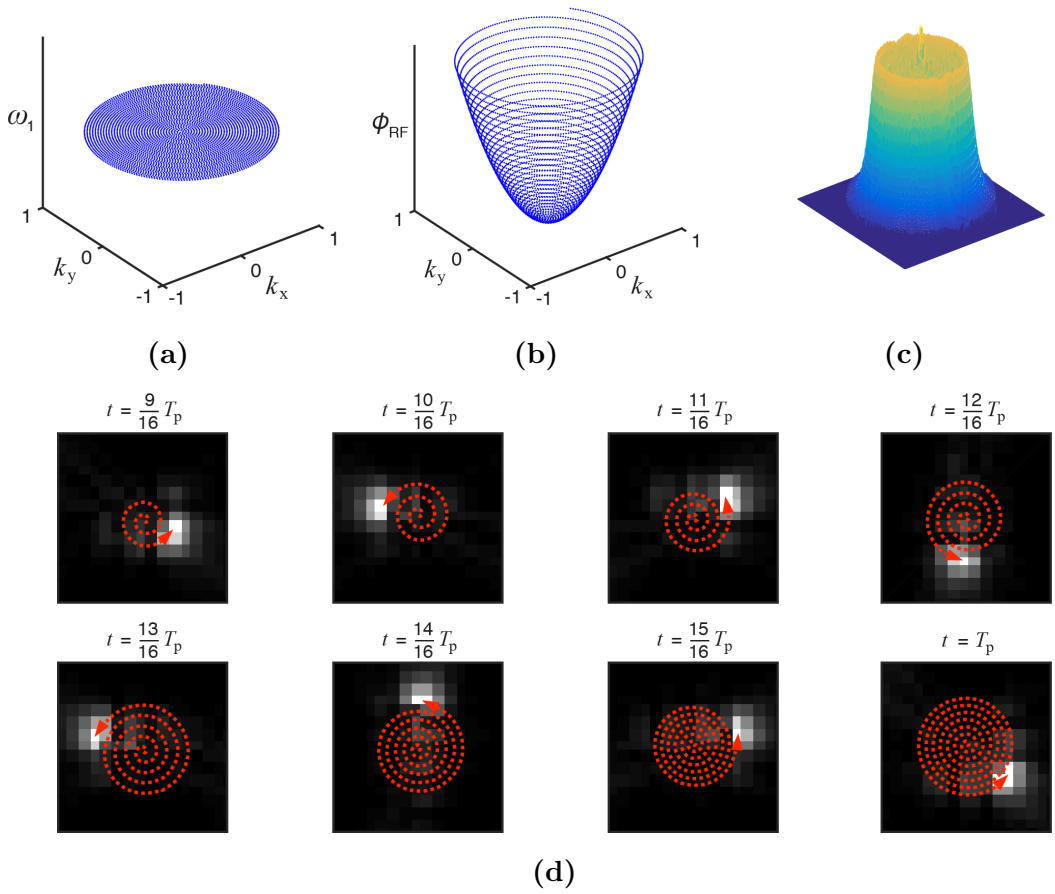

Figure 4.1: A k-space representation of the 2D chirp pulse is shown in terms of its RF amplitude (ω_1) (**a**) and phase (ϕ_{RF}) functions (**b**). **c**: This mesh plot of the resulting excitation profile produced by the 2D chirp pulse shows selective disc excitation in 2D space (equivalent to cylindrical excitation in 3D space). **d**: Snapshots in time during the second half of 2D chirp pulse allow visualization of the spatiotemporal phase coherence as it moves along the outward spiraling trajectory.

coordinates are

$$\omega_{\mathrm{RF}}^{\mathrm{chirp}}(t) = \omega_{\mathrm{c}} + A\sqrt{|\vec{k}_{\mathrm{s}}(t)|^2}\frac{d|\vec{k}_{\mathrm{s}}(t)|}{dt} \tag{4.1}$$

$$\vec{G}_{\mathrm{s}}(t) = \frac{1}{\gamma}\frac{d\vec{k}_{\mathrm{s}}(t)}{dt} = G(t)\exp(i\theta_{\mathrm{G}}(t)) \tag{4.2}$$

where ω_{c} is the carrier frequency, A is a scaling factor, and γ is the gyromagnetic ratio. For an outwardly traversing spiral having N turns, the corresponding k-vector function $\vec{k}_{\mathrm{s}}(t)$, k-angular function $\theta_{\mathrm{k}}(t)$, gradient amplitude function $G(t)$, and gradient phase function $\theta_{\mathrm{G}}(t)$ are given respectively by

$$\vec{k}_{\mathrm{s}}(t) = k_{\max}\sqrt{\tau}\exp(i\theta_{\mathrm{k}}(t)), \quad \theta_{\mathrm{k}}(t) = 2\pi N\sqrt{\tau} \tag{4.3}$$

$$G(t) = \frac{k_{\max}}{\gamma T_{\mathrm{p}}}\sqrt{\frac{1}{4\tau} + \pi^2 N^2}, \quad \theta_{\mathrm{G}}(t) = \theta_{\mathrm{k}}(t) + \tan^{-1} 2\pi N\sqrt{\tau} \tag{4.4}$$

To avoid the singularity in the gradient amplitude function (Eq. (3.4)), implementation of $\vec{G}_{\mathrm{s}}(t)$ is performed by discretizing Eq. (4.3) and taking its derivative. Because the allocated phase is radially symmetric in k-space, the 2D chirp pulse produces local phase coherence along an outward spiraling trajectory in a manner that is analogous to the 1D chirp pulse in which excitation sequentially occurs along the quadratic phase. Alternatively, by replacing τ with $1 - \tau$, spiral k-space is sampled in a radially inward order and inward spiraling of local phase coherence is produced by the pulse. The reason why local phase coherence (as opposed to localized excitation) happens in a spatiotemporal manner is explained further below. However, an intuitive understanding into why the sequential excitation model does not apply can be obtained by considering the rotating slice illustration used previously[87]. Specifically, when the slice undergoes multiple 2π rotations on a spiral trajectory, the magnetization at a given location experiences the on- or near-resonance condition multiple times during the pulse. Hence, instead of tipping magnetization in a sequential manner along the trajectory, the

magnetization is affected by the pulse multiple times, and the number of times is dictated by the number of turns on the spiral.

To give better insight as to how phase coherence is steered through physical space, k-space analysis is used. By assuming a low tip angle excitation which decouples the transverse magnetization from the longitudinal magnetization[35], $M_{\mathrm{xy}}(\vec{r})$ in the rotating frame for a pulse with amplitude-modulated function $\omega_1(t)$ and FM function $\omega_{\mathrm{RF}}(t)$ can be written as[37]

$$M_{\mathrm{xy}}(\vec{r}) = iM_0 \exp(-i\varphi(T_{\mathrm{p}})) \int_0^{T_{\mathrm{p}}} \omega_1(t) \exp(-i\vec{r} \cdot \vec{k}_{\mathrm{r}}(t))dt \tag{4.5}$$

$$\vec{k}_{\mathrm{r}}(t) = -\gamma \int_t^{T_{\mathrm{p}}} \left[\vec{G}(t') - \frac{(\omega_{\mathrm{RF}}(t') - \omega_{\mathrm{c}})}{\gamma} \frac{\hat{r}}{|\vec{r}|} \right] dt' \tag{4.6}$$

where M_0 is the initial longitudinal magnetization, $\varphi(T_{\mathrm{p}}) = \int_0^{T_{\mathrm{p}}} (\omega_{\mathrm{RF}}(t') - \omega_{\mathrm{c}})dt'$, and $\hat{r} = \frac{\vec{r}}{|\vec{r}|}$ is a unit vector. A detailed derivation of the equations above has been provided previously[37].

During the pulse, isochromats are continuously being excited, de-phased, and re-phased due to the gradient and frequency being continuously modulated. Magnetization refocuses at a given location $\vec{r}$ when the position-dependent k-space equals 0 $\left(\vec{k}_{\mathrm{r}}(t) = 0\right)$, analogous to echoes forming when $k = 0$ in Fourier imaging. Mathematically, localization of coherence at time $0 \leq t \leq T_{\mathrm{p}}$ occurs at the spatial location where the condition

$$\gamma \vec{G}(t) \cdot \vec{r} = \omega_{\mathrm{RF}}(t) - \omega_{\mathrm{c}} \tag{4.7}$$

is satisfied. When this condition is met, the position-dependent k-space given by Eq. (4.6) becomes zero, the nullification of the phase term in Eq. (4.5) follows, and localized maximum phase coherence occurs at this position. It is important to note that this approach of attaining spatiotemporal coherence is different from previous implementations. Specifically, instead of using Eq. (4.7) in real-space to ensure the excitation trajectory covers the whole object of interest, the distribution of phase or frequency modulation in k-space is used to design the pulse. Only after

completing this step is the coherence trajectory extracted using Eq. (4.7). For the 2D chirp pulse, this procedure yields an RF pulse consisting of a constant frequency with the actual frequency sweep being achieved through frequency-modulated cosinusoidal gradients. From Eqs. (4.1), (4.2), and (4.7), the maximum coherence trajectory $\vec{r}_{\mathrm{o}}^{\,\mathrm{chirp}}(t)$ is given by

$$\vec{r}_{\mathrm{o}}^{\,\mathrm{chirp}}(t) = A\sqrt{|\vec{k}_{\mathrm{s}}(t)|^2}\exp(-i\theta_{\mathrm{G}}(t)) \tag{4.8}$$

According to Eqs. (4.1) and (4.8), the scaling factor A has units of $\mathrm{cm}^2/\mathrm{rad}$ and the maximum excitation radius is given by $Ak_{\max}$.

To shift the selected excitation region by $\vec{r}_{\mathrm{o}}$, a constant offset $\vec{k}_{\mathrm{s}}^{\mathrm{o}}$ is applied to the sampled k-space trajectory. By using the relationship given in Eq. (4.7), one can extract the offset $\vec{k}_{\mathrm{s}}^{\mathrm{o}}$ needed to produce a shift of $\vec{r}_{\mathrm{o}}$. For the 2D chirp pulse, the relationship between offset $\vec{k}_{\mathrm{s}}^{\mathrm{o}}$ and shift $\vec{r}_{\mathrm{o}}$ is given by

$$\vec{r}_{\mathrm{o}} = A\vec{k}_{\mathrm{s}}^{\mathrm{o}} \tag{4.9}$$

4.2.2 2D Hyperbolic Secant Spatiotemporal Pulse

Due to the nonideal ripple excitation profile produced by the 2D chirp pulse, a 2D version of the original HS1 pulse[36] was also developed for the purpose of achieving a flatter excitation profile. As shown in Figure 4.2, for the same k-trajectory, the amplitude was modulated proportional to $\mathrm{sech}(\beta|\vec{\kappa}_{\mathrm{s}}(t)|)$ and the phase was allocated proportional to $\ln(\cosh(\beta|\vec{\kappa}_{\mathrm{s}}(t)|))$,

$$\omega_1^{\mathrm{HS1}}(t) = \omega_1^{\max}\mathrm{sech}(\beta|\vec{\kappa}_{\mathrm{s}}(t)|) \tag{4.10}$$

$$\omega_{\mathrm{RF}}^{\mathrm{HS1}}(t) = \omega_{\mathrm{c}} + B\beta\tanh(\beta|\vec{\kappa}_{\mathrm{s}}(t)|)\frac{d|\vec{\kappa}_{\mathrm{s}}(t)|}{dt} \tag{4.11}$$

where β is a dimensionless truncation factor, $\vec{\kappa}_{\mathrm{s}}(t) = \vec{k}_{\mathrm{s}}(t)/\max(|\vec{k}_{\mathrm{s}}(t)|)$ is $\vec{k}_{\mathrm{s}}$ normalized to 1, $\omega_1^{\max}$ is the maximum RF amplitude, B is a scaling factor in units of radian, and $B\beta/k_{\max}$ is the maximum excitation radius.

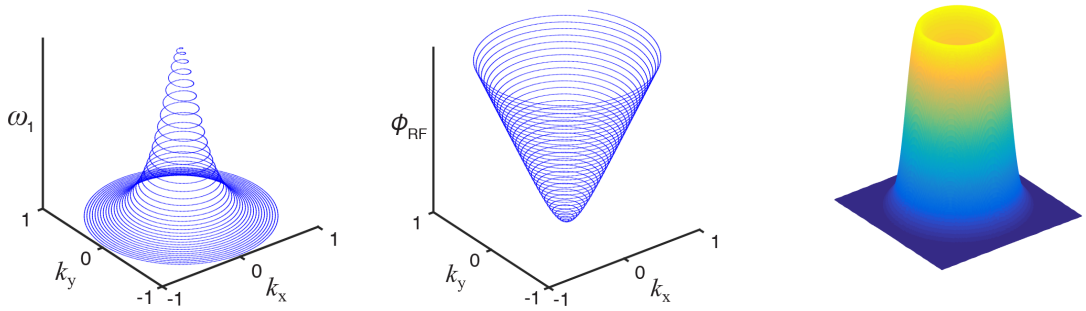

(a) **(b)** **(c)**

Figure 4.2: A k-space representation of the 2D hyperbolic secant (HS1) pulse is shown in terms of its RF amplitude (ω_1) (**a**) and phase (ϕ_{RF}) functions (**b**). **c**: This mesh plot of the resulting excitation profile produced by the 2D HS1 shows no ripples, unlike those of the 2D chirp pulse.

4.2.3 B_1 Compensation

As stated above, one of the most promising aspects of multidimensional FM excitation is the ability to compensate for field inhomogeneity. By distributing phase in 2D k-space, and thus keeping coherence spatially confined, the flip angle variation that normally results from B_1 inhomogeneity can be avoided. Specifically, by linking a spatial B_1^+ map, $B_1^+(\vec{r})$, with the maximum coherence trajectory, $\vec{r}_{\mathrm{o}}(t)$, one can compensate for B_1^+ inhomogeneity by modifying the amplitude function of the pulse according to

$$\omega_1^{B_{1\mathrm{comp}}}(t) = \omega_1(t)/\gamma B_1^+(\vec{r}_{\mathrm{o}}(t)) \tag{4.12}$$

The reasoning behind this approach assumes that maximum RF energy is deposited along the trajectory of maximum coherence during the pulse. Therefore, if at this location, the B_1^+ produced by the coil is less/more than expected, one can modify the pulse amplitude function by scaling the RF voltage at that time point based on the measured B_1^+ map. By another interpretation, the k-space amplitude profile of the 2D FM pulse is deformed by a spatial variation of B_1, and a rescaling of the B_1 amplitude is thus needed to retrieve the desired flat

excitation profile. This assumption has been validated through simulations and experiments.

4.2.4 Imaging Sequences

The 2D FM pulses described herein excite a cylindrical volume because they are sampled on a spiral k-space trajectory. As with 1D FM pulses, the quadratic phase of the excited M_{xy} does not result in signal loss in conventional Fourier imaging, provided the spatial scale of each pixel is small compared with the spatial scale of the phase variation[83]. Thus, a conventional 2D spin-echo sequence, which included standard frequency- and phase-encoding gradients and slice-selective π-pulse(s) for refocusing, was used to acquire axial images of the cylinder excited by the 2D FM pulses. In addition, an implementation of the spin-echo sequence with spiral readout was used for single-shot imaging. The latter takes advantage of the fact that after spiral-in excitation, whereby k-space is centered, sampling while rewinding the gradients defines a k-space trajectory spiraling outward. At the same time, phase coherence is rewound on the trajectory that is opposite the one traversed during excitation. As in the 1D case, a quadratic phase profile is created along the trajectory of maximum coherence. When an odd number of π-pulse(s) are used for refocusing, time reversed readout gradients are required and the isochromats experience different echo times (TE); i.e., isochromats that experience phase coherence first re-cohere last and isochromats that experience phase coherence last re-cohere first. When using an even number of π-pulses, time reversal of the readout gradient is no longer required and all isochromats experience the same TE, i.e., isochromats that experience phase coherence first re-cohere first and isochromats that experience phase coherence last re-cohere last. These sequences are shown in Figure 4.3.

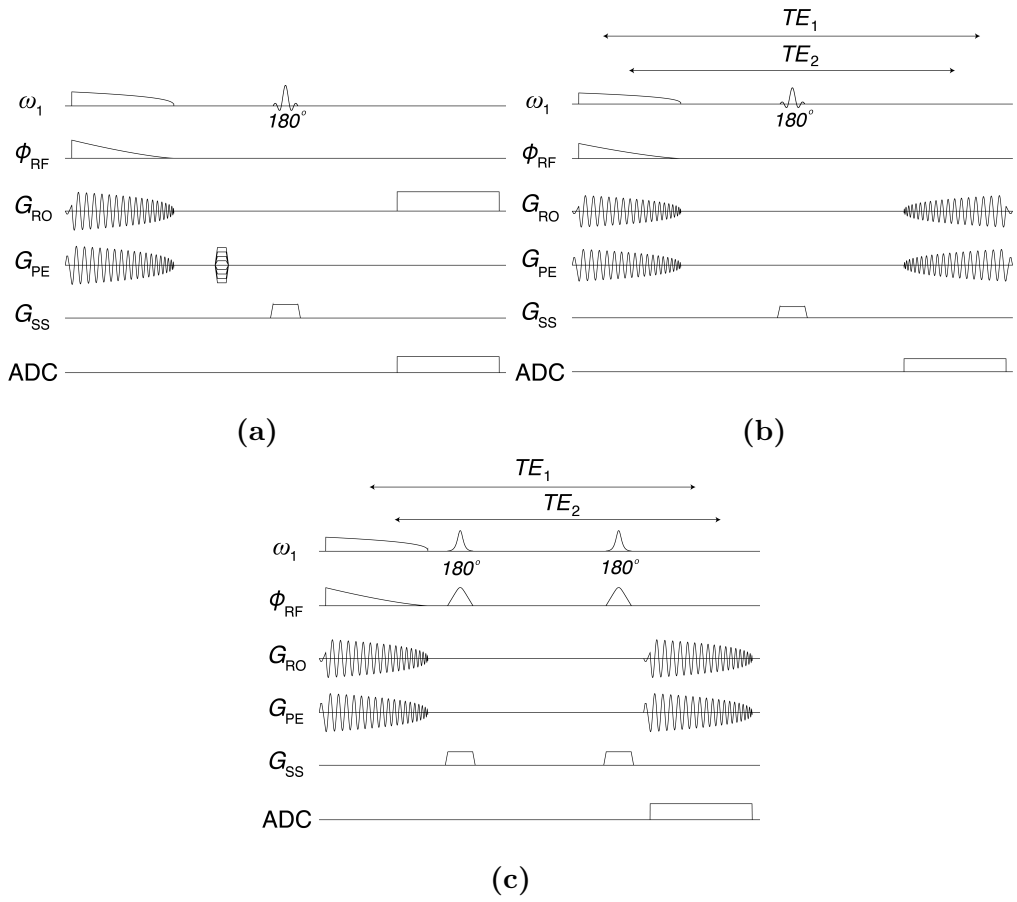

Figure 4.3: Pulse sequences used to evaluate the performance of 2D FM pulses. **a**: Conventional single-slice spin-echo sequence with slice selection along the longitudinal axis of the cylindrical volume excited by the 2D pulses. **b**: A version of this sequence with spiral readout. Isochromats that experience phase coherence first during excitation will "re-cohere" last during readout. **c**: With a double spin-echo version of the sequence, a constant echo time between excitation and readout phase coherences is possible.

4.3 Methods

4.3.1 Simulations

MATLAB (MathWorks, Inc., Natick, MA) and a Bloch simulator programmed in C language were used to test and validate the spatiotemporal excitation principles introduced above. The 2D simulations were carried out to evaluate the resulting pulse excitation profiles assuming a spatially homogenous spin distribution. To demonstrate the occurrence of sequential, localized coherence during excitation, voxel averaging of the individual transverse magnetization components M_{x} and M_{y} were done independently using 10×10 isochromats per voxel. Images were constructed from a 41×41 voxel averaged matrix. Potential relaxation effects were not considered in the simulations.

For B_1 compensation, a B_1^+ field map was generated for a 14.4 cm diameter loop coil using the Biot-Savart equation and imposed on simulations. The pulse amplitude modulation function, $B_1(t)$, was rescaled based on the B_1^+ inhomogeneity along the trajectory of coherence. B_1 compensation was demonstrated on a uniform circular phantom.

A preliminary attempt to compensate for spatial B_0-variation was also conducted. B_0 compensation can be realized by modifying the RF pulse phase. In the case of a spatially varying static field, the carrier frequency in Eqs. (4.6) and (4.7) becomes spatially dependent. This consequential position-dependent phase can be compensated through the RF phase if the position dependent static field profile is known. For demonstration, an attempt to compensate a saddle-shaped static field (i.e., B_0 proportional to $x^2 - y^2$) was made by subtracting a phase proportional to $\sqrt{k_{\mathrm{x}}^2(t) - k_{\mathrm{y}}^2(t)}$ from the parent pulse phase, which is proportional to $\sqrt{k_{\mathrm{x}}^2(t) + k_{\mathrm{y}}^2(t)}$. The resulting excitation profile was then compared with the noncompensated profile.

4.3.2 Experiments

Experimental verification was performed on a Varian DirectDrive^{TM} console (Agilent Technologies, Santa Clara, CA) interfaced to a 90 cm 4 Tesla (T) magnet (Oxford Magnet Technology, Oxfordshire, UK) with a clinical gradient system (model SC72, Siemens, Erlangen, Germany). The 2D spatiotemporal excitation pulses were tested and optimized on a cylindrical phantom consisting of distilled water doped with 1.5% agar and 0.1 mM Gd ($T_1 \sim 1$ s and $T_2 \sim 160$ ms). A spiral k-space trajectory was resampled to accommodate gradient slew rate constraints while maintaining the equivalent k-profile, as shown in Figure 4.4. Specifically, the k-space was sampled at different points along the identical spiral trajectory to meet slew rate constraints, resulting in modified gradient tables well within the slew-rate limit. The phase of the RF pulse was modified based on this newly sampled spiral k-space trajectory, while the RF amplitude weighting was density corrected accordingly. In consideration of the known sensitivity of spiral trajectories to gradient performance, the gradients in each direction were measured[88] and calibrated assuming no cross correlation. The RF pulse was further modified based on these measurements to ensure high fidelity. Demonstrations of selective excitation and chemical-shift effects were performed using two different sequences: (i) 2D excitation followed by phase- and frequency-encoded multishot spin-echo imaging (Fig. 4.3a), and (ii) 2D excitation followed by spin-echo imaging using spiral-readout single-shot imaging (Fig. 4.3b). A 16-element transverse electromagnetic (TEM) head coil[89] was used for these experiments.

To demonstrate B_1-compensation, a double-loop quadrature surface coil (loop diameters = 8 cm) was used. The B_1^+ map was obtained using the actual flip-angle sequence[90], whereas the B_1^- map was obtained using a double spin-echo sequence, in which an adiabatic half passage (AHP) pulse was used for excitation followed by two adiabatic full passage (AFP) pulses for slice-selective refocusing and quadratic phase compensation. Sufficient transmit power was delivered to both pulses to ensure operation in the adiabatic regime. This ensured that all isochromats went through equal rotation, thus resulting in an image reflecting

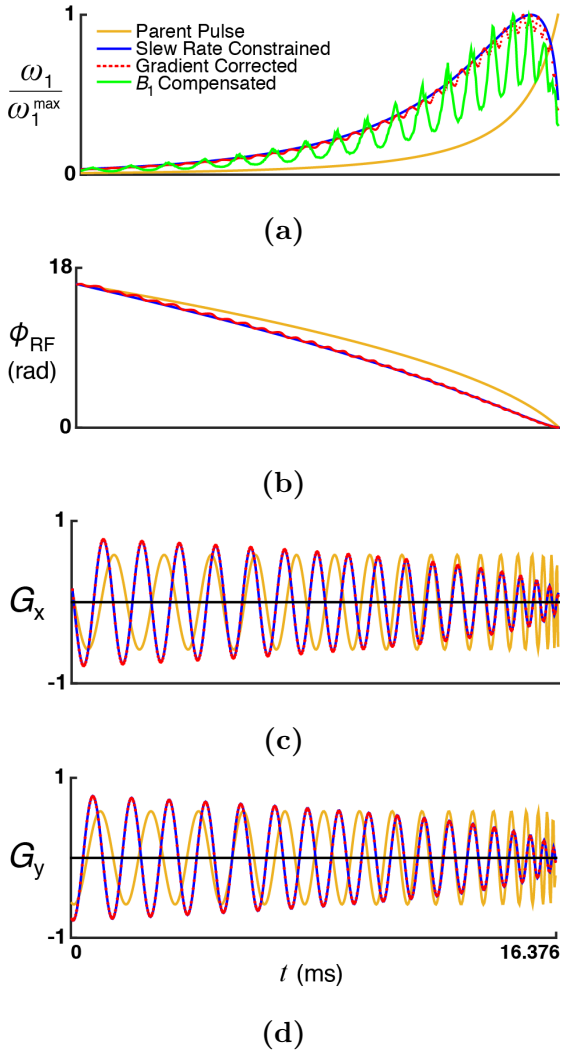

Figure 4.4: Plots showing the modulation functions of the 2D HS1 pulse. RF amplitude (**a**), RF phase (**b**), x-axis gradients (**c**), and y-axis gradients (**d**) for uniformly sampled (beige), slew-rate adjusted (blue), gradient measured (red dot), and B_1 compensated (green) versions of the pulse.

only the B_1^- profile. B_1^+ compensated and noncompensated images were obtained with the double spin-echo sequence using AFP pulses for slice-selective refocusing and same peak B_1 power. The use of two AFP pulses in the adiabatic regime ensured uniform inversion in the presence of surface coil B_1^+ inhomogeneity and compensated the subsequently induced quadratic phase along the slice direction. The images were then normalized with respect to the B_1^- map to remove the receive sensitivity, resulting in images reflecting only transmit B_1^+ spatial variation.

Further experiments were carried out to examine how the excitation profile changes in the presence of a highly inhomogeneous B_0. To produce an inhomogeneous field, the x^2-y^2 shim current was driven to its limit. Images were then acquired using the multishot spin-echo sequence (Fig. 4.3a). To minimize spatial shift caused by inhomogeneous B_0 during frequency encoding, the bandwidth of the readout was maximized, which resulted in a maximum voxel shift of only half of one voxel. These results were then compared with the profile of an amplitude-modulated 2D jinc pulse[91], which is a pulse weighted by a jinc function in 2D k-space, thus producing a cylindrical excitation profile similar to the 2D FM pulses. The number of spiral turns and excitation width was designed to be identical to the 2D FM pulses. B_0 maps were acquired using two gradient echo images of different echo times, TE_1 and TE_2 ($TE_1 < TE_2$), and dividing their phase difference map by $TE_2 - TE_1$.

4.4 Results

4.4.1 Simulations

Results from Bloch simulations of a 2D chirp pulse at different time points during the second half of the pulse are shown in Figure 4.1d. As depicted by the bright spots, the coherence is steered along a spiral trajectory. The mesh plots in Figures 4.1c and 4.2c depict the simulated excitation profiles of the 2D chirp and 2D HS1 pulses, respectively.

The uniformity of the flip angle produced by the 2D chirp and 2D HS1 pulses can be best visualized in the images of Figure 4.5. The radially varying flip angle seen in the simulated excitation profile of the 2D chirp pulse (Fig. 4.5b) is a known undesirable characteristic of chirp pulses, while the profile of the simulated 2D HS1 pulse (Fig. 4.5f) exhibits a flatter flip angle profile, similar in shape to that produced by an equivalent 1D HS1 pulse.

Because the frequencies of both pulse and gradient functions are modulated, the bandwidth of the 2D spiral trajectory pulse cannot simply be defined in the traditional sense of the total frequency swept by the RF pulse. Instead, for a pulse of a specific spiral trajectory, pulse width, and gradient amplitude, one can use the spatial displacement due to off-resonance sensitivity $\Delta x = \Delta\omega/\mathrm{BW} \cdot \mathrm{thk}$, where Δx is the spatial displacement of excitation thickness thk resulting from a pulse of bandwidth BW for an off-resonance $\Delta\omega$, to deduce the bandwidth. In the 1D case, the bandwidth of a pulse would be equivalent to the off-resonance that results in a spatial displacement equal to the excitation thickness. For the 2D FM case, because excitation width increases/decreases with off-resonance, we can define the bandwidth as the offset that doubles the excitation width. For the pulse used in the simulations and experiments (with $T_\mathrm{p} = 16.384$ ms, 18-turn spiral trajectory, and 0.787 G/cm gradient amplitude), the bandwidth using this approach was 200 Hz, resulting in a time-bandwidth product of 3.2768. The relative specific absorption rate (SAR) of the 2D HS1 for a 10° flip angle produced with the TEM coil, calculated as the time integral of $B_1^2(t)$, was 2.978 W/kg, which is substantially greater than that produced by a hard pulse (0.1746 W/kg) of equal bandwidth and flip angle. The peak value of $\gamma B_1/2\pi$ was 30 Hz for the 2D HS1 and 6.3 Hz for the 4.4 ms hard pulse. The peak B_1 for the 2D HS1 pulse was determined through Bloch simulations and was confirmed to be linear for flip angles up to 20°.

The point spread function (PSF) of the 2D FM pulses is a jinc function (polar coordinate analog of the sinc function) due to the finite spiral excitation k-trajectory being a product of an infinite spiral k-trajectory with a cylindrical

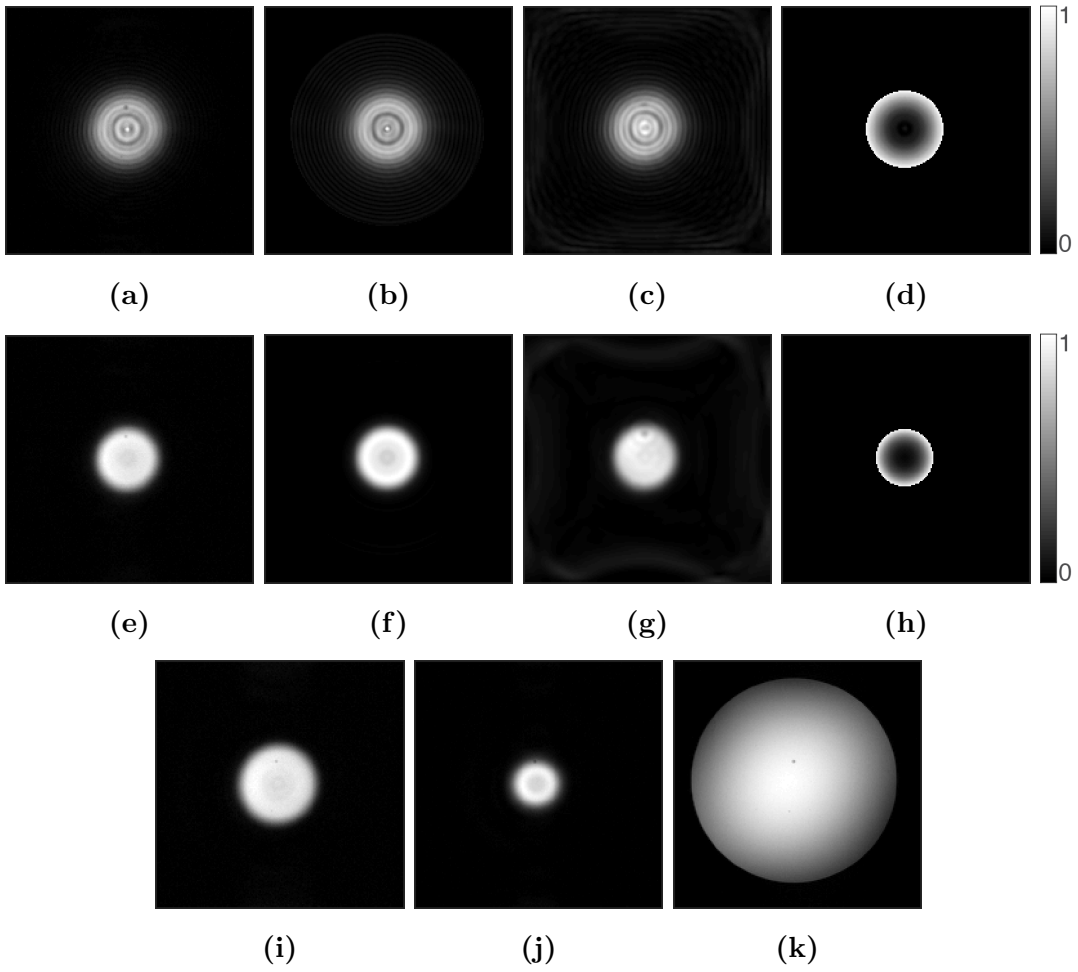

Figure 4.5: Images showing the features of (**a-d**) 2D chirp and (**e-j**) 2D HS1 pulses, when used to excite a cylindrical volume in a phantom (**k**). In all cases, the image slice orientation is perpendicular to the cylinder axis. **a,e**: Images acquired with the multishot spin-echo sequence. **b,f**: Bloch simulated excitation profiles. **c,g**: Images acquired with the single-shot spin-echo sequence using spiral readout. **d,h**: Bloch simulated normalized phase images. **i**: Multishot spin-echo image acquired in the presence of a +50 Hz frequency offset, which increases the excitation radius. **j**: Multishot spin-echo image acquired in the presence of a +50 Hz frequency offset, but using a 2D HS1 pulse with inverted $\phi_{\mathrm{RF}}(t)$, which decreases the excitation radius. **k**: Gradient echo axial image of the phantom (1.5% agar and 0.1 mM Gd). Images obtained from both simulation and experiment used a FOV of 192 × 192 mm and matrix size 192 × 192. *TR* of 200 ms and *TE* of 50 ms were used in all acquisitions.

window k-space filter, which is the Fourier transform of a jinc. Along the radial direction, the resolution is dictated by $k_{\max}$ of excitation k-space. In other words, the resolution is inversely proportional to the radial width of the cylindrical k-space filter. For the case of the 2D HS1 pulse that was used in simulations and experiments, the sequence shown in Figure 4.3b was simulated for a single point isochromat to estimate the spatial resolution [defined as full width half max (FWHM) of the PSF] and to obtain confirmation of a jinc-shaped PSF. These simulations showed the PSF is spatially invariant and its width scales linearly with $k_{\max}$. For example, for 1 cm resolution, $k_{\max} = 0.7168$ cycles/cm, and for 0.5 cm resolution, $k_{\max} = 1.4336$ cycles/cm. Although the resolution can be improved by increasing $k_{\max}$, which consequently increases the pulse bandwidth, this comes at the cost of a higher slew rate and gradient amplitude.

Multidimensional pulses can be applied in segments, although this requires multiple scans (shots) to completely cover excitation k-space. In addition, these pulses can be implemented with multiple coils using parallel RF transmission (pTx)[20, 21, 22]. Figure 4.6 shows simulations of such implementations of 2D FM pulses. When adequate sampling and radially symmetric quadratic phase conditions are met, multishot radial (Fig. 4.6f) and interleaved spiral (Fig. 4.6g) trajectories have the advantage of allowing the pulse length to be shortened and thus can reduce T_2^* effects during excitation at the cost of requiring increased number of shots to complete. Parallel excitation is another method to shorten the pulse length and has the advantage of requiring only a single shot to complete (Figs. 4.6d, 4.6h).

Bloch simulations were also performed to test the ability to compensate for B_1 inhomogeneity (Figs. 4.7a, 4.7b, 4.7c, 4.7d). The transmit B_1^+ profile of a 14.4 cm diameter single loop coil, as calculated from the Biot-Savart equation, is shown in Figure 4.7b. The simulation result with the loop coil B_1^+ profile imposed, but not compensated (Fig. 4.7c), shows a nonuniform excitation profile, with a greater excitation near the coil due to the larger B_1^+ in that region. After applying compensation (Fig. 4.7d), using the same peak power, a significant

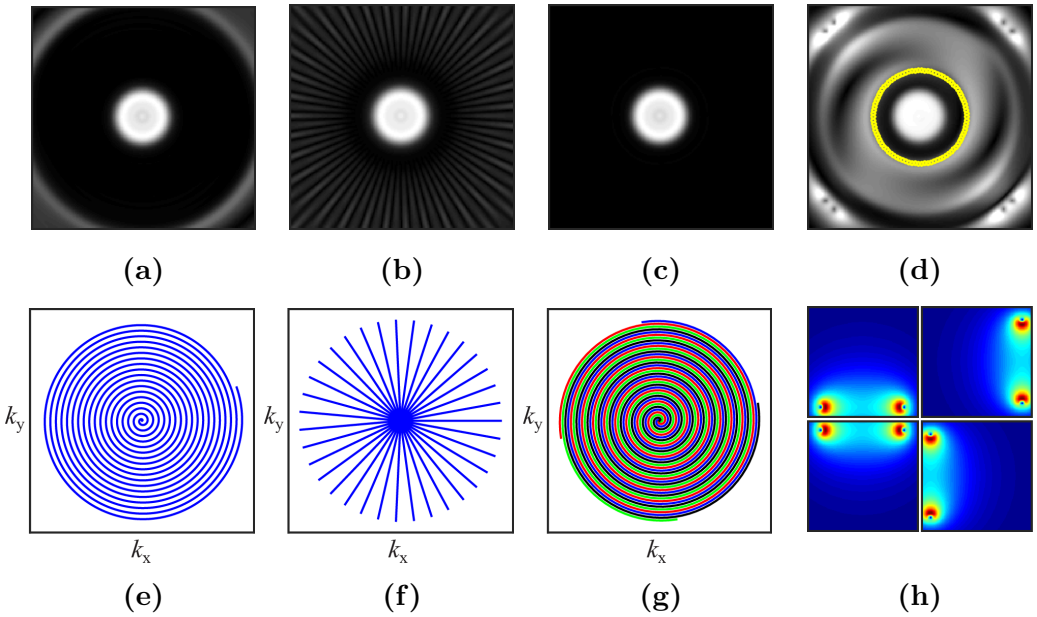

Figure 4.6: Excitation profile of the 2D HS1 resulting from spiral sampling (**a**), multiscan radial sampling (**b**), and interleaved spiral sampling (**c**) demonstrates the ability to use multishot/interleaved excitation sampling schemes to reduce pulse width. In comparison to (**e**), single-shot spiral sampling of pulse width 16.384 ms, multiscan radial sampling (**f**) decreased the pulse width to 1.024 ms at the expense of requiring 35 excitations, while interleaved spiral sampling (**g**) decreased the pulse width to 4.096 ms at the expense of requiring 4 excitations. **d**: Multicoil parallel excitation profile of the 2D HS1 pulse using ROI specification[22] (indicated by yellow circle). **h**: Four coil elements placed along the sides of a square were used to accelerate excitation. Parallel transmission has the advantage of accomplishing single shot excitation with a reduced pulse width (4.096 ms) by taking advantage of the individual coil B_1^+ profiles.

improvement in uniformity is achieved. The excitation profile, which varied ∼50% from top to bottom in the noncompensated case, is decreased to within ∼6% with compensation. The lower flip angle resulting from compensation is due to the average B_1 being lower as compared to the noncompensated case (Fig. 4.4a). The flip angle can be increased by increasing the peak B_1 amplitude.

Further simulations were performed to investigate the effects of B_0 inhomogeneity having spatial distribution proportional to $x^2 - y^2$ (Fig. 4.8d). Distortions to the excited disc are seen with the 2D HS1 pulse without (Fig. 4.8a) and with (Fig. 4.8b) B_0 compensation. The disc is highly distorted in the noncompensated case, whereas some improvement in the excitation profile is observed when using the B_0-compensated pulse. Although the compensated pulse does not produce a perfect disc (Fig. 4.8c), the modest improvement shown supports the hypothesis that spatiotemporal phase coherence can be exploited for such purposes.

4.4.2 Experiments

Images of the cylindrical water phantom are shown in Figure 4.5. Experimental confirmation of selective excitation of a disc can be seen by comparing the gradient echo image (Fig. 4.5k) with spin-echo images excited by a 2D chirp (Fig. 4.5a) or 2D HS1 (Fig. 4.5e) pulse. These images are in good agreement with the simulation results (Figs. 4.5b, 4.5f). Good agreement between simulations and experiments are also evident in images acquired with the single-shot spiral readout following 2D chirp (Fig. 4.5c) or 2D HS1 (Fig. 4.5g) excitation. To reconstruct images from these data, the acquired k-space image data were density compensated and gridded using a Kaiser-Bessel gridding kernel[92], followed by 2D FFT. As shown in Figure 4.5i, a constant frequency offset of +50 Hz increases the excitation radius, in accordance with Eq. (4.7), because the carrier frequency ω_c is changed. For this same offset, when the RF frequency is swept in the opposite direction (equivalent to making A and B in Eqs. (4.1) and (4.11), respectively, opposite in sign), a decrease in excitation radius is observed (Fig. 4.5).

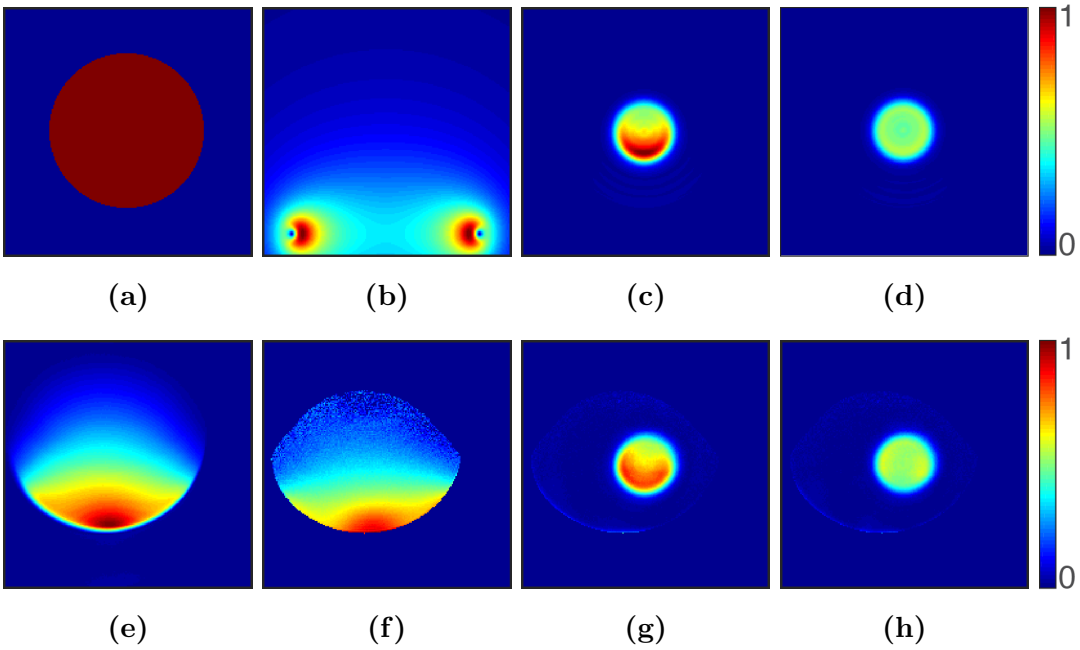

Figure 4.7: Demonstrations of B_1 compensation using 2D HS1 pulse. **a**: Circular object with uniform spin density used in simulations. **b**: Transmit B_1 profile (B_1^+) of a 14.4 cm diameter loop coil calculated from the Biot-Savart equation. **c**: Bloch simulation excitation profile in the presence of this nonuniform B_1^+ profile with no compensation shows greater excitation toward the coil where B_1^+ is greater. **d**: Excitation profile with B_1^+ compensation shows highly uniform excitation. Measured B_1^- (**e**) and B_1^+ (**f**) of the surface coil used in experiments. The ability to compensate for B_1^+ inhomogeneity can be seen by comparing noncompensated (**g**) and compensated (**h**) images. In both simulation and experiment, the lower flip angle resulting from compensation is due to the lower average B_1^+ compared with the noncompensated case (Fig. 4.4a).

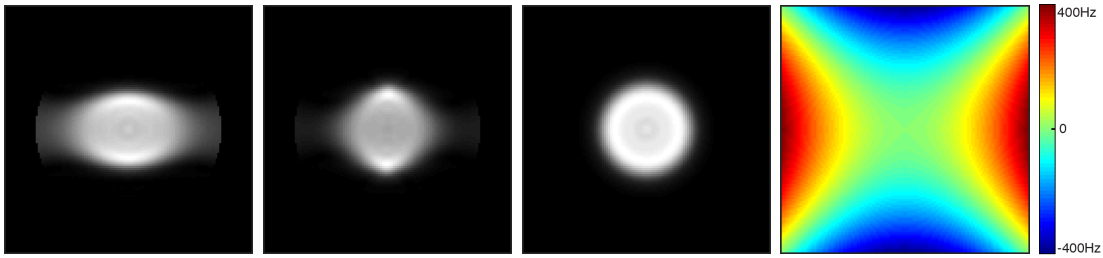

(a) **(b)** **(c)** **(d)**

Figure 4.8: Simulations of the excitation profile produced by 2D HS1 pulse when B_0 is proportional to $x^2 - y^2$. **a**: With the parent pulse, the excitation profile is no longer disc shaped due to B_0 inhomogeneity. **b**: The excitation profile of the redesigned pulse more closely resembles the desired profile shown in (**c**). **d**: The B_0 distribution (proportional to $x^2 - y^2$) used in the simulations.

Results of experiments using the 2D HS1 pulse to compensate for B_1 inhomogeneity are presented in Figures 4.7e-4.7h. As stated above, all images in this figure have been normalized with respect to the receive B_1^- profile to allow depiction of intensity distortions solely due to B_1^+ inhomogeneity. Figures 4.7e, 4.7f, which are the measured B_1^- and B_1^+ maps, respectively, show the inhomogeneous transmit and receive profiles of the surface coil used for the experiment. The image obtained with no compensation (Fig. 4.7g) shows ∼50% variation across the excitation region, with a tendency to excite most signal toward the coil, as expected from the B_1^+ profile and simulation results. A comparison of this image with the compensated image (Fig. 4.7h) reveals a significant improvement, whereby variation across the excitation region has been reduced to within ∼12%. The compensated 2D HS1 pulse pattern based on this B_1^+ profile is shown in Figure 4.4a. As mentioned above, the lower flip angle of the compensated profile is due to using the same peak B_1 for both compensated and noncompensated case.

Figure 4.9 depicts the excitation profiles of the 2D chirp, 2D HS1, and 2D jinc pulses in the presence of large B_0 inhomogeneity created by maximizing the current in the $x^2 - y^2$ shim coil. As compared to the ideal profiles of the 2D chirp and 2D HS1 pulses shown in Figures 4.9e and 4.9f, respectively, the excitation

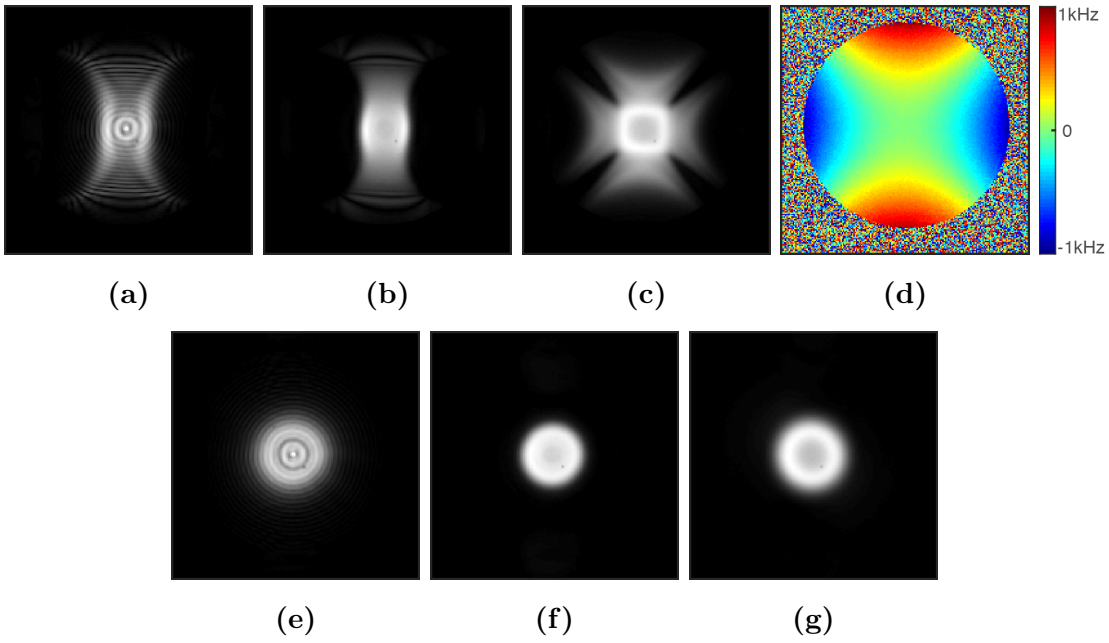

Figure 4.9: Spin-echo images showing the effect of B_0 inhomogeneity induced by a maximized x^2-y^2 shim. The volume was excited with 2D chirp pulse (**a**), 2D HS1 pulse (**b**), and a Gaussian truncated 2D jinc pulse (**c**) of 18 spiral turns and 13.14 ms duration. **d**: B_0 map obtained using the double gradient echo method. Desired ideal excitation profiles of the 2D chirp pulse (**e**), 2D HS1 pulse (**f**), and 2D jinc pulse (**g**) are shown for reference.

widths of the 2D chirp (Fig. 4.9a) and HS1 (Fig. 4.9b) pulses increased/decreased in regions where the field increased/decreased, in agreement with the expected changes in excitation radius when a frequency offset is applied (e.g., as shown in Figs. 4.5i, 4.5j). The 2D jinc profile somewhat resembled the B_0 profile but did not increase nor decrease in width in a consistent manner as the frequency offset varied.

Finally, the 2D FM pulses were used to image human brain of healthy volunteers under a protocol approved by our institutions IRB. A comparison of the standard spin-echo image (Fig. 4.10a) with the spin-echo image using a 2D HS1 excitation and fat suppression (Fig. 4.10b) shows the selected disc centered over the ventricles. The linear projections taken along the vertical (red) and horizontal (green) axes show no excitation beyond the radius of excitation. With no fat

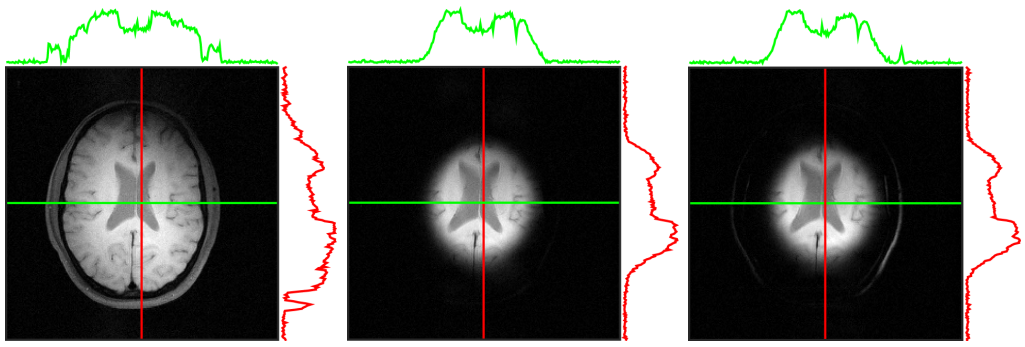

(a) (b) (c)

Figure 4.10: Human brain imaging with the 2D HS1 pulse. **a**: Reference spin-echo image (FOV 256 × 256 mm, matrix size 256 × 256, TE = 21 ms, TR = 455.024 ms). **b**: Spin-echo image using the 2D HS1 pulse for excitation. All acquisition parameters were fixed, except the 2D HS1 pulse was preceded by a fat-saturation module and TR = 475.66 ms. **c**: Imaging with the 2D HS1 pulse without fat saturation produces lipid signals at the periphery. These lipid signals arise from scalp and marrow because the fat disc is wider than the water disc, due to chemical shift.

suppression applied (Fig. 4.10c), additional outer rings appear, which are seen as spikes on the line plots. The latter is a consequence of fat signals having a different excitation radius due to chemical shift, as was demonstrated in the phantom images. The unwanted fat signal was easily eliminated using a fat suppression technique (Fig. 4.10b)[93].

4.5 Discussion and Conclusion

For certain applications, spatiotemporal techniques can offer unique advantages over conventional frequency- and phase-encoding techniques in MRI. In this work, a method of designing 2D pulses using a spatially dependent frequency sweep was introduced. In contrast to previous spatiotemporal methods in which the spatiotemporal nature of the excitation process is exploited for encoding spatial information, these new 2D FM pulses yield spatiotemporal phase coherence.

The ability to selectively "carve out" a target region was shown through both

simulations and experiments. Furthermore, the ability to compensate for transmit B_1^+ inhomogeneity was experimentally demonstrated using a surface coil by exploiting the spatiotemporal feature of the phase coherence induced by the pulse. Namely, B_1^+ inhomogeneity compensation is achieved by scaling the transmitter voltage of the pulse pattern based on the relative B_1^+ along the phase coherence trajectory.

As is well known when dealing with spiral trajectories, it is important to operate well within the slew-rate limits of the gradient system when designing the pulse. To accommodate this, the initial uniformly sampled spiral was resampled to meet gradient slew-rate constraints, and then the pulse pattern was modified accordingly (Fig. 4.4). Measurement and correction of the gradient nonlinearities and timing errors represent important steps in ensuring high fidelity. Failure to do this causes inaccurate sampling of the spiral k-trajectory, resulting in a skewed elliptical excitation and inaccurate B_1 compensation.

Doubling the bandwidth while keeping the time-bandwidth product constant causes a doubling of the SAR of both the 2D HS1 (5.957 W/kg) and the hard pulse (0.3492 W/kg), as expected from theory. However, if the bandwidth is doubled by doubling the time-bandwidth product to achieve the same flip angle, the SAR of the 2D FM pulse increases four-fold (11.913 W/kg). The latter is due to the excitation area, which is proportional to the square of the radius, increasing four-fold as well. Therefore, 4 times more power for equal power distribution or twice the peak B_1 amplitude is required.

As was shown, a frequency offset (e.g., caused by chemical-shift) leads to an increase or decrease of the excitation radius depending on the polarity of the offset and frequency sweep direction (Figs. 4.5i, 4.5j). As predicted based on Eq. (4.6), a positive (or negative) frequency offset causes a linear phase accumulation and results in added (or subtracted) parabolic phase because this linear phase is distributed along a spiral k-trajectory. Depending on the sign of the frequency offset, this additional phase either increases or decreases the steepness of the paraboloid, which is identical to increasing or decreasing A and B of Eqs. (4.1)

and (4.11). This is a unique property and can be advantageous in situations such as forgoing the need to implement a fat suppression module to eliminate circumscribing fat signals around the brain.

Experiments were carried out to investigate how the excitation profile changes in the presence of a highly inhomogeneous B_0 field induced by the $x^2 - y^2$ shim and how it compares with that produced by an amplitude modulated 2D jinc pulse using the same number of spiral turns. Driving the $x^2 - y^2$ shim to its limit caused a $\pm$1000 Hz variation in the B_0 field at 4T. With this B_0 variation, the excitation width of the 2D chirp and HS1 pulses increased proportionately in areas where the field increased (and vice versa), resulting in an excitation profile somewhat resembling the B_0 distribution in space. Although the 2D jinc pulse showed an excitation profile somewhat correlated to the field profile, it did not show a correlation to the polarity of the field variation as was the case with the 2D chirp and HS1 pulses. When driving the $x^2 - y^2$ shim current to its opposite extreme, the polarity of inhomogeneity rotated by $\pi/2$ (i.e., the offset varied from 0 to +1000 Hz along the x-direction and from 0 to -1000 Hz along the y-direction), and the excitation profile of the 2D chirp and HS1 pulses rotated by $\pi/2$ as well, whereas the 2D jinc pulse produced an image that looked similar to the previous case.

As shown in our initial simulation results (Fig. 4.8), by simply subtracting a phase that resembles the $x^2 - y^2$ field profile $\left(\propto \sqrt{k_{\mathrm{x}}^2(t) - k_{\mathrm{y}}^2(t)} \right)$ from the existing pulse table, an improvement in the excitation profile can be seen in comparison with the noncompensated case. Based on these results, and considering that the excitation profile of the 2D spatiotemporal pulses behave in a predictable manner as B_0 varies, it may be possible to fully compensate for B_0 inhomogeneity in future work. Although not shown here, an alternative approach to compensate for B_0 inhomogeneity was further explored through simulations using a similar method to that was used for B_1 compensation, although instead of modifying the pulse amplitude, the frequency of the RF pulse along the coherence trajectory was altered. This approach did show an improvement in the excitation profile compared

with the noncompensated case, but did not produce the degree of compensation hoped for. This was largely due to two reasons: 1) an inaccurate assumption of the coherence trajectory caused by a nonconstant spatially varying B_0, and 2) a change of the local quadratic phase coherence profile due to a spatially varying adjacent field environment along the coherence trajectory.

Although the k-space trajectories evaluated were limited to radially symmetric trajectories (Figs. 4.6e-4.6g) in this work, other trajectories such as an EPI-type raster trajectory can be used to excite a square-shaped region as long as the quadratic phase is allocated with radial symmetry. Also, by extending to three dimensions, for example by sampling a spherical trajectory, it should be possible to selectively excite a sphere for 3D imaging and to compensate for field inhomogeneity within.

Chapter 5

Designing 2D and 3D Selective Adiabatic Pulses

5.1 Introduction

Frequency modulated (FM) pulses have unique characteristics and certain advantages compared to conventional constant frequency amplitude modulated (AM) radiofrequency (RF) pulses. By modulating both the frequency and amplitude functions independently, the pulse width is decoupled from its RF bandwidth, which is usually stipulated by the pulse shape dependent time-bandwidth product or R-value. This decoupling facilitates even distribution of RF energy with respect to time by sequentially exciting (or inverting) spin isochromats, allowing broadband excitation without the need to increase peak RF power and sharp slice profiles. When using the chirp or hyperbolic secant (HS1)[36] pulse, sequential excitation produces a transverse phase that varies quadratically along the frequency sweep direction[83, 82]. This non-linear, spatially varying quadratic phase turns out to be advantageous for certain applications such as pseudo-echo-imaging, where the different local rephasing times of the transverse magnetization is utilized to encode spatial information[83, 82, 84, 85].

Another application in which FM pulses are vastly used is for *in vivo* NMR

and MRS experiments. Often, these experiments are carried out on surface coils to maximize receive sensitivity given the limited availability of concentration for the nuclei of interest. The spatial variation in flip angle due to the highly inhomogeneous B_1 field produced by surface coils is overcome by carefully sweeping the frequency. Called the adiabatic condition, this ensures that the magnetization will follow the effective field during adiabatic rapid passage provided that the effective field is swept at a slower rate than the rotation of magnetization about this effective field[14, 15]. Hence, adiabatic pulses enable uniform rotations of magnetization even with a B_1 field profile that spatially varies by an order of magnitude as long as a certain B_1 threshold is met, making it highly tolerant to extreme B_1 variation. Adiabatic pulses that are spatially selective are favorable in applications such as the navigator technique, where it is used as a pre-pulse to monitor the motion of a moving organ such as the diaphragm. Two-dimensional (2D) selective adiabatic pulses introduced by Conolly and colleagues showed selective inversion of an infinitely long cuboid by sampling k-space with amplitude modulation in one orthogonal direction and frequency modulation in the other[94]. In this work, we extend upon this and introduce a new method of designing multidimensional adiabatic pulses in both two- and three dimensions based on a sub-pulse approach. We further show that the intrinsically long length of these pulses can be shortened utilizing parallel transmission (pTx)[20, 21, 22]. To the best of our knowledge, this is the first demonstration of pTx being applied to adiabatic pulses.

5.2 Theory

5.2.1 Parent Pulse Design

The basic approach in designing multidimensional adiabatic pulses is to selectively excite in two-dimensions using sub-pulses and drive them adiabatically using a parent adiabatic pulse. Adiabatic pulses that possess a property known as offset-independent adiabaticity (OIA), ensures that isochromats whose resonance

frequency lies within the RF frequency sweep range meet the adiabatic condition equally[14, 15]. Thus, by evenly distributing RF energy with respect to time, an adiabatic full passage (AFP) is achieved and the longitudinal magnetization is inverted from M_z to $=M_z$. Possibly the most well-known pulse that can drive the adiabaticity based on the OIA principle is the hyperbolic secant pulse[36]. The pulse function of the HS1, in complex form, is given by

$$\omega_1^{\mathrm{HS1}}(t) = \omega_1^{\max}\mathrm{sech}(\beta\tau)e^{i\mu(\ln(\mathrm{sech}(\beta\tau)))} \tag{5.1}$$

where $\omega_1^{\max}$ is maximum RF amplitude (rad/s), $\tau = 2t/T_p - 1$ is a normalized time parameter with respect to pulse length T_p spanning the range $[-1, 1]$, and β and μ are real constants. The pulse table for an HS1 applied continuously with a constant gradient is shown in Fig. 5.1a.

As will be explained below, to drive adiabaticity, the parent pulse is implemented using discrete samples of the continuous form, with gradients blips inserted between each piece-wise constant segment to achieve selectivity[95]. Fig. 5.1b shows the discretized version (hard-blipped HS1). Compared to the continuous case, an infinite number of aliasing sidebands appear due to the time domain parent pulse being multiplied by a Dirac comb function in the discretization process, which is equivalent to convolution in the reciprocal domain. For a Dirac comb spaced $\delta t = T_p/N_{\mathrm{seg}}$ apart, where N_{seg} is the total number of sampled segments, the Nyquist criterion is given by

$$N_{\mathrm{seg}} \geq N_{\mathrm{Nyq}} = bw \cdot T_p = R \tag{5.2}$$

where N_{Nyq} is the minimum number of samples required to avoid aliasing and bw is the bandwidth of the pulse.

The piece-wise constant hard pulse segments of the hard-blipped HS1 can be further modulated by an amplitude modulation function such as that corresponding to a 2D Jinc pulse (Fig. 5.1c). Calling it the Jinc-blipped HS1, this piece-wise

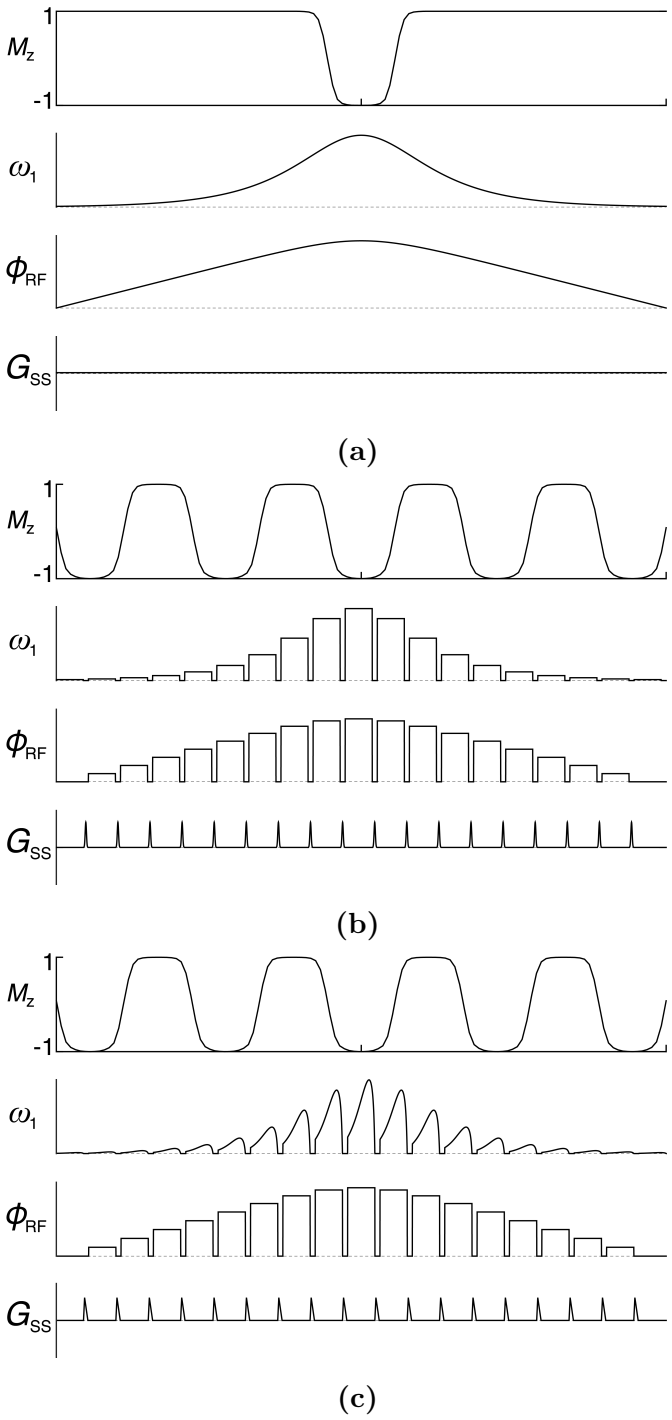

Figure 5.1: Amplitude, phase, and gradient for (a) continuous, (b) hard-blipped, and (c) Jinc-blipped HS1 (22.912 ms, R-value = 9.5). Compared to the (a) continuous HS1, an infinite number of aliasing sidebands appear for both the (b) hard-blipped and (c) Jinc-blipped cases. Peak RF power requirement is higher for the (c) Jinc-blipped HS1 than the (b) hard-blipped HS1, since it is directly proportional to the area ratio between the constant hard pulse element and the modulation Jinc function.

modulated discretized pulse produces the same inversion profile and aliasing sidebands as its piece-wise constant counterpart. However, peak RF power requirement is higher than the hard-blipped HS1 since this is inversely proportional to the area of the modulation function, which is less than the area of the constant hard pulse element.

5.2.2 Designing Multidimensional Adiabatic Pulses

For the ongoing illustration, a spiral k-trajectory 2D Jinc[91] is employed for the sub-pulse (Fig. 5.2b) and a hard-blipped HS1 for the parent pulse (Fig. 5.1b). First, the parent adiabatic pulse is discretized and sufficiently oversampled, followed by each piece-wise constant pulse segment being binned for the sub-pulse elements. Within each bin, a sufficiently sampled sub-pulse is placed and complex multiplied by the corresponding parent pulse segment. This is equivalent to modulating the amplitudes of consecutivesub-pulse elements by the parent amplitude function and adding the parent and sub-pulse phases, which results in the Jinc-blipped HS1. To re-center k-space for the subsequent sub-pulse element, a blip is inserted between the sub-pulses to nullify the area accrued under the gradients during the previous sub-pulse element. The result is a 2D adiabatic pulse that selectively inverts an infinitely long cylinder. The extension to three-dimensions (3D) is easily made by inserting additional blips along the remaining gradient direction between sub-pulse elements, thus selectively inverting a cylinder of finite height. This is equivalent to traversing N_{seg} identical spiral k-trajectories, each spaced $\gamma \int_0^{T_{\text{blip}}} G_{\text{blip}}(t)dt$ apart (Fig. 5.2a), where $G_{\text{blip}}(t)$ is the blip applied along the frequency sweep direction for duration T_{blip}. Each of the sampled 2D pulses are then modulated according to the amplitude and phase of the corresponding parent pulse segment. The resulting pulse is shown in Fig. 5.2c. If a one-dimensional (1D) slice selective pulse is used in place of the 2D spatially selective sub-pulse, one arrives at the spatially selective 2D adiabatic pulse previously described[94].

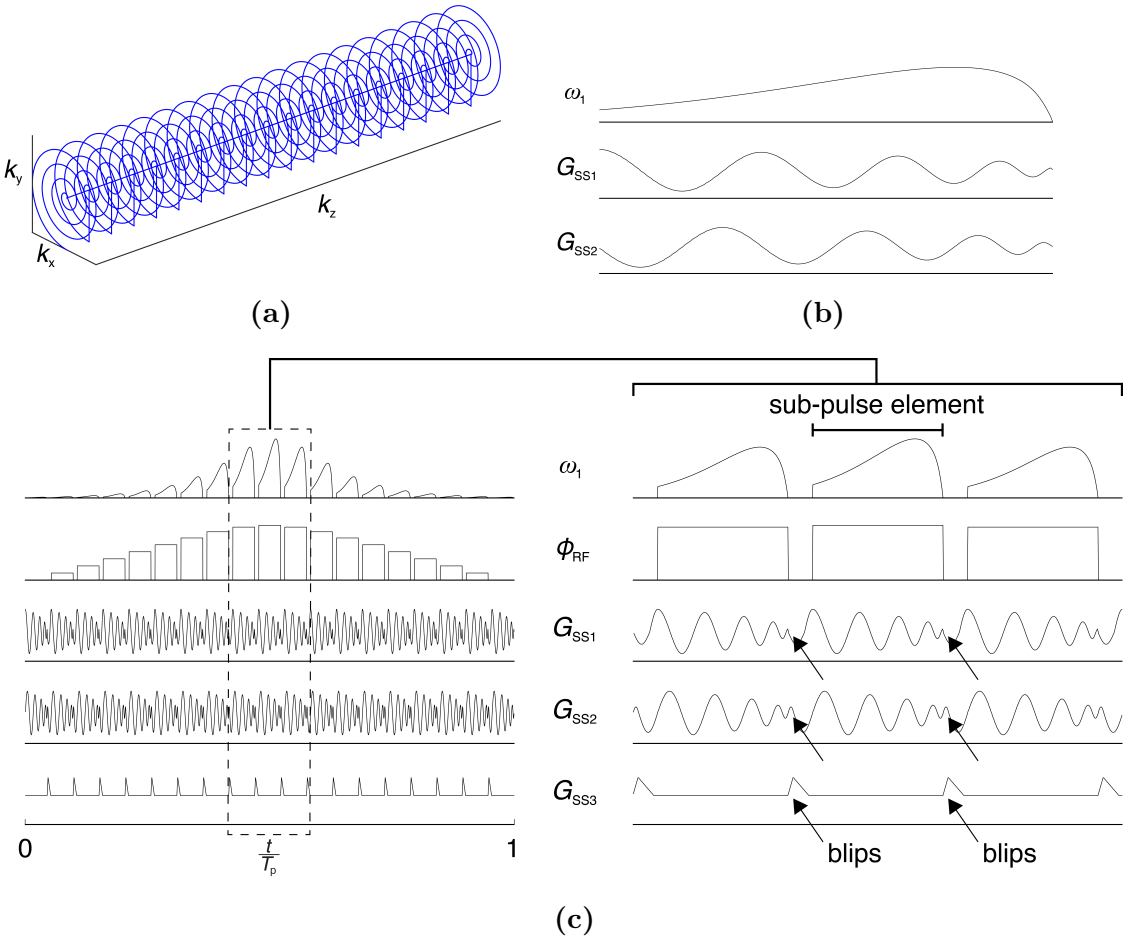

Figure 5.2: (a) 3D excitation k-space trajectory traversed sampling a (b) 3.5 turn spiral trajectory 2D Jinc sub-pulse driven adiabatically by a 19 sample 22.912 ms HS1 parent pulse with an R-value of 9.5 (Fig. 5.1b. Modulating the amplitudes of consecutive sub-pulse elements by the parent amplitude function and adding the parent and sub-pulse phases generates a multidimensional adiabatic pulse shown in (c). Blips are inserted between sub-pulses to nullify the gradient area accrued and re-center k-space as indicated by the magnification of the sub-pulse elements in the dashed box. The blips applied along the z gradient direction shifts each spiral trajectory in the k_z direction, enabling extension to three dimensions.

5.2.3 Imaging Sequences

It was confirmed through simulations that the 3D adiabatic pulse using 2D Jinc sub-pulses and HS1 parent pulse described above (Figure 5.2) selectively inverts a cylindrical volume of finite height. To extract this inversion profile experimentally, one can simply apply the 3D adiabatic pulse as an inversion preparation pulse and subtract the acquired signal from one acquired without inversion preparation applied. However, this requires two separate measurements, essentially doubling the acquisition time. A more efficient method is to use the 3D adiabatic inversion pulse in a spin-echo sequence as a spatially selective refocusing π-pulse following a non-selective $\pi/2$ excitation, eliminating the need of obtaining two acquisitions. When using an odd number of π-pulse(s) (Fig. 5.3a), isochromats along the blipped frequency sweep direction will experience different echo times (TE), where isochromats that were excited first refocus last and vice versa. An even number of π-pulses can compensate for the spatially quadratic phase along the frequency sweep direction to remove this difference in echo times, enabling all isochromats within the spatially selective volume to experience an identical TE with the added advantage of balancing any gradient imperfections (Fig. 5.3b). To ensure a clean inversion, half sine crusher gradients were placed before and after the 3D refocusing pulses, while for double echoes, the crusher amplitudes of the first and second refocusing pulses were applied with different strength to avoid any undesired stimulated echoes.

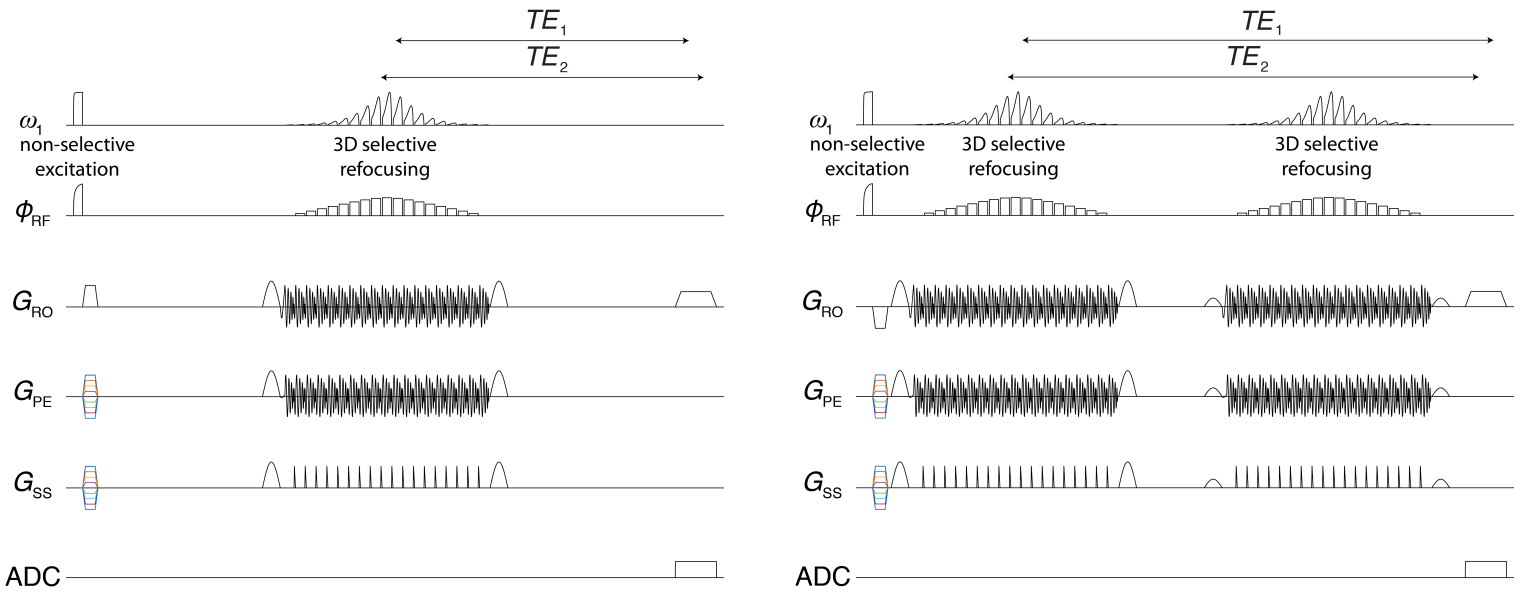

Figure 5.3: 3D adiabatic pulse can be used as a spatially selective refocusing π-pulse following a non-selective $\pi/2$ excitation in either a (a) single spin-echo or (b) double spin-echo configuration. Double spin-echo compensates for the spatially quadratic phase along the frequency sweep direction, enabling isochromats within the spatially selective volume to experience identical echo times with the added advantage of balancing any residual gradient imperfections.

5.2.4 pTx

It is possible to incorporate parallel transmission into the design of multidimensional adiabatic pulses. The strategy is to take advantage of the individual coil sensitivities through under sampling of the sub-pulses and driving them adiabatically with the fully sampled parent pulse, thus making it possible to shorten the intrinsically long pulse. This approach is plausible as long as the sub-pulse is designed according to the linear low-tip-approximation[35], as will be shown below.

5.3 Methods

5.3.1 Simulations

An in-house Bloch simulator programmed in C language and MATLAB (MathWorks, Inc., Natick, Massachusetts, USA) were used to validate the principles presented above. 3D simulations were carried out for a 22.912 ms pulse made of 3.5 turn spiral trajectory 256 element Jinc weighted 2D sub-pulses driven adiabatically by a 19 element HS1 parent pulse of time-bandwidth product 9.5 (Figure 5.2). The resulting M_z profiles were obtained from a 48x48x48 single isochromat matrix. Peak RF power was linearly swept to confirm spatially selective inversion and adiabaticity.

Pulse bandwidth evaluation was carried out by varying chemical shift and SAR calculations based on the time integral of $B_1(t)$-squared were done using peak B_1 needed for 95% inversion ($M_z = -0.9M_0$). To verify its use as a 3D refocusing pulse, 4 separate spin-echo (Fig. 5.3a) simulations were generated and summed using EXORCYCLE phase cycling[96]. It was confirmed that the resulting transverse magnetization after selective refocusing was identical to the profile attained after selective inversion of an initial magnetization along M_z.

Parallel transmission was simulated utilizing the sensitivity of 8 coil elements[97]

shown in Fig. 5.4c. The 3.5-turn 256 sample spiral k-trajectory used above was under sampled by 4 (Fig. 5.4g). Using the excitation profile obtained from the fully sampled sub pulse as the target excitation pattern, the spatial domain method[22] was applied, in which a least squared method was used to solve the minimization problem. This generated 8 distinct sub-pulses based on the 4-fold under sampled spiral k-trajectory for each coil. These sub-pulses were then used to design 8 distinct 3D pulses driven adiabatically by the same parent HS1, which were then applied to each coil element in parallel for pTx adiabatic inversion.

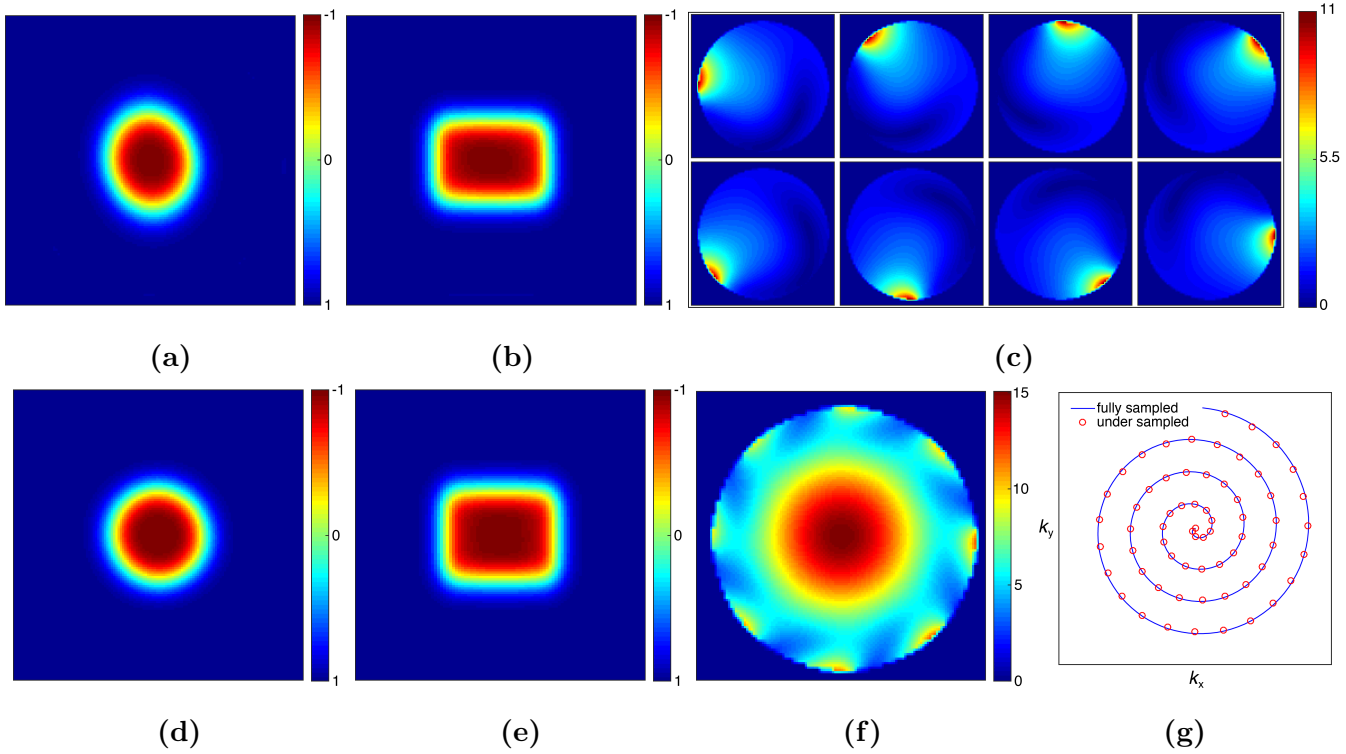

Figure 5.4: Inversion profile obtained using parallel transmission along the (a) axial and (b) coronal views using the coil profiles shown in (c). Corresponding profiles (d,e) obtained using the fully sampled pulse operating in a circularly polarized mode (f). The pTx pulses were generated by under sampling the spiral k-trajectory of the sub-pulse by 4-fold, as shown in (g), reducing the overall pulse length from 22.912 ms to 8.32 ms.

5.3.2 Experiments

3D refocus profile was experimentally verified on a Varian DirectDrive^{TM} console (Agilent Technologies, Santa Clara, CA) interfaced to a 90 cm 4T magnet (Oxford Magnet Technlology, Oxfordshire, UK) with a clinical gradient system (model SC72, Siemens, Erlangen, Germany). The same pulse verified through simulations was used as a refocusing π-pulse in a double spin echo sequence (Fig. 5.2b) on a cylindrical water phantom doped with 1.5% agar and 0.1 mM Gd ($T_1 \sim 1$ s and $T_2 \sim 160$ ms). The gradients, which were well within the gradient slew-rate constraint, were measured[88] and fine-tuned for all three directions. Although the spiral gradients showed minimum distortion, the blip gradient exhibited a prolonged undershoot that leaked into the subsequent sub-pulse. To compensate for this, a gradient corrected parent HS1 pulse was regenerated, which was then used to construct a gradient corrected 3D pulse.

Finally, images of the human brain from healthy volunteers were obtained under a protocol approved by our institutions IRB. Double spin-echo images using 3D adiabatic inversion and standard spin-echo images with identical sequence parameters were obtained for comparison. A 16-element transverse electromagnetic (TEM) head coil[89] was used in all experiments.

5.4 Results

5.4.1 Simulations

The volumetric slice image and inversion profiles along the axial (Ω_x-Ω_y), coronal (Ω_x-Ω_z), and sagittal (Ω_y-Ω_z) planes are shown in Figs. 5.5a5.5b5.5c5.5d. In the axial view, a circular shape is selectively inverted, whereas a rectangular shape is inverted along both the coronal and sagittal directions. Thus, the 3D pulse (Figure 5.2) selectively inverts a cylinder of finite height. The spatial bandwidths along both the Ω_x and Ω_y (radial) directions follow the bandwidth of the 2D Jinc pulse assuming a gradient corresponding to the maximum amplitude of the spiral

gradients, and are the same due to radial symmetry. The spatial bandwidth along the Ω_z (height) direction is given by the frequency sweep range of the parent HS1 pulse. Sweeping the RF amplitude and plotting the trace of M_z through the center for various offset frequencies along both the radial Ω_x-direction and height Ω_z-direction, the following properties are observed. In the Ω_z-direction (Fig. 5.5e), a linear regime ($\omega_1^{max}/2\pi = 0 - 250$ Hz) and adiabatic regime ($\omega_1^{max}/2\pi = 325$ Hz $-$) is observed, identical to the profile produced by the Jinc-blipped HS1. In the Ω_x-direction (Fig. 5.5f), a similar linear and adiabatic regime is observed. However, the profile along the radial direction increases and flattens out as ω_1^{max} is increased.

Figure 5.4 shows results obtained through the spatial domain method[22] for parallel transmission using 8 coil elements[97]. Utilizing the coil sensitivity profiles shown in Fig. 5.4c, the 4-fold under-sampled sub-pulse reduced the pulse length to 8.32 ms. The inversion profile generated by these pTx pulses are shown in Figs. 5.4a,5.4b. For comparison, Figs. 5.4d,5.4e are the inversion profiles of the fully sampled pulse ($T_p = 22.912$ ms) obtained by driving the 8 coils in a circularly polarized (CP) mode (Fig. 5.4f). The coronal view inversion profiles (Fig. 5.4b,5.4e) show excellent agreement. In the axial view, pTx produced a skewed oval shaped inversion profile (Fig. 5.4a) instead of the expected circular inversion profile generated by the fully sampled pulse (Fig. 5.4d).

5.4.2 Experiments

Phantom experiment results are shown in Figure 5.6. The axial, sagittal, and coronal views (Figs. 5.6a,5.6b,5.6c) of the phantom were obtained from a double spin-echo sequence using an adiabatic half passage (AHP) for excitation and adiabatic full passage for slice refocusing. The corresponding views obtained from double 3D selective adiabatic refocus (Figs. 5.6d,5.6e,5.6f) shows a cylindrical inversion of finite height, agreeing well with simulation results (Figs. 5.6g,5.6h,5.6i). Overlaying the trace plots of Figs. 5.6a,5.6b (green) and Figs. 5.6d,5.6e (red)

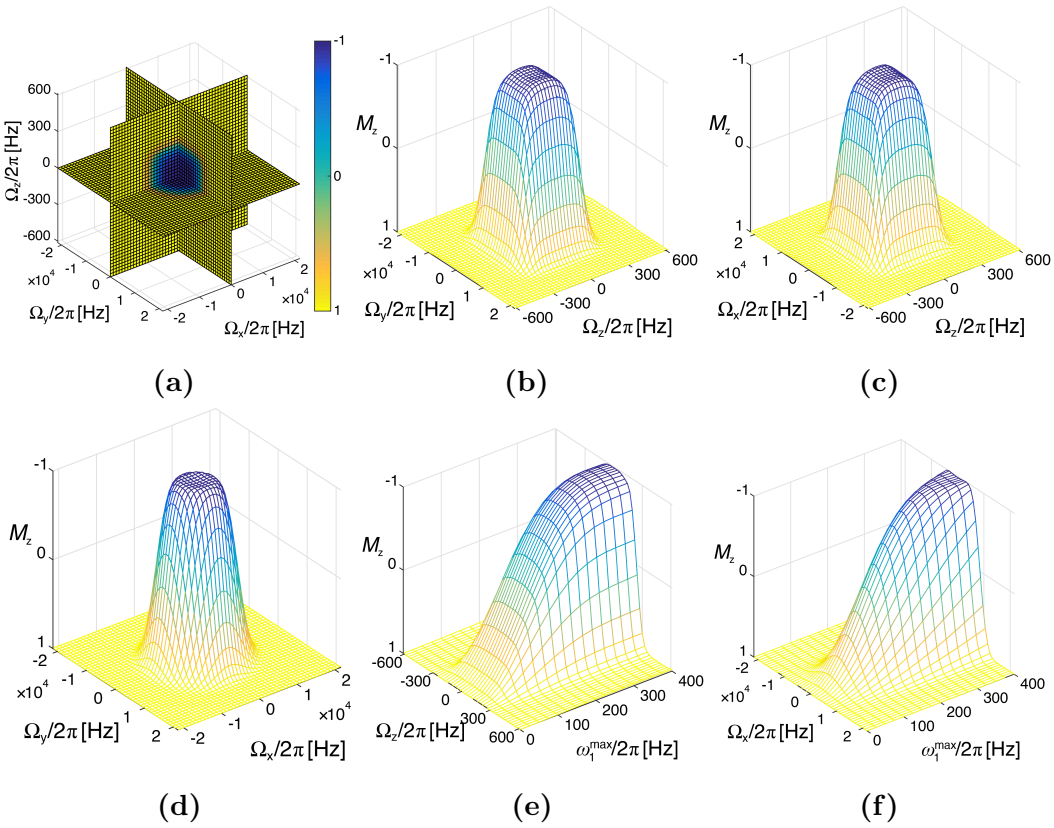

Figure 5.5: (a) Volumetric slice plot and inversion profiles along the (b) Ω_y-Ω_z plane, (c) Ω_x-Ω_z plane and (d) Ω_x-Ω_y plane obtained from Bloch simulations using the pulse in Figure 5.1 exhibits inversion of a cylinder with finite height. Sweeping the RF amplitude ($\omega_1^{\max}$) and plotting the trace of M_z through the center for various offset frequencies along both the (e) Ω_z-direction and (f) Ω_x-direction exhibit both a linear and adiabatic regime.

demonstrates selective inversion. The experimental 3D profiles appear sharper compared to the simulation results due to the image being obtained from a double spin-echo scheme, whereas the simulation shown is the inversion profile following pulse application. Inversion profiles along the radial and height directions were also obtained for various RF amplitudes. In agreement with simulation results, the radial profile increases and flattens out as $\omega_1^{\max}$ is increased and the profile along the height direction resembles that of a Jinc-blipped HS1.

In vivo images of the human brain are shown in Figure 5.7. Fig. 5.7a and Fig. 5.7 are the axial and coronal views acquired from double spin-echo (FOV = 256 x 256 x 256 mm, matrix size = 128 x 64 x 64) using 3D selective adiabatic refocusing (Fig. 5.3b). Comparing with standard spin-echo images (Figs. 5.7b,5.7d) acquired using identical sequence parameters (TE = 70 ms, TR = 1 s) clearly shows selective refocusing of a finite height cylindrical volume encapsulating the ventricles. Linear traces taken along the horizontal (green) and vertical (red) axes show no π-refocusing beyond the radius of inversion in the axial view, while sidebands, marked by gold dashed lines in Fig. 5.7c, emerged along the frequency sweep direction in the coronal view. In both coronal views (Figs. 5.7c,5.7d), flow artifacts are present due to absence of flow compensation during acquisition.

5.5 Discussion and Conclusion

A 3D selective adiabatic full passage pulse was simulated and experimentally verified. To minimize pulse width, the 2D spiral sub-pulses were minimized in length within the gradient hardware specifications, resulting in a pulse width of 1.024 ms, while an R-value of 9.5 for the parent pulse was used to limit the number of sub-pulse elements (N_{seg}) to 19 based on oversampling by twice the Nyquist rate[98]. The final pulse length was 22.912 ms.

Bandwidth was assessed independently along both the height Ω_{z} and radial Ω_{r} directions. Within each direction, both the spatial bandwidth and spectral bandwidth were evaluated by obtaining the inversion profiles for varying off-resonances.

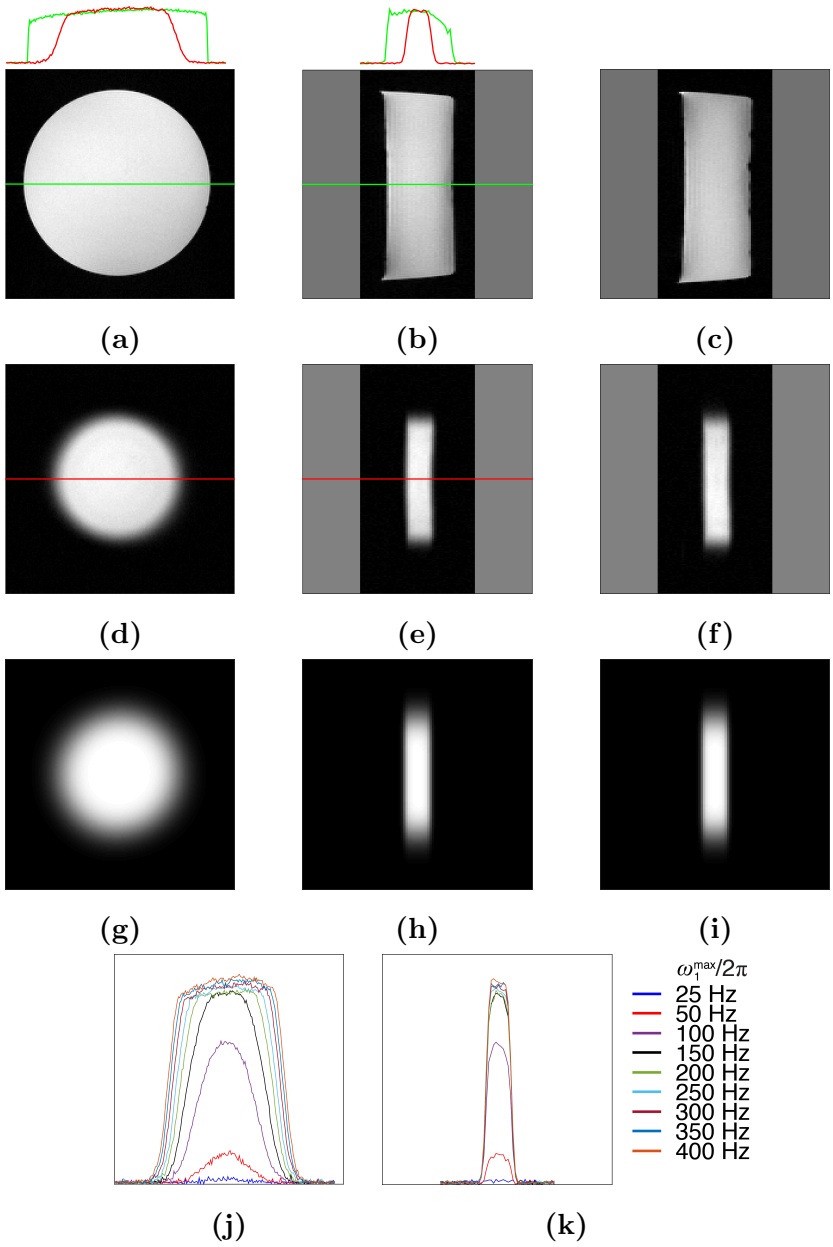

Figure 5.6: (a) Axial, (b) sagittal, and (c) coronal views of the phantom used. Compared with corresponding views (d-f) acquired using the double-spin echo sequence in Figure 5.3b clearly shows selective refocusing of a cylinder with finite height, in good agreement with simulation results (g-i). Experimental results exhibit slightly better selectivity than simulation results due to being obtained from a double-echo sequence. Refocusing profile along the radial (j) and height (k) direction for various ω_1^{max} demonstrates adiabatic property.

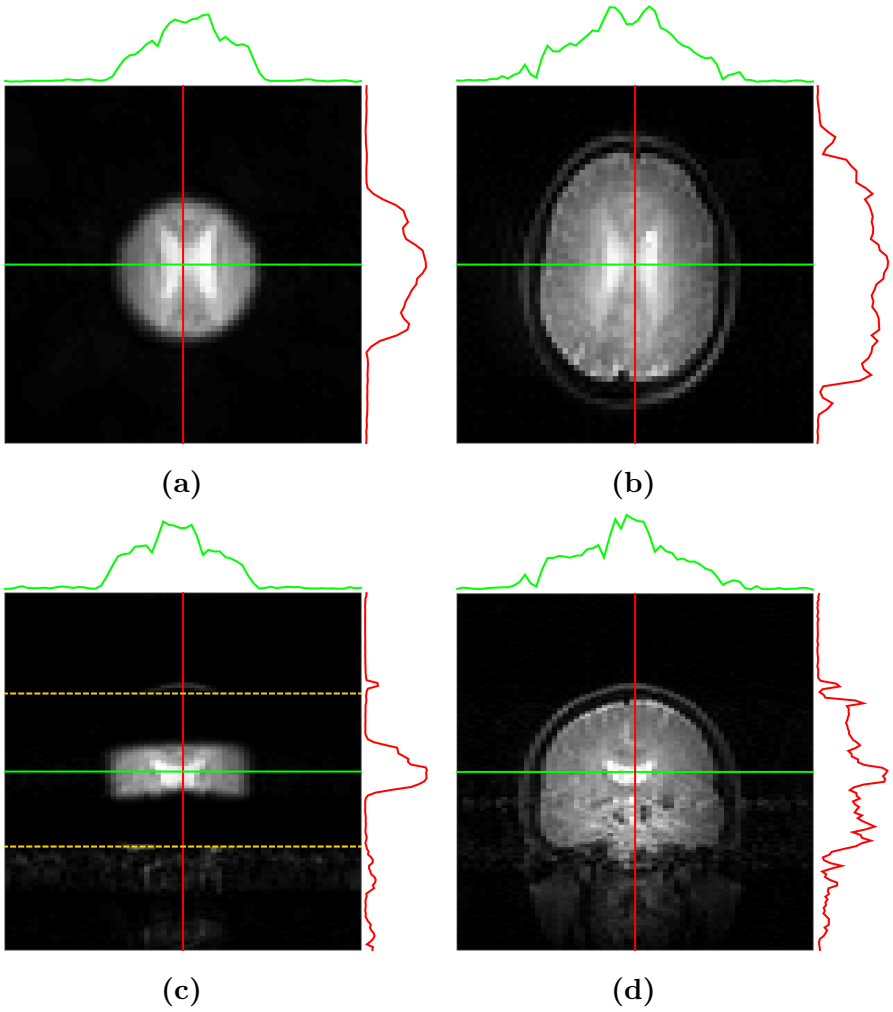

Figure 5.7: (a) Axial and (c) coronal views acquired from double spin-echo (FOV = 256 x 256 x 256 mm, matrix size = 128 x 64 x 64) using 3D selective adiabatic refocusing (Fig. 5.3b). Comparing with standard axial (b) and coronal (d) spin-echo images acquired from identical sequence parameters (TE = 70 ms, TR = 1 s) shows selective refocusing of a finite height cylindrical volume encapsulating the ventricles. Linear traces taken along the horizontal (green) and vertical (red) axes show for comparison. Sidebands appear along the frequency sweep direction marked by the gold dashed line (c). Flow artifacts are present due to absence of flow compensation during acquisition.

The spatial bandwidths were determined based on the blip gradients in the height direction and the maximum spiral gradient amplitude in the radial direction. The results are displayed in Fig. 5.8. For comparison, bandwidth along the height direction was analyzed for the continuous HS1 (Fig. 5.1a), hard-blipped HS1 (Fig. 5.1b), and Jinc-blipped HS1 (Fig. 5.1c). As expected, spatial displacement due to the off-resonance sensitivity ($\Delta x = \delta/bw \cdot thk$) for the continuous HS1 (Fig. 5.8a) is linear with respect to off-resonance, where Δx is the spatial displacement of inversion thickness thk produced by a pulse of bandwidth bw for an off-resonance δ. Spatial displacement equivalent to inversion thickness occurs at an off-resonance equal to the pulse bw (= 488 Hz). For the hard-blipped HS1 (Fig. 5.8b), aliasing sidebands are present and shift together with the baseband in the same linear manner with respect to off-resonance. However, the inversion profile falls off according to a sinc modulation as off-resonance is increased, which stems from the hard sub-pulse elements. Off-resonance at which inversion falls to half max occurs at $\delta = \pm 625$ Hz. Similarly, the Jinc-blipped HS1 inversion profile shows linear displacement with chemical shift and an additional modulation along the chemical shift dimension with a Gaussian shape profile dropping off to half max at $\delta = \pm 725$ Hz.

For the 3D pulse, the bandwidth in the Ω_z-direction follows the Jinc-blipped HS1. In the radial direction, there are no spatial aliasing sidebands. However, aliasing occurs in the off-resonance direction with the baseband profile falling to half max at $\delta = \pm 233$ Hz (Fig. 5.8d). For all pulses, the bandwidths in the spatial directions were extracted based on full width half max (FWHM) criteria at $\delta = 0$, while the spectral bandwidth was extracted using FWHM at Ω_z, $\Omega_r = 0$. In the Ω_z direction, both the spatial and spectral bandwidths were approximately equal to the bandwidth of the pulse. However, in the spectral dimension, both the hard-blipped HS1 and Jinc-blipped HS1 showed $\sim$5% lower bandwidth compared to the continuous HS1. This is explained by the extra sinc and Gaussian modulation, respectively, as off-resonance increases. In the Ω_r direction, the spectral bandwidth agreed with the pulse bandwidth. However, the spatial bandwidth created by the

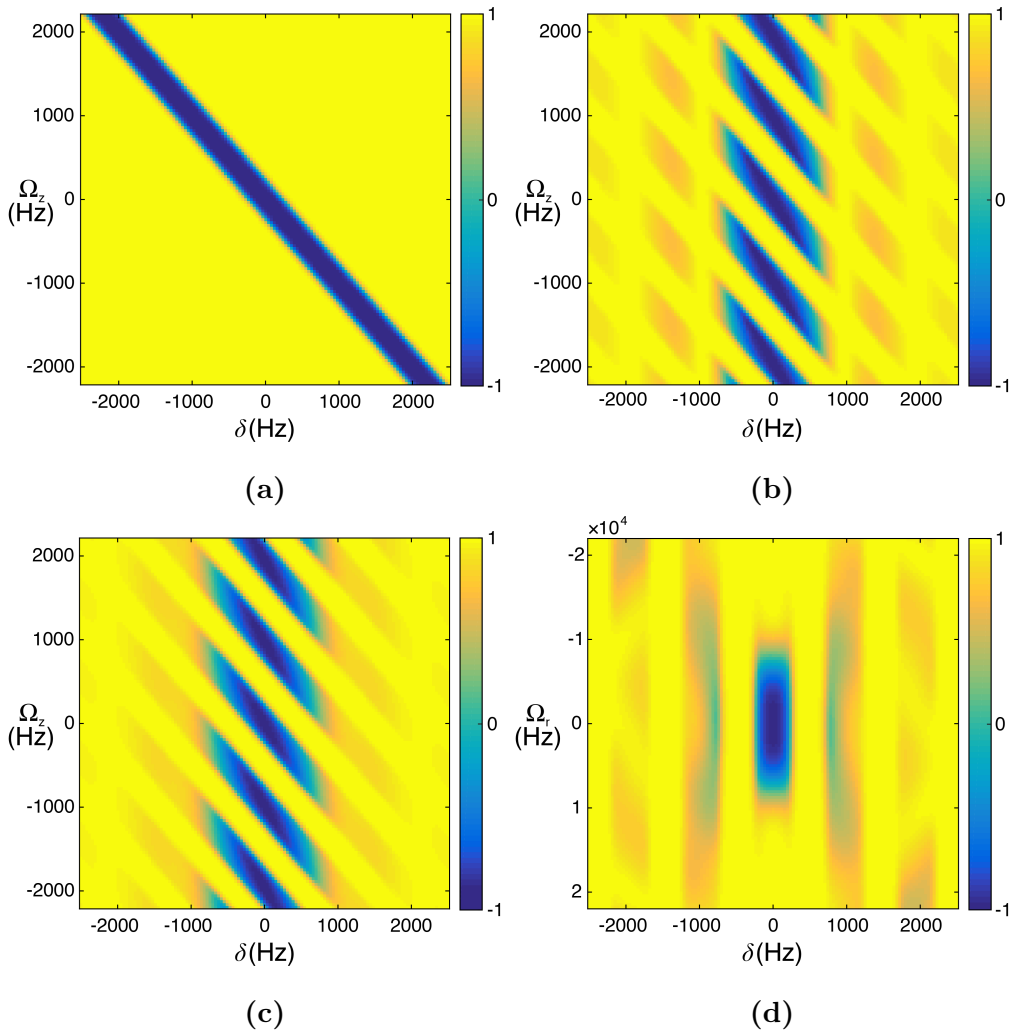

Figure 5.8: 3D plots depicting inversion profile dependency on spatial offset (Ω) and spectral offset (δ) for the (a) continuous HS1, (b) hard-blipped HS1, (c) Jinc-blipped HS1, and (d) 3D adiabatic pulse. Spatial displacement due to the off-resonance sensitivity is linear with respect to off-resonance, with aliasing sidebands present in addition to an extra (b) sinc and (c) Gaussian modulation along the chemical shift dimension for the blipped HS1 pulses. In the radial Ω_r direction (d), there are no spatial aliasing sidebands, but aliasing does occur in the off-resonance direction.

spiral gradients was much greater (∼33x). The results are displayed in Table 5.1.

	$\omega_1^{max}/2\pi$[4]	SAR[5]	spatial-*bw* (Hz)	spectral-*bw* (Hz)
continuous HS1	185	1.11	488	488
hard-blipped HS1	175	1	478	466
Jinc-blipped HS1 (Ω_z)[6]	270	1.14	478	460
Jinc-blipped HS1 (Ω_r)[7]	270	1.14	15600	466

Table 5.1

When designing a 2D pulse, sampling spiral k–space by spiraling in and spiraling out in an alternating manner eliminates the need for the k-refocusing blips and can thus shorten the pulse to 21.184 ms. However, the main barrier for shortening the overall pulse width, for both 2D and 3D, is the gradient hardware performance, which determine both the sub-pulse and blip length. For the gradient system used in this study, the maximum gradient strength was 50 mT/m with a slew rate of 10 T/m/s. Using gradient hardware standard on clinical systems (maximum gradient strength of 80 mT/m and slew rate 200 T/m/s), the overall pulse length can be decreased 4-fold, resulting in a 5.728 ms pulse, at the expense of a 4-fold higher peak RF amplitude. On animal systems which come with 1000 mT/m maximum gradient strength and 9000 T/m/s slew rate, this affords additional increase in the oversampling rate of the parent pulse, which move the sidebands further outwards. This facilitates single voxel spectroscopy with just two acquisitions, a 4-fold reduction from standard techniques[23].

Further optimization is realized from taking advantage of parallel transmission (pTx)[20, 21, 22]. Since the 2D sub-pulses are designed according to the principle of low-tip angle approximation, the sub-pulse can be under-sampled by exploiting

[4] peak RF power needed for 95% inversion (M_z = -0.9M_0)
[5] calculations taken from the time integral of $B_1(t)^2$ is reported relative to hard-blipped HS1
[6] spatial bandwidth along the height direction
[7] spatial bandwidth along the radial direction

coil sensitivity while being adiabatically driven through the parent pulse, thus shortening the overall pulse length. As described in the methods and results section, utilizing the sensitivity of 8 coil elements, the fully sampled sub-pulse was under sampled 4-fold, decreasing the total pulse length from 22.912 ms to 8.32 ms. Whereas the coronal view inversion profiles (Fig. 5.4b,5.4e) showed good agreement, in the axial view, a skewed oval shaped inversion profile was produced (Fig. 5.4a) using pTx instead of the circular shape generated by the fully sampled pulse (Fig. 5.4d). An identical skewed oval shape was observed in the excitation profile produced by the 2D pTx sub-pulse. Hence, this should improve if pTx sub-pulses are generated using more advanced methods to solve the spatial domain minimization problem.

Bandwidth comparison was carried out for the fully sampled pulse and pTx with the results presented in Table 5.2. Along the height direction, like the fully sampled pulse, pTx exhibits the same linear dependence on off-resonance and Gaussian modulation as off-resonance is increased. Also in accord, along the radial direction, the spatial bandwidth was much greater than the spectral bandwidth. However, the bandwidths in both the spatial and spectral dimensions turn out to be approximately 4 times greater than the fully sampled pulse, which is due to the 4-fold decrease in pulse width for the same R-value (9.5). Likewise, along the radial direction, no spatial aliasing sidebands were observed, while aliasing sidebands occurred in the off-resonance direction. The bandwidths in both the spatial and spectral dimensions are also approximately 4 times greater due to the the same reason.

Compared to the hard-blipped HS1 (Fig. 5.1b), the peak B_1 needed for 95% inversion ($M_z = -0.9M_0$) was greater for the continuous HS1 (Fig. 5.1a), which can be explained by the sharper inversion profile it produces. The greater peak B_1 of the Jinc-blipped HS1 relative to the hard-blipped HS1, which is due to the smaller area of the Jinc modulation function, is directly proportional to the area

[8] peak RF power needed for 95% inversion (M_z = -0.9M_0) for each coil element

[9] calculations taken from the time integral of $B_1(t)^2$ is reported relative to CP

	$\omega_1^{max}/2\pi$[8]	SAR[9]	spatial-*bw* (Hz)	spectral-*bw* (Hz)
CP (Ω_z)[6]	18	1	478	460
pTx (Ω_z)[6]	75	4.05	1914	1802
CP (Ω_r)[7]	18	1	13700	466
pTx (Ω_r)[7]	75	4.05	60250	1846

Table 5.2

ratio between the constant hard pulse element and the Jinc modulation element ($[\omega_1^{max}]_{\text{Jinc}} = [\omega_1^{max} \cdot area]_{\text{hard}}/[area]_{\text{Jinc}}$). Based on this, the relative SAR with respect to the hard-blipped HS1 calculated by taking the time integral of $B_1(t)$-squared was 111% for the continuous HS1 and 114% for the Jinc-blipped HS1. The relative SAR for pTx was 4.05 times greater with respect to CP, with a peak B_1 of 18 Hz for each coil operating in CP mode and 75 Hz for pTx. This reflects the 4-fold increase in bandwidth of the pTx pulses. The results are shown in Tables 5.1 and 5.2.

A new method of designing multidimensional selective adiabatic pulses was introduced and confirmed through both simulations and experiments. Although the pulse that was designed and used to confirm 3D selective adiabaticity was undesirably long, it was shown that by utilizing parallel transmission available on standard clinical systems, the pulse length could be shortened to be of practical use in applications such as inner volume selection, navigation techniques, and inversion in the presence of inhomogeneous B_1.

Chapter 6

Recent Developments, Summary, and Future Direction

6.1 B_0 Compensation in 1D

6.1.1 Introduction

As was shown in chapters 4 and 5, the ability to compensate for field inhomogeneity is a unique aspect of multidimensional FM pulses that has gained much interest as of late. Snyder et al[87] showed B_1 compensation through simulations by temporally adjusting the pulse according to the resonance trajectory and B_1 profile map. Modifying the amplitude function of spatially dependent frequency swept two-dimensional pulses based on its spatiotemporal phase coherence and B_1 map, B_1 compensation was demonstrated using simulations and experimentally verified in chapter 3[19]. There has also been work done on main field B_0 compensation. Ben-Eliezer et al utilized spatiotemporal encoding from a reconstruction point of view to image in the presence of B_0 inhomogeneity caused by metallic implants[99]. An attempt to compensate from an excitation perspective was made in chapter 3 by adjusting the phase of the pulse according to the B_0 profile map[19]. Although an improvement in excitation profile was observed, it

did not fully compensate to the desired excitation profile.

In the following, preliminary work on B_0 compensation along one dimension is presented. Key equations are laid down which have been verified through Bloch simulations, validating proof of principle.

6.1.2 Theory

As previously stated, exploiting the spatiotemporal nature inherent to frequency modulated pulses, B_1 compensation can be accomplished by correlating either the excitation trajectory[87] or maximum coherence trajectory[19] with a spatial B_1^+ map and rescaling the RF amplitude accordingly. To compensate for B_0 inhomogeneity, a similar approach is taken by correlating the excitation trajectory with a spatial B_0 map. However, instead of modulating the RF amplitude function, the frequency (or equivalently phase) function is modulated to meet the resonance condition based on the relative B_0 along the targeted excitation trajectory.

For a spatially uniform B_0, the excitation trajectory for an OIA FM pulse applied in the presence of a constant gradient is given by

$$\vec{r}_{\mathrm{o}}(t) = \frac{\omega_{\mathrm{RF}}(t) - \omega_{\mathrm{c}}}{\gamma G} \tag{6.1}$$

where $\omega_{\mathrm{RF}}(t)$ is the frequency modulation function with respect to carrier frequency ω_{c}, γ is gyromagnetic ratio, and G is gradient amplitude. Based on this, one can compensate for a spatially non-uniform B_0 profile, $B_0(\vec{r})$, by modifying the pulse frequency sweep function:

$$\omega_{\mathrm{RF}}^{\mathrm{comp}}(t) - \omega_{\mathrm{c}} = \gamma G \vec{r}_{\mathrm{o}}(t) + B_0\big(\vec{r}_{\mathrm{o}}(t)\big) \tag{6.2}$$

The OIA condition requires that all isochromats with resonance frequencies within the frequency sweep range meet the adiabatic condition equally. As a consequence, due to the frequency modulation function being altered to compensate for B_0, the amplitude function must be also be adjusted to meet OIA demands.

For an isochromat with resonance offset frequency Ω ($= \omega_0 - \omega_c$) that is within the frequency bandwidth, the OIA condition K is given by

$$K(t_\Omega) = \frac{\left(\omega_1(t_\Omega)\right)^2}{\dot{\omega}_{\mathrm{RF}}(t_\Omega)} \tag{6.3}$$

where t_Ω is time of resonance and $\dot{\omega}_{\mathrm{RF}}(t_\Omega)$ is the rate of change of the frequency sweep with respect to time at $t = t_\Omega$. Pulses that satisfy OIA, such as the chirp and HS1, have a constant K throughout the pulse. Hence, the amplitude function for compensation, $\omega_1^{\mathrm{comp}}(t)$ becomes

$$\omega_1^{\mathrm{comp}}(t) = \sqrt{\frac{\dot{\omega}_{\mathrm{RF}}^{\mathrm{comp}}(t)}{\dot{\omega}_{\mathrm{RF}}(t)}}\omega_1(t) \tag{6.4}$$

This modulation of the amplitude function to satisfy the OIA condition is equivalent to density compensation in excitation k-space. In the homogeneous case, excitation k-space trajectory is traversed with uniform density. However, when the frequency modulation function is modified to compensate for B_0, the sampled excitation k-space is no longer uniform and therefore, the existing amplitude modulation function must be density weighted to take this into account.

For a spatially quadratic B_0 profile given by $B_0^{\max} r^2$, the frequency modulation functions of the B_0 compensation pulse for the chirp and HS1, respectively, are given by

$$\omega_1^{\mathrm{chirp,comp}}(t) = \omega_c + bw\left(\frac{t}{T_p} - \frac{1}{2}\right)\left(1 + \frac{B_0^{\max}}{(\gamma G)^2} bw\left(\frac{t}{T_p} - \frac{1}{2}\right)\right) \tag{6.5}$$

$$\omega_1^{\mathrm{HS1,comp}}(t) = \omega_c - \mu\beta\tanh\left(\frac{2\beta}{T_p}\left(t - \frac{T_p}{2}\right)\right)\left(1 - \frac{B_0^{\max}}{(\gamma G)^2}\mu\beta\tanh\left(\frac{2\beta}{T_p}\left(t - \frac{T_p}{2}\right)\right)\right) \tag{6.6}$$

Integrating B_0 Compensation into Multidimensional Adiabatic Pulse Design

With the method explained above, compensation for B_0 can be integrated into the design process of multidimensional adiabatic pulses described in chapter 5 by generating a compensated parent FM pulse for a given inhomogeneous B_0 profile. The compensation method described above was derived assuming a continuous pulse. However, the parent pulse to be compensated is in discretized form, meaning a hard pulse approximation is used in which hard pulse elements, scaled proportional to its corresponding pulse element, have gradient blips inserted in between. When compensating for such discretized pulses, the extra inhomogeneity due to the presence of a static background inhomogeneity must be taken into account. To compensate for this, suppose that each piece-wise constant hard pulse element is of length $n_{\text{hard}}dt$ and each gradient blip is of length $n_{\text{grad}}dt$. During one hard pulse approximation (one hard pulse followed by a gradient blip), an isochromat at position r_{o} has evolved $\gamma B_0(r_{\text{o}})(n_{\text{hard}} + n_{\text{grad}})dt$ radians. Consequently, the effective frequency to be compensated is $B_0(r_{\text{o}})(n_{\text{hard}} + n_{\text{grad}})$ instead of $B_0(r_{\text{o}})$ used in the continuous case.

$$\omega^{\text{comp}}_{\text{RF, gapped}}(t) - \omega_{\text{c}} = \gamma G \vec{r}_{\text{o}}(t) + (n_{\text{hard}} + n_{\text{grad}}) B_0\big(\vec{r}_{\text{o}}(t)\big) \tag{6.7}$$

$$\omega^{\text{comp}}_{1,\text{ gapped}}(t) = \sqrt{\frac{\dot{\omega}^{\text{comp}}_{\text{RF, gapped}}(t)}{\dot{\omega}_{\text{RF}}(t)}}\omega_1(t) \tag{6.8}$$

This newly produced gapped compensation pulse can then be used as the parent pulse to design B_0 compensating multidimensional adiabatic pulses based on the method described in chapter 5.

6.1.3 Methods

B_0 compensation was simulated for a spatially varying quadratic main field profile ($B_0^{\max} r^2$) shown in Fig. 6.1a for both the chirp and HS1. For both pulses (T_{p}

= 4 ms, R-value = 40), the frequency modulation function was modified based on the local B_0 field along the target excitation trajectory, while the amplitude modulation function was corrected to meet OIA demands. Additional simulations were carried out to demonstrate B_0 compensation for 3D pulses assuming similar spatially varying quadratic inhomogeneity profiles (Fig. 6.3a).

6.1.4 Results

Fig. 6.1 shows the resulting profiles obtained from a homogeneous B_0 (blue), inhomogeneous B_0 with no compensation (red), and inhomogeneous B_0 with compensation (green), for both the chirp (Fig. 6.1b) and HS1 (Fig. 6.1c). Comparing the non-compensated profiles (red) with the compensated ones (green) shows drastic improvement, with the compensated profile becoming almost identical to the homogeneous case (blue). The pulses used in the simulations are shown in Fig. 6.2 for both the chip (Fig.6.2a) and HS1 (Fig.6.2b), with the original pulse (blue) and the compensated pulse (green) pulse overlaid.

Fig. 6.3 shows the resulting sagittal and axial views, respectively, obtained from a homogeneous B_0 (Figs. 6.3a, 6.3e), inhomogeneous B_0 with no compensation (Figs. 6.3b, 6.3f), and inhomogeneous B_0 with compensation (Figs. 6.3c, 6.3g), from a 3D adiabatic pulse with 2D Jinc sub-pulses driven adiabatically by a parent HS1. The 1D inhomogeneous B_0 profile is shown in Fig. 6.3d. Like the 1D case, comparing the non-compensated profiles (Figs. 6.3b, 6.3f) with the compensated ones (Figs. 6.3c, 6.3g) shows drastic improvement, with the compensated profile becoming almost identical to the homogeneous case (Figs. 6.3a, 6.3e).

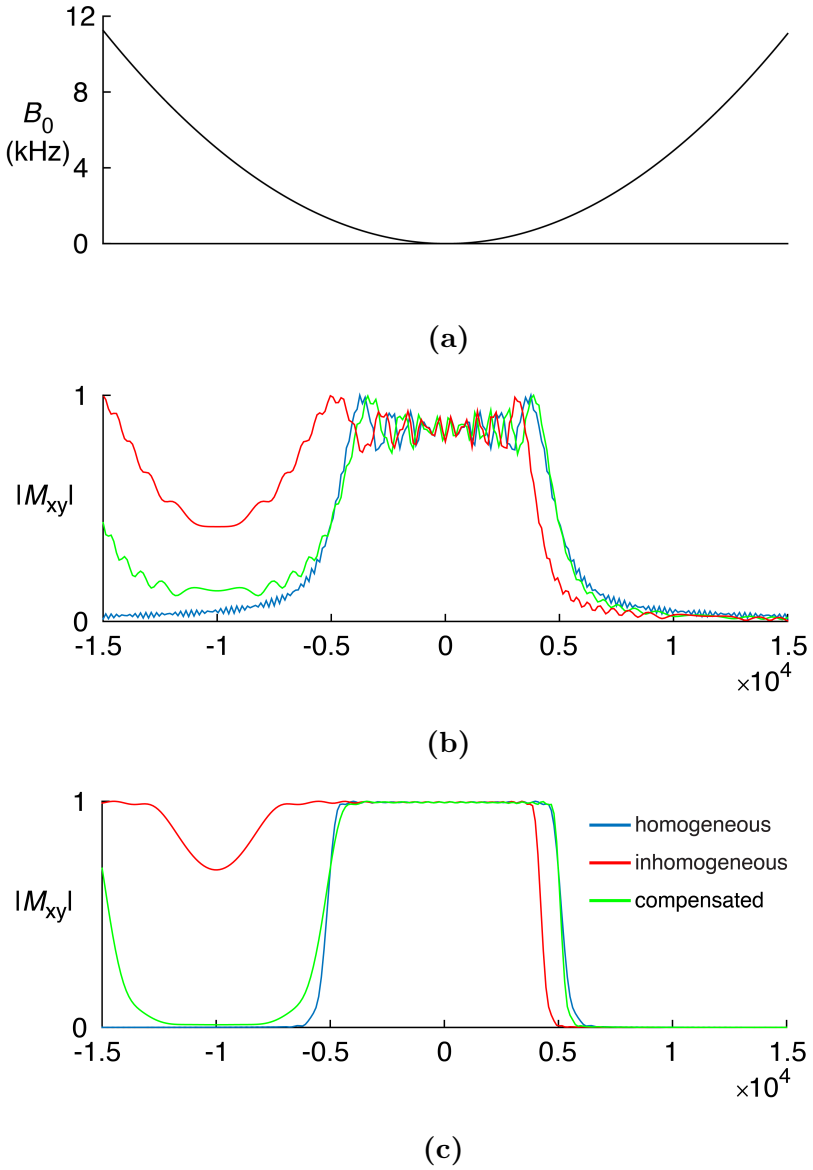

Figure 6.1: (**a**) Spatially quadratic B_0 profile used for compensation. Profiles obtained from (**b**) chirp and (**c**) HS1. Compared to the non-compensated profile (red), B_0 compensation (green) shows drastic improvement, almost identical to the homogeneous profile (blue).

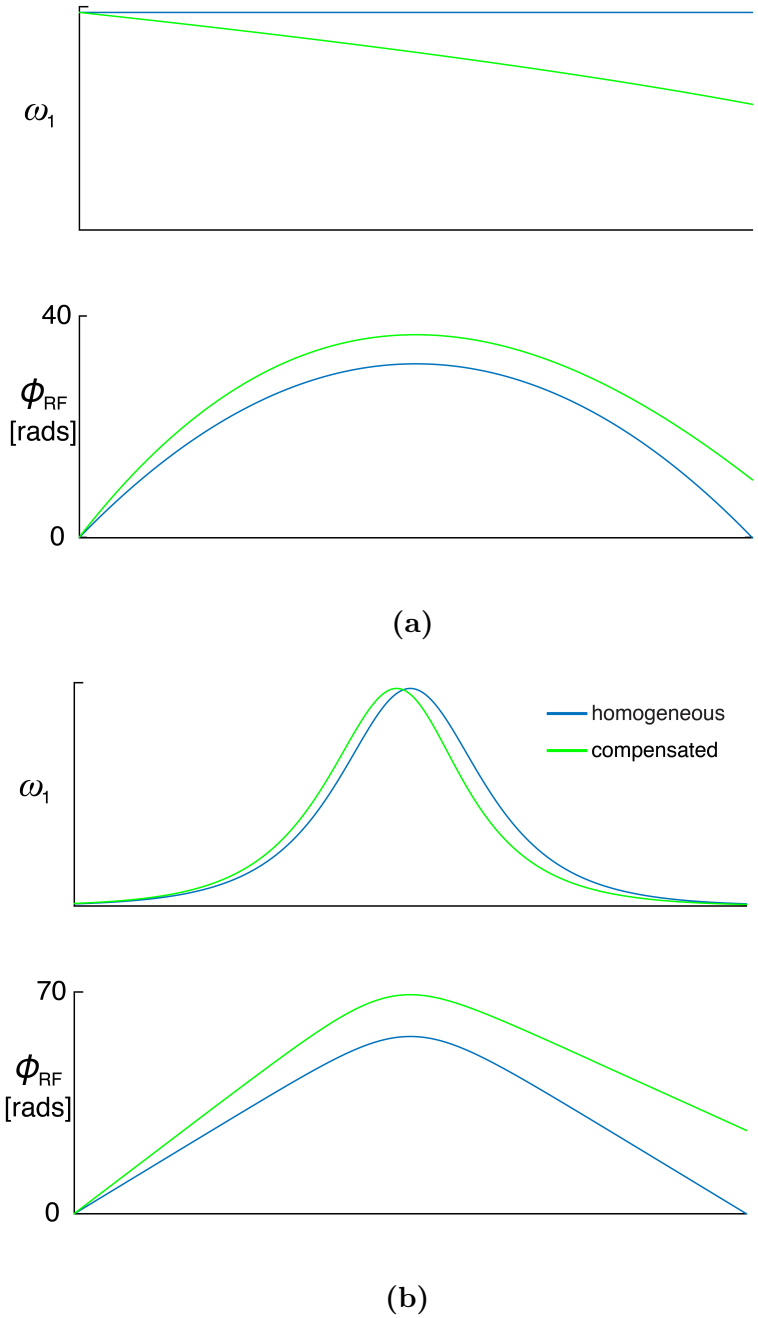

(a)

(b)

Figure 6.2: Overlay of the amplitude ω_1 and phase ϕ_{RF} functions of the original non-compensated pulse (blue) with the compensated pulse (green) for (**a**) chirp and (**b**) HS1.

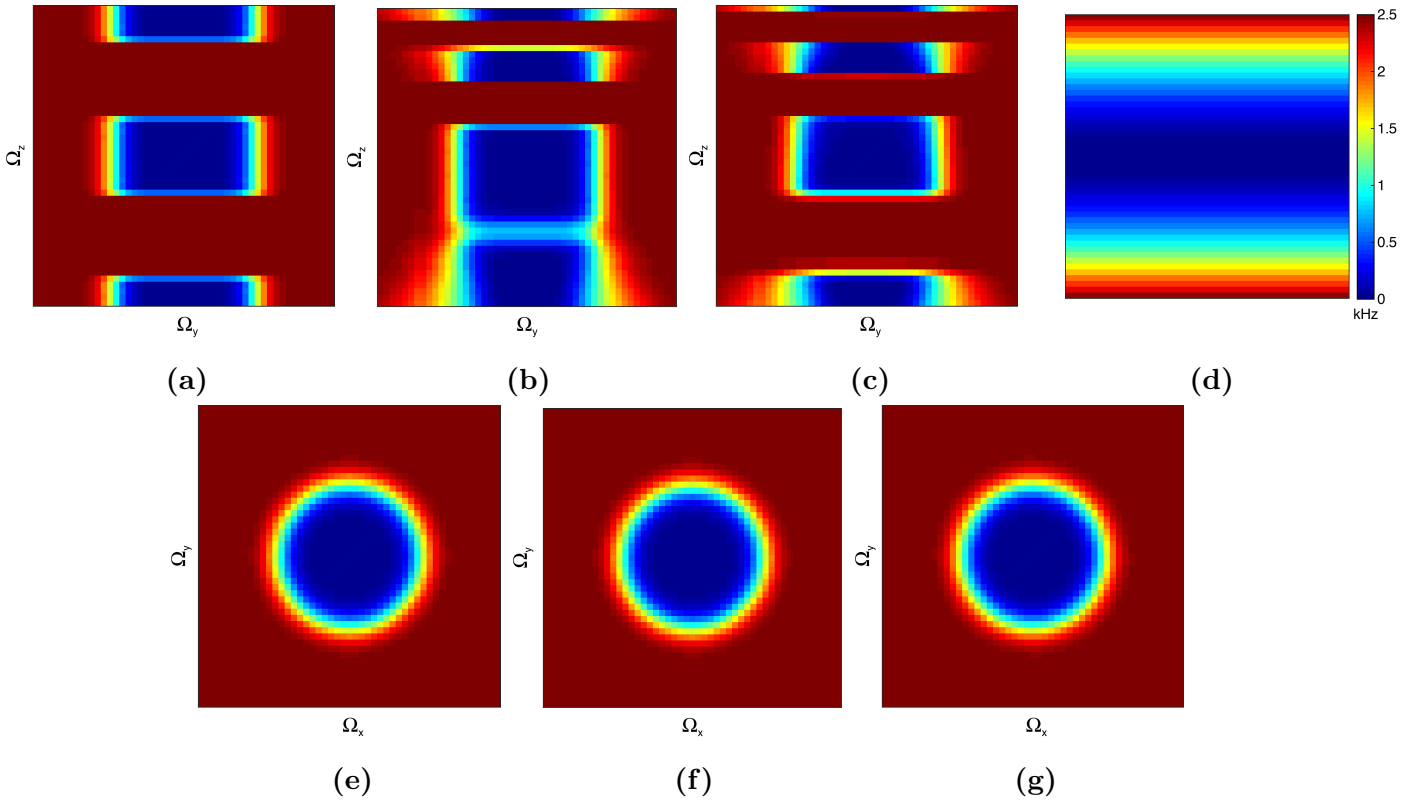

Figure 6.3: Sagittal (a) - (c) and axial (e) - (g) views in a homogeneous B_0 (a)(e), inhomogeneous B_0 with no compensation (b)(f), and inhomogeneous B_0 with compensation (c)(g) obtained from a 3D adiabatic pulse with 2D Jinc sub-pulses driven adiabatically by a parent HS1. (d) Inhomogeneous B_0 profile used. Like the 1D case, comparing the non-compensated profiles (b)(f) with the compensated ones (c)(g) shows drastic improvement, with the compensated profile becoming almost identical to the homogeneous case (a)(e).

6.2 Summary and Future Direction

New approaches applicable to magnetic resonance spectroscopic imaging with an emphasis on fast imaging and field inhomogeneity compensation was presented. First, an ultra-fast spectroscopic imaging method that indirectly extracts the transmural distribution of ATP utilization based on the T_1^{nom} technique was demonstrated, reducing data acquisition time by up to an order of magnitude. It was shown that in the normal heart, increase of cardiac work state is accompanied by an increase in ATP hydrolysis rate with no changes in CK flux rate, while there were no significant differences between EPI vs. ENDO concerning the ATP hydrolysis rate or CK flux rate in both baseline and high cardiac work states. Second, a pulse design method based on a k-space description was used to design two-dimensional frequency-modulated pulses that produce phase coherence in a spatiotemporal manner. Exploiting this spatiotemporal nature, compensation of the effect of B_1^+ inhomogeneity was experimentally verified, in agreement with simulation results. In addition, simulations were used to demonstrate partial compensation for B_0 inhomogeneity, suggesting extensions might also be used to compensate for static field inhomogeneity. Last, a method of designing two-dimensional and three-dimensional adiabatic π pulses that invert and refocus spins with high tolerance to B_1 inhomogeneity was introduced.

Preliminary results demonstrated full compensation of B_0 along one-dimension using FM pulses and the ability to incorporate it into the 3D adiabatic pulse design. Experimental verification can be carried out by maximizing the z^2 shim current, measuring the B_0 field, generate the corresponding compensating pulse, and verify compensation through the slice profile. Furthermore, utilizing the k-space formulation given in Eqs. (2.31) and (2.32), it should be possible extend compensation to 2D and 3D by adding the B_0 inhomogeneity into the formulation and derive a compensating pulse by solving the inverse problem.

Last, the studies carried out for indirect measure of the ATP hydrolysis rate

were terminal in nature. Implementing a closed chest cardiac protocol will enable continuous monitor of the bioenergetics and thus enable more physiological measurements. Preliminary studies were carried out on the 9.4 T system using a surface loop coil but due to the limitation in available RF power, we were unable to achieve adequate penetration of B_1. With sufficient hardware performance, closed chest spectroscopy should also be realizable.

References

[1] Paul A. Bottomley. Human in vivo NMR spectroscopy in diagnostic medicine: clinical tool or research probe? *Radiology*, 170(1):1–15, 1989. PMID: 2642336.

[2] Qing X. Yang, Jinghua Wang, Xiaoliang Zhang, Christopher M. Collins, Michael B. Smith, Haiying Liu, Xiao-Hong Zhu, J. Thomas Vaughan, Kâmil Uğurbil, and Wei Chen. Analysis of wave behavior in lossy dielectric samples at high field. *Magnetic Resonance in Medicine*, 47(5):982–989, 2002.

[3] Qiang Xiong, Lei Ye, Pengyuan Zhang, Michael Lepley, Jinfeng Tian, Jun Li, Liying Zhang, Cory Swingen, J. Thomas Vaughan, Dan S. Kaufman, and Jianyi Zhang. Functional consequences of human induced pluripotent stem cell therapy: Myocardial ATP turnover rate in the in vivo swine heart with postinfarction remodeling. *Circulation*, 127(9):997–1008, 2013.

[4] Qiang Xiong, Fei Du, Xiaohong Zhu, Pengyuan Zhang, Piradeep Suntharalingam, Joseph Ippolito, Forum D. Kamdar, Wei Chen, and Jianyi Zhang. ATP production rate via creatine kinase or ATP synthase in vivo: A novel superfast magnetization saturation transfer method. *Circulation Research*, 108(6):653–663, 2011.

[5] Meinrad Beer, Jörn Sandstede, Wilfried Landschütz, Marén Viehrig, Kerstin Harre, Michael Horn, Martin Meininger, Thomas Pabst, Werner Kenn,

Axel Haase, Markus von Kienlin, Stefan Neubauer, and Dietbert Hahn. Altered energy metabolism after myocardial infarction assessed by 31P-MR-spectroscopy in humans. *European Radiology*, 10(8):1323–1328, 2000.

[6] Meinrad Beer, Stefan Buchner, Jörn Sandstede, Marén Viehrig, Claudia Lipke, Alfons Krug, Herbert Köstler, Thomas Pabst, Werner Kenn, Wilfried Landschütz, Markus Kienlin, Kerstin Harre, Stefan Neubauer, and Dietbert Hahn. 31P-MR spectroscopy for the evaluation of energy metabolism in intact residual myocardium after acute myocardial infarction in humans. *Magnetic Resonance Materials in Physics, Biology and Medicine*, 13(2):70–75, 2001.

[7] Stefan Neubauer, Michael Horn, Monika Cramer, Kerstin Harre, John B. Newell, Werner Peters, Thomas Pabst, Georg Ertl, Dietbert Hahn, Joanne S. Ingwall, and Kurt Kochsiek. Myocardial phosphocreatine-to-ATP ratio is a predictor of mortality in patients with dilated cardiomyopathy. *Circulation*, 96(7):2190–2196, 1997.

[8] Hildo J. Lamb, Hugo P. Beyerbacht, Arnoud van der Laarse, Berend C. Stoel, Joost Doornbos, Ernst E. van der Wall, and Albert de Roos. Diastolic dysfunction in hypertensive heart disease is associated with altered myocardial metabolism. *Circulation*, 99(17):2261–2267, 1999.

[9] Jianyi Zhang, Norbert Wilke, Ying Wang, Yi Zhang, Chunshen Wang, Marcel H.J. Eijgelshoven, Yong K. Cho, Yo Murakami, Kâmil Uğurbil, Robert J. Bache, and Arthur H. L. From. Functional and bioenergetic consequences of postinfarction left ventricular remodeling in a new porcine model: MRI and ^{31}P-MRS study. *Circulation*, 94(5):1089–1100, 1996.

[10] Yo Murakami, Yi Zhang, Yong K. Cho, Abdul M. Mansoor, Jun K. Chung, Cuixia Chu, Gary Francis, Kâmil Uğurbil, Robert J. Bache, Arthur H. L. From, Michael Jerosch-Herold, Norbert Wilke, and Jianyi Zhang. Myocardial oxygenation during high work states in hearts with postinfarction remodeling. *Circulation*, 99(7):942–948, 1999.

[11] Yo Murakami, Jianyi Zhang, Marcel H. J. Eijgelshoven, Wei Chen, Wenda C. Carlyle, Yi Zhang, Guangrong Gong, and Robert J. Bache. Myocardial creatine kinase kinetics in hearts with postinfarction left ventricular remodeling. *American Journal of Physiology - Heart and Circulatory Physiology*, 276(3):H892–H900, 1999.

[12] Jianyi Zhang, Hellmut Merkle, Kristy Hendrich, Michael Garwood, Arthur H. From, Kâmil Uğurbil, and Robert J. Bache. Bioenergetic abnormalities associated with severe left ventricular hypertrophy. *The Journal of Clinical Investigation*, 92(2):993–1003, 8 1993.

[13] Qiang Xiong, Pengyuan Zhang, Jing Guo, Cory Swingen, Albert Jang, and Jianyi Zhang. Myocardial ATP hydrolysis rates in vivo: a porcine model of pressure overload-induced hypertrophy. *American Journal of Physiology - Heart and Circulatory Physiology*, 309(3):H450–H458, 2015.

[14] Alberto Tannús and Michael Garwood. Adiabatic pulses. *NMR in Biomedicine*, 10(8):423–434, 1997.

[15] Michael Garwood and Lance DelaBarre. The return of the frequency sweep: Designing adiabatic pulses for contemporary NMR. *Journal of Magnetic Resonance*, 153(2):155 – 177, 2001.

[16] Pierre-Marie Robitaille, Hellmut Merkle, Kristy Hendrich, Eugene Sublett, Brian Lew, Gregory Path, Arthur H. L. From, Robert J. Bache, Michael Garwood, and Kâmil Uğurbil. Spectroscopic imaging and spatial localization using adiabatic pulses and applications to detect transmural metabolite distribution in the canine heart. *Magnetic Resonance in Medicine*, 10(1):14–37, 1989.

[17] Kristy Hendrich, Hellmut Merkle, Sally Weisdorf, William Vine, Michael Garwood, and Kâmil Uğurbil. Phase-modulated rotating-frame spectroscopic localization using an adiabatic plane-rotation pulse and a single surface coil. *Journal of Magnetic Resonance*, 92(2):258 – 275, 1991.

[18] Albert Jang, Qiang Xiong, Pengyuan Zhang, and Jianyi Zhang. Transmurally differentiated measurement of ATP hydrolysis rates in the in vivo porcine hearts. *Magnetic Resonance in Medicine*, pages n/a–n/a, 2016.

[19] Albert Jang, Naoharu Kobayashi, Steen Moeller, J. Thomas Vaughan, Jianyi Zhang, and Michael Garwood. 2D pulses using spatially dependent frequency sweeping. *Magnetic Resonance in Medicine*, pages n/a–n/a, 2015.

[20] Ulrich Katscher, Peter Brnert, Christoph Leussler, and Johan S. van den Brink. Transmit sense. *Magnetic Resonance in Medicine*, 49(1):144–150, 2003.

[21] Yudong Zhu. Parallel excitation with an array of transmit coils. *Magnetic Resonance in Medicine*, 51(4):775–784, 2004.

[22] William Grissom, Chun-yu Yip, Zhenghui Zhang, V. Andrew Stenger, Jeffrey A. Fessler, and Douglas C. Noll. Spatial domain method for the design of RF pulses in multicoil parallel excitation. *Magnetic Resonance in Medicine*, 56(3):620–629, 2006.

[23] Roger J. Ordidge, Alan Connelly, and Joost A. B. Lohman. Image-selected in vivo spectroscopy (ISIS). A new technique for spatially selective NMR spectroscopy. *Journal of Magnetic Resonance (1969)*, 66(2):283 – 294, 1986.

[24] Walther Gerlach and Otto Stern. Der experimentelle Nachweis der Richtungsquantelung im Magnetfeld. *Zeitschrift fur Physik*, 9:349–352, December 1922.

[25] Isidor I. Rabi, Jerrold R. Zacharias, Sidney Millman, and Polykarp Kusch. A new method of measuring nuclear magnetic moment. *Phys. Rev.*, 53:318–318, Feb 1938.

[26] Felix Bloch, William W. Hansen, and Martin Packard. Nuclear induction. *Phys. Rev.*, 69:127–127, Feb 1946.

[27] Felix Bloch. Nuclear induction. *Phys. Rev.*, 70:460–474, Oct 1946.

[28] Felix Bloch, William W. Hansen, and Martin Packard. The nuclear induction experiment. *Phys. Rev.*, 70:474–485, Oct 1946.

[29] Edward M. Purcell, Henry C. Torrey, and Robert V. Pound. Resonance absorption by nuclear magnetic moments in a solid. *Phys. Rev.*, 69:37–38, Jan 1946.

[30] Richard R. Ernst and Weston A. Anderson. Application of fourier transform spectroscopy to magnetic resonance. *Review of Scientific Instruments*, 37(1):93–102, 1966.

[31] Raymond Damadian. Tumor detection by nuclear magnetic resonance. *Science*, 171(3976):1151–1153, 1971.

[32] David I. Hoult, Stephen J. Busby, David G. Gadian, George K. Radda, Rex E. Richards, and P. John Seeley. Observation of tissue metabolites using ^{31}P nuclear magnetic resonance. *Nature*, 252(5481):285287, November 1974.

[33] Paul C. Lauterbur. Image formation by induced local interactions: Examples employing nuclear magnetic resonance. *Nature*, 242:190–191, 1973.

[34] Peter Mansfield and Peter K. Grannell. NMR 'diffraction' in solids? *Journal of Physics C Solid State Physics*, 6:L422–L426, November 1973.

[35] John Pauly, Dwight Nishimura, and Albert Macovski. A k-space analysis of small-tip-angle excitation. *Journal of Magnetic Resonance*, 81(1):43 – 56, 1989.

[36] Michael S. Silver, Richard I. Joseph, and David I. Hoult. Highly selective $\pi/2$ and π pulse generation. *Journal of Magnetic Resonance*, 59(2):347 – 351, 1984.

[37] Nathaniel J. Powell, Albert Jang, Jang-Yeon Park, Julien Valette, Michael Garwood, and Magorzata Marjaska. Gradient rotating outer volume excitation (GROOVE): A novel method for single-shot two-dimensional outer volume suppression. *Magnetic Resonance in Medicine*, 73(1):139–149, 2015.

[38] Stig Ljunggren. A simple graphical representation of fourier-based imaging methods. *Journal of Magnetic Resonance*, 54(2):338 – 343, 1983.

[39] Donald B. Twieg. The k-trajectory formulation of the NMR imaging process with applications in analysis and synthesis of imaging methods. *Medical Physics*, 10(5):610–621, 1983.

[40] William A. Edelstein, James M. S. Hutchison, Glyn Johnson, and Thomas Redpath. Spin warp NMR imaging and applications to human whole-body imaging. *Physics in Medicine and Biology*, 25(4):751, 1980.

[41] Erwin L. Hahn. Spin echoes. *Phys. Rev.*, 80:580–594, Nov 1950.

[42] Truman R. Brown, B. M. Kincaid, and Kâmil Uğurbil. NMR chemical shift imaging in three dimensions. *Proceedings of the National Academy of Sciences of the United States of America*, 79(11 I):3523–3526, 1982.

[43] Samuel P. Bessman and Christopher L. Carpenter. The creatine-creatine phosphate energy shuttle. *Annual Review of Biochemistry*, 54(1):831–862, 1985. PMID: 3896131.

[44] Hadassa Degani, Maren Laughlin, Sharon Campbell, and Robert G. Shulman. Kinetics of creatine kinase in heart: A ^{31}P NMR saturation- and inversion-transfer study. *Biochemistry*, 24(20):5510–5516, 1985.

[45] John A. Bittl and Joanne S. Ingwall. Reaction rates of creatine kinase and ATP synthesis in the isolated rat heart. A ^{31}P NMR magnetization transfer study. *Journal of Biological Chemistry*, 260(6):3512–3517, 1985.

[46] Kâmil Uğurbil, Marc Petein, Rubin Maidan, Steve Michurski, and Arthur H. L. From. Measurement of an individual rate constant in the presence of multiple exchanges: application to myocardial creatine kinase reaction. *Biochemistry*, 25(1):100–107, 1986.

[47] Peter B. Kingsley-Hickman, Edward Y. Sako, Parekket Mohanakrishnan, Pierre-Marie L. Robitaille, Arthur H. L. From, John E. Foker, and Kâmil Uğurbil. ^{31}P NMR studies of ATP synthesis and hydrolysis kinetics in the intact myocardium. *Biochemistry*, 26(23):7501–7510, 1987.

[48] Xiaohong Wang, Qingsong Hu, Abdul Mansoor, Joseph Lee, Zongli Wang, TeChung Lee, Arthur H. L. From, and Jianyi Zhang. Bioenergetic and functional consequences of stem cell-based VEGF delivery in pressure-overloaded swine hearts. *American Journal of Physiology - Heart and Circulatory Physiology*, 290(4):H1393–H1405, 2006.

[49] Lepeng Zeng, Qingsong Hu, Xiaohong Wang, Abdul Mansoor, Joseph Lee, Julia Feygin, Ge Zhang, Piradeep Suntharalingam, Sherry Boozer, Abner Mhashilkar, Carmelo J. Panetta, Cory Swingen, Robert Deans, Arthur H. L. From, Robert J. Bache, Catherine M. Verfaillie, and Jianyi Zhang. Bioenergetic and functional consequences of bone marrowderived multipotent progenitor cell transplantation in hearts with postinfarction left ventricular remodeling. *Circulation*, 115(14):1866–1875, 2007.

[50] Jan van Deursen, Arend Heerschap, Frank Oerlemans, Wim Rultenbeek, Paul Jap, Henk ter Laak, and B Wieringa. Skeletal muscles of mice deficient in muscle creatine kinase lack burst activity. *Cell*, 74(4):621 – 631, 1993.

[51] Jingbo Liu, Chunsheng Wang, Yo Murakami, Guangrong Gong, Yutaka Ishibashi, Catherine Prody, Koichi Ochiai, Robert J. Bache, Catherine Godinot, and Jianyi Zhang. Mitochondrial ATPase and high-energy phosphates in failing hearts. *American Journal of Physiology - Heart and Circulatory Physiology*, 281(3):H1319–H1326, 2001.

[52] Kâmil Uğurbil. Magnetization-transfer measurements of individual rate constants in the presence of multiple reactions. *Journal of Magnetic Resonance*, 64(2):207 – 219, 1985.

[53] Sture Forsén and Ragnar A. Hoffman. Study of moderately rapid chemical exchange reactions by means of nuclear magnetic double resonance. *The Journal of Chemical Physics*, 39(11):2892–2901, 1963.

[54] Harden M. McConnell. Reaction rates by nuclear magnetic resonance. *The Journal of Chemical Physics*, 28(3):430–431, 1958.

[55] John A. Bittl, James A. Balschi, and Joanne S. Ingwall. Effects of norepinephrine infusion on myocardial high-energy phosphate content and turnover in the living rat. *The Journal of Clinical Investigation*, 79(6):1852–1859, 6 1987.

[56] Yun Ye, Chunsheng Wang, Jianyi Zhang, Young K. Cho, Guangrong Gong, Yo Murakami, and Robert J. Bache. Myocardial creatine kinase kinetics and isoform expression in hearts with severe LV hypertrophy. *American Journal of Physiology - Heart and Circulatory Physiology*, 281(1):H376–H386, 2001.

[57] Paul A. Bottomley, Ronald Ouwerkerk, Ray F. Lee, and Robert G. Weiss. Four-angle saturation transfer (FAST) method for measuring creatine kinase reaction rates in vivo. *Magnetic Resonance in Medicine*, 47(5):850–863, 2002.

[58] Qiang Xiong, Qinglu Li, Abdul Mansoor, Mohammad Nurulqadr Jameel, Fei Du, Wei Chen, and Jianyi Zhang. Novel strategy for measuring creatine

kinase reaction rate in the in vivo heart. *American Journal of Physiology - Heart and Circulatory Physiology*, 297(3):H1010–H1019, 2009.

[59] Michael A. Conway, Paul A. Bottomley, Ronald Ouwerkerk, George K. Radda, and Bheeshma Rajagopalan. Mitral regurgitation: Impaired systolic function, eccentric hypertrophy, and increased severity are linked to lower phosphocreatine/ATP ratios in humans. *Circulation*, 97(17):1716–1723, 1998.

[60] Christopher J. Hardy, Robert G. Weiss, Paul A. Bottomley, and Gary Gerstenblith. Altered myocardial high-energy phosphate metabolites in patients with dilated cardiomyopathy. *American Heart Journal*, 122(3, Part 1):795 – 801, 1991.

[61] Craig S. Smith, Paul A. Bottomley, Steven P. Schulman, Gary Gerstenblith, and Robert G. Weiss. Altered creatine kinase adenosine triphosphate kinetics in failing hypertrophied human myocardium. *Circulation*, 114(11):1151–1158, 2006.

[62] Robert G. Weiss, Paul A. Bottomley, Christopher J. Hardy, and Gary Gerstenblith. Regional myocardial metabolism of high-energy phosphates during isometric exercise in patients with coronary artery disease. *New England Journal of Medicine*, 323(23):1593–1600, 1990. PMID: 2233948.

[63] Robert G. Weiss, Gary Gerstenblith, and Paul A. Bottomley. ATP flux through creatine kinase in the normal, stressed, and failing human heart. *Proceedings of the National Academy of Sciences of the United States of America*, 102(3):808–813, 2005.

[64] Ronglih Liao, Luigino Nascimben, Jan Friedrich, Judith K. Gwathmey, and Joanne S. Ingwall. Decreased energy reserve in an animal model of dilated cardiomyopathy: Relationship to contractile performance. *Circulation Research*, 78(5):893–902, 1996.

[65] Kurt W. Saupe, Matthias Spindler, Rong Tian, and Joanne S. Ingwall. Impaired cardiac energetics in mice lacking muscle-specific isoenzymes of creatine kinase. *Circulation Research*, 82(8):898–907, 1998.

[66] Robert S. Balaban, Howard L. Kantor, Lawrence A. Katz, and Richard W. Briggs. Relation between work and phosphate metabolite in the in vivo paced mammalian heart. *Science*, 232(4754):1121–1123, 1986.

[67] Greg Path, Pierre-Marie Robitaille, Hellmut Merkle, Martin Tristani, Jianyi Zhang, Michael Garwood, Arthur H. L. From, Robert J. Bache, and Kâmil Uğurbil. Correlation between transmural high energy phosphate levels and myocardial blood flow in the presence of graded coronary stenosis. *Circulation Research*, 67(3):660–73, 1990.

[68] Jianyi Zhang, Kâmil Uğurbil, Arthur H. L. From, and Robert J. Bache. Myocardial oxygenation and high-energy phosphate levels during graded coronary hypoperfusion. *American Journal of Physiology - Heart and Circulatory Physiology*, 280(1):H318–H326, 2001.

[69] Jianyi Zhang, Dirk J. Duncker, Ya Xu, Yi Zhang, Greg Path, Hellmut Merkle, Kristy Hendrich, Arthur. H. From, Robert J. Bache, and Kâmil Uğurbil. Transmural bioenergetic responses of normal myocardium to high workstates. *American Journal of Physiology - Heart and Circulatory Physiology*, 268(5):H1891–H1905, 1995.

[70] Jianyi Zhang, Arthur H. L. From, Kâmil Uğurbil, and Robert J. Bache. Myocardial oxygenation and high-energy phosphate levels during KATP channel blockade. *American Journal of Physiology - Heart and Circulatory Physiology*, 285(4):H1420–H1427, 2003.

[71] Jianyi Zhang, Greg Path, Vanaya Chepuri, David C. Homans, Hellmut Merkle, Kristy Hendrich, Kâmil Uğurbil, Robert J. Bache, and Arthur H. L. From. Effects of dobutamine on myocardial blood flow, contractile function,

and bioenergetic responses distal to coronary stenosis: Implications with regard to dobutamine stress testing. *American Heart Journal*, 129(2):330 – 342, 1995.

[72] Guangrong Gong, Kâmil Uğurbil, and Jianyi Zhang. Transmural metabolic heterogeneity at high cardiac work states. *American Journal of Physiology - Heart and Circulatory Physiology*, 277(1):H236–H242, 1999.

[73] Robert B. Jennings, Keith A. Reimer, Mary L. Hill, and Steven E. Mayer. Total ischemia in dog hearts, in vitro. 1. comparison of high energy phosphate production, utilization, and depletion, and of adenine nucleotide catabolism in total ischemia in vitro vs. severe ischemia in vivo. *Circulation Research*, 49(4):892–900, 1981.

[74] F. Mark Jeffrey, Charles J. Storey, Ray L. Nunnally, and Craig R. Malloy. Effect of ischemia on NMR detection of phosphorylated metabolites in the intact rat heart. *Biochemistry*, 28(13):5323–5326, 1989.

[75] Stuart M. Humphrey and Pamela B. Garlick. NMR-visible ATP and Pi in normoxic and reperfused rat hearts: a quantitative study. *American Journal of Physiology - Heart and Circulatory Physiology*, 260(1):H6–H12, 1991.

[76] Michael Garwood, Thomas Schleich, Brian D. Ross, Gerald B. Matson, and Wallace D. Winters. A modified rotating frame experiment based on a fourier series window function. application to in vivo spatially localized NMR spectroscopy. *Journal of Magnetic Resonance (1969)*, 65(2):239 – 251, 1985.

[77] Lei Ye, Husnain Kh. Haider, Shujia Jiang, Ru San Tan, Ruowen Ge, Peter K. Law, and Eugene K.W. Sim. Improved angiogenic response in pig heart following ischaemic injury using human skeletal myoblast simultaneously expressing vegf165 and angiopoietin-1. *European Journal of Heart Failure*, 9(1):15–22, 2007.

[78] Jianyi Zhang, Yo Murakami, Yi Zhang, Yong K Cho, Yun Ye, Guangrong Gong, Robert J. Bache, Kâmil Uğurbil, and Arthur H. L. From. Oxygen delivery does not limit cardiac performance during high work states. *American Journal of Physiology - Heart and Circulatory Physiology*, 277(1):H50–H57, 1999.

[79] Jianyi Zhang, Dirk J. Duncker, Xu Ya, Yi Zhang, Todd Pavek, Horan Wei, Hellmut Merkle, Kâmil Uğurbil, Arthur H. L. From, and Robert J. Bache. Effect of left ventricular hypertrophy secondary to chronic pressure overload on transmural myocardial 2-deoxyglucose uptake: A ^{31}P NMR spectroscopic study. *Circulation*, 92(5):1274–1283, 1995.

[80] David C. Homans, Richard Asinger, K. Joseph Elsperger, Darryl Erlien, Eugene Sublett, Frank Mikell, and Robert J. Bache. Regional function and perfusion at the lateral border of ischemic myocardium. *Circulation*, 71(5):1038–47, 1985.

[81] Dirk J. Duncker, Jianyi Zhang, and Robert J. Bache. Coronary pressure-flow relation in left ventricular hypertrophy. importance of changes in back pressure versus changes in minimum resistance. *Circulation Research*, 72(3):579–87, 1993.

[82] James G. Pipe. Spatial encoding and reconstruction in MRI with quadratic phase profiles. *Magnetic Resonance in Medicine*, 33(1):24–33, 1995.

[83] Jang-Yeon Park, Lance DelaBarre, and Michael Garwood. Improved gradient-echo 3D magnetic resonance imaging using pseudo-echoes created by frequency-swept pulses. *Magnetic Resonance in Medicine*, 55(4):848–857, 2006.

[84] Yoav Shrot and Lucio Frydman. Spatially encoded NMR and the acquisition of 2D magnetic resonance images within a single scan. *Journal of Magnetic Resonance*, 172(2):179 – 190, 2005.

[85] Ryan Chamberlain, Jang-Yeon Park, Curt Corum, Essa Yacoub, Kâmil Uğurbil, Clifford R. Jack, and Michael Garwood. RASER: A new ultra-fast magnetic resonance imaging method. *Magnetic Resonance in Medicine*, 58(4):794–799, 2007.

[86] Jean-Nicolas Dumez and Lucio Frydman. Multidimensional excitation pulses based on spatiotemporal encoding concepts. *Journal of Magnetic Resonance*, 226(0):22 – 34, 2013.

[87] Angela L. S. Snyder, Curtis A. Corum, Steen Moeller, Nathaniel J. Powell, and Michael Garwood. MRI by steering resonance through space. *Magnetic Resonance in Medicine*, 72(1):49–58, 2014.

[88] Jeff H. Duyn, Yihong Yang, Joseph A. Frank, and Jan Willem van der Veen. Simple correction method fork-space trajectory deviations in MRI. *Journal of Magnetic Resonance*, 132(1):150 – 153, 1998.

[89] J. Thomas Vaughan, Hoby P. Hetherington, Joe O. Otu, Jullie W. Pan, and Gerald M. Pohost. High frequency volume coils for clinical NMR imaging and spectroscopy. *Magnetic Resonance in Medicine*, 32(2):206–218, 1994.

[90] Vasily L. Yarnykh. Actual flip-angle imaging in the pulsed steady state: A method for rapid three-dimensional mapping of the transmitted radiofrequency field. *Magnetic Resonance in Medicine*, 57(1):192–200, 2007.

[91] John Pauly. RF pulse design.

[92] John I. Jackson, Craig H. Meyer, Dwight G. Nishimura, and Albert Macovski. Selection of a convolution function for fourier inversion using gridding. *Medical Imaging, IEEE Transactions on*, 10(3):473–478, Sep 1991.

[93] Axel Haase, Jens Frahm, Wolfgang Hanicke, and Dieter Matthaei. 1 H NMR chemical shift selective (CHESS) imaging. *Physics in Medicine and Biology*, 30(4):341, 1985.

[94] Steven Conolly, John Pauly, Dwight Nishimura, and Albert Macovsiu. Two-dimensional selective adiabatic pulses. *Magnetic Resonance in Medicine*, 24(2):302–313, 1992.

[95] David G. Norris, Peter J. Koopmans, Rasim Boyaciolu, and Markus Barth. Power independent of number of slices (PINS) radiofrequency pulses for low-power simultaneous multislice excitation. *Magnetic Resonance in Medicine*, 66(5):1234–1240, 2011.

[96] Geoffrey Bodenhausen, Ray Freeman, and David L. Turner. Suppression of artifacts in two-dimensional J spectroscopy. *Journal of Magnetic Resonance*, 27:511–514, 1977.

[97] Will Grissom. http://www.vuiis.vanderbilt.edu/ grissowa/.

[98] Djaudat Idiyatullin, Curt Corum, Steen Moeller, and Michael Garwood. Gapped pulses for frequency-swept MRI. *Journal of Magnetic Resonance*, 193(2):267 – 273, 2008.

[99] Noam Ben-Eliezer, Eddy Solomon, Elad Harel, Nava Nevo, and Lucio Frydman. Fully refocused multi-shot spatiotemporally encoded MRI: robust imaging in the presence of metallic implants. *Magnetic Resonance Materials in Physics, Biology and Medicine*, 25(6):433–442, 2012.